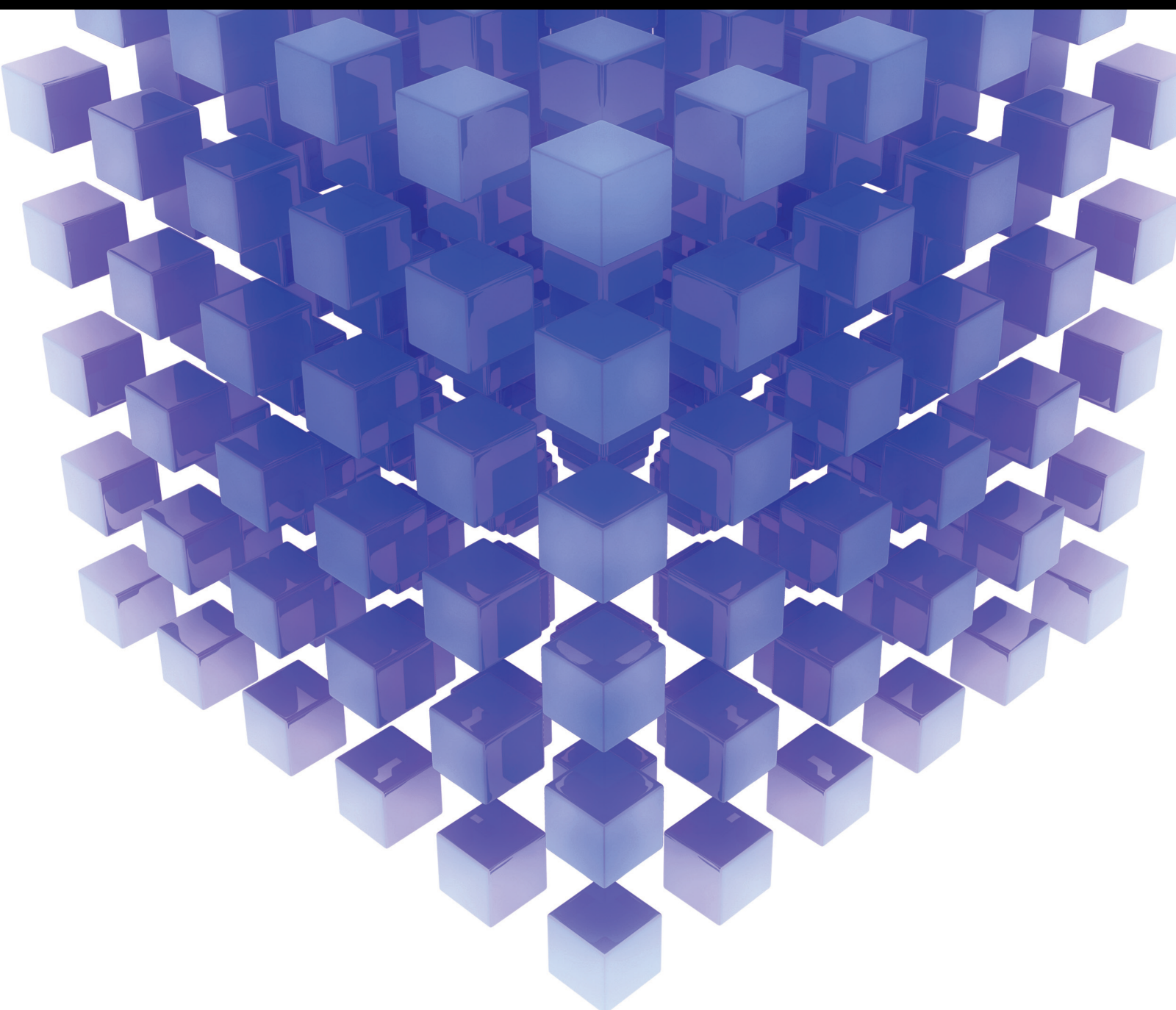


Mathematical Problems in Engineering

Advanced Control and Applications of Medical Robots

Lead Guest Editor: Zhan Li

Guest Editors: Hang Su, Bo Xiao, and Jing Guo





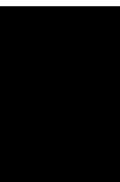
Advanced Control and Applications of Medical Robots

Mathematical Problems in Engineering

Advanced Control and Applications of Medical Robots

Lead Guest Editor: Zhan Li


Guest Editors: Hang Su, Bo Xiao, and Jing Guo



Copyright © 2021 Hindawi Limited. All rights reserved.

This is a special issue published in “Mathematical Problems in Engineering.” All articles are open access articles distributed under the Creative Commons Attribution License, which permits unrestricted use, distribution, and reproduction in any medium, provided the original work is properly cited.

Chief Editor

Guangming Xie , China

Academic Editors

Kumaravel A , India
Waqas Abbasi, Pakistan
Mohamed Abd El Aziz , Egypt
Mahmoud Abdel-Aty , Egypt
Mohammed S. Abdo, Yemen
Mohammad Yaghoub Abdollahzadeh
Jamalabadi , Republic of Korea
Rahib Abiyev , Turkey
Leonardo Acho , Spain
Daniela Addessi , Italy
Arooj Adeel , Pakistan
Waleed Adel , Egypt
Ramesh Agarwal , USA
Francesco Aggogeri , Italy
Ricardo Aguilar-Lopez , Mexico
Afaq Ahmad , Pakistan
Naveed Ahmed , Pakistan
Elias Aifantis , USA
Akif Akgul , Turkey
Tareq Al-shami , Yemen
Guido Ala, Italy
Andrea Alaimo , Italy
Reza Alam, USA
Osamah Albahri , Malaysia
Nicholas Alexander , United Kingdom
Salvatore Alfonzetti, Italy
Ghous Ali , Pakistan
Nouman Ali , Pakistan
Mohammad D. Aliyu , Canada
Juan A. Almendral , Spain
A.K. Alomari, Jordan
José Domingo Álvarez , Spain
Cláudio Alves , Portugal
Juan P. Amezcua-Sanchez, Mexico
Mukherjee Amitava, India
Lionel Amodeo, France
Sebastian Anita, Romania
Costanza Arico , Italy
Sabri Arik, Turkey
Fausto Arpino , Italy
Rashad Asharabi , Saudi Arabia
Farhad Aslani , Australia
Mohsen Asle Zaem , USA

Andrea Avanzini , Italy
Richard I. Avery , USA
Viktor Avrutin , Germany
Mohammed A. Awadallah , Malaysia
Francesco Aymerich , Italy
Sajad Azizi , Belgium
Michele Baccocchi , Italy
Seungik Baek , USA
Khaled Bahlali, France
M.V.A Raju Bahubalendruni, India
Pedro Balaguer , Spain
P. Balasubramaniam, India
Stefan Balint , Romania
Ines Tejado Balsera , Spain
Alfonso Banos , Spain
Jerzy Baranowski , Poland
Tudor Barbu , Romania
Andrzej Bartoszewicz , Poland
Sergio Baselga , Spain
S. Caglar Baslamisli , Turkey
David Bassir , France
Chiara Bedon , Italy
Azeddine Beghdadi, France
Andriette Bekker , South Africa
Francisco Beltran-Carbajal , Mexico
Abdellatif Ben Makhlof , Saudi Arabia
Denis Benasciutti , Italy
Ivano Benedetti , Italy
Rosa M. Benito , Spain
Elena Benvenuti , Italy
Giovanni Berselli, Italy
Michele Betti , Italy
Pietro Bia , Italy
Carlo Bianca , France
Simone Bianco , Italy
Vincenzo Bianco, Italy
Vittorio Bianco, Italy
David Bigaud , France
Sardar Muhammad Bilal , Pakistan
Antonio Bilotta , Italy
Sylvio R. Bistafa, Brazil
Chiara Boccaletti , Italy
Rodolfo Bontempo , Italy
Alberto Borboni , Italy
Marco Bortolini, Italy

Paolo Boscariol, Italy
Daniela Boso , Italy
Guillermo Botella-Juan, Spain
Abdesselem Boulkroune , Algeria
Boulaïd Boulkroune, Belgium
Fabio Bovenga , Italy
Francesco Braghin , Italy
Ricardo Branco, Portugal
Julien Bruchon , France
Matteo Bruggi , Italy
Michele Brun , Italy
Maria Elena Bruni, Italy
Maria Angela Butturi , Italy
Bartłomiej Błachowski , Poland
Dhanamjayulu C , India
Raquel Caballero-Águila , Spain
Filippo Cacace , Italy
Salvatore Caddemi , Italy
Zuowei Cai , China
Roberto Caldelli , Italy
Francesco Cannizzaro , Italy
Maosen Cao , China
Ana Carpio, Spain
Rodrigo Carvajal , Chile
Caterina Casavola, Italy
Sara Casciati, Italy
Federica Caselli , Italy
Carmen Castillo , Spain
Inmaculada T. Castro , Spain
Miguel Castro , Portugal
Giuseppe Catalanotti , United Kingdom
Alberto Cavallo , Italy
Gabriele Cazzulani , Italy
Fatih Vehbi Celebi, Turkey
Miguel Cerrolaza , Venezuela
Gregory Chagnon , France
Ching-Ter Chang , Taiwan
Kuei-Lun Chang , Taiwan
Qing Chang , USA
Xiaoheng Chang , China
Prasenjit Chatterjee , Lithuania
Kacem Chehdi, France
Peter N. Cheimets, USA
Chih-Chiang Chen , Taiwan
He Chen , China



































Kebing Chen , China
Mengxin Chen , China
Shyi-Ming Chen , Taiwan
Xizhong Chen , Ireland
Xue-Bo Chen , China
Zhiwen Chen , China
Qiang Cheng, USA
Zeyang Cheng, China
Luca Chiapponi , Italy
Francisco Chicano , Spain
Tirivanhu Chinyoka , South Africa
Adrian Chmielewski , Poland
Seongim Choi , USA
Gautam Choubey , India
Hung-Yuan Chung , Taiwan
Yusheng Ci, China
Simone Cinquemani , Italy
Roberto G. Citarella , Italy
Joaquim Ciurana , Spain
John D. Clayton , USA
Piero Colajanni , Italy
Giuseppina Colicchio, Italy
Vassilios Constantoudis , Greece
Enrico Conte, Italy
Alessandro Contento , USA
Mario Cools , Belgium
Gino Cortellessa, Italy
Carlo Cosentino , Italy
Paolo Crippa , Italy
Erik Cuevas , Mexico
Guozeng Cui , China
Mehmet Cunkas , Turkey
Giuseppe D'Aniello , Italy
Peter Dabnichki, Australia
Weizhong Dai , USA
Zhifeng Dai , China
Purushothaman Damodaran , USA
Sergey Dashkovskiy, Germany
Adiel T. De Almeida-Filho , Brazil
Fabio De Angelis , Italy
Samuele De Bartolo , Italy
Stefano De Miranda , Italy
Filippo De Monte , Italy

José António Fonseca De Oliveira
Correia , Portugal
Jose Renato De Sousa , Brazil
Michael Defoort, France
Alessandro Della Corte, Italy
Laurent Dewasme , Belgium
Sanku Dey , India
Gianpaolo Di Bona , Italy
Roberta Di Pace , Italy
Francesca Di Puccio , Italy
Ramón I. Diego , Spain
Yannis Dimakopoulos , Greece
Hasan Dinçer , Turkey
José M. Domínguez , Spain
Georgios Dounias, Greece
Bo Du , China
Emil Dumic, Croatia
Madalina Dumitriu , United Kingdom
Premraj Durairaj , India
Saeed Eftekhari Azam, USA
Said El Kafhali , Morocco
Antonio Elipse , Spain
R. Emre Erkmen, Canada
John Escobar , Colombia
Leandro F. F. Miguel , Brazil
FRANCESCO FOTI , Italy
Andrea L. Facci , Italy
Shahla Faisal , Pakistan
Giovanni Falsone , Italy
Hua Fan, China
Jianguang Fang, Australia
Nicholas Fantuzzi , Italy
Muhammad Shahid Farid , Pakistan
Hamed Faruqi, Iran
Yann Favennec, France
Fiorenzo A. Fazzolari , United Kingdom
Giuseppe Fedele , Italy
Roberto Fedele , Italy
Baowei Feng , China
Mohammad Ferdows , Bangladesh
Arturo J. Fernández , Spain
Jesus M. Fernandez Oro, Spain
Francesco Ferrise, Italy
Eric Feulvarch , France
Thierry Floquet, France


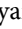




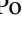





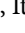
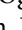



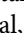

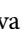
Eric Florentin , France
Gerardo Flores, Mexico
Antonio Forcina , Italy
Alessandro Formisano, Italy
Francesco Franco , Italy
Elisa Francomano , Italy
Juan Frausto-Solis, Mexico
Shujun Fu , China
Juan C. G. Prada , Spain
HECTOR GOMEZ , Chile
Matteo Gaeta , Italy
Mauro Gaggero , Italy
Zoran Gajic , USA
Jaime Gallardo-Alvarado , Mexico
Mosè Gallo , Italy
Akemi Gálvez , Spain
Maria L. Gandarias , Spain
Hao Gao , Hong Kong
Xingbao Gao , China
Yan Gao , China
Zhiwei Gao , United Kingdom
Giovanni Garcea , Italy
José García , Chile
Harish Garg , India
Alessandro Gasparetto , Italy
Stylianios Georgantzinou, Greece
Fotios Georgiades , India
Parviz Ghadimi , Iran
Ştefan Cristian Gherghina , Romania
Georgios I. Giannopoulos , Greece
Agathoklis Giaralis , United Kingdom
Anna M. Gil-Lafuente , Spain
Ivan Giorgio , Italy
Gaetano Giunta , Luxembourg
Jefferson L.M.A. Gomes , United Kingdom
Emilio Gómez-Déniz , Spain
Antonio M. Gonçalves de Lima , Brazil
Qunxi Gong , China
Chris Goodrich, USA
Rama S. R. Gorla, USA
Veena Goswami , India
Xunjie Gou , Spain
Jakub Grabski , Poland

Antoine Grall , France
George A. Gravvanis , Greece
Fabrizio Greco , Italy
David Greiner , Spain
Jason Gu , Canada
Federico Guarracino , Italy
Michele Guida , Italy
Muhammet Gul , Turkey
Dong-Sheng Guo , China
Hu Guo , China
Zhaoxia Guo, China
Yusuf Gurefe, Turkey
Salim HEDDAM , Algeria
ABID HUSSANAN, China
Quang Phuc Ha, Australia
Li Haitao , China
Petr Hájek , Czech Republic
Mohamed Hamdy , Egypt
Muhammad Hamid , United Kingdom
Renke Han , United Kingdom
Weimin Han , USA
Xingsi Han, China
Zhen-Lai Han , China
Thomas Hanne , Switzerland
Xinan Hao , China
Mohammad A. Hariri-Ardebili , USA
Khalid Hattaf , Morocco
Defeng He , China
Xiao-Qiao He, China
Yanchao He, China
Yu-Ling He , China
Ramdane Hedjar , Saudi Arabia
Jude Hemanth , India
Reza Hemmati, Iran
Nicolae Herisanu , Romania
Alfredo G. Hernández-Díaz , Spain
M.I. Herreros , Spain
Eckhard Hitzer , Japan
Paul Honeine , France
Jaromir Horacek , Czech Republic
Lei Hou , China
Yingkun Hou , China
Yu-Chen Hu , Taiwan
Yunfeng Hu, China
Can Huang , China
Gordon Huang , Canada
Linsheng Huo , China
Sajid Hussain, Canada
Asier Ibeas , Spain
Orest V. Iftime , The Netherlands
Przemyslaw Ignaciuk , Poland
Giacomo Innocenti , Italy
Emilio Insfran Pelozo , Spain
Azeem Irshad, Pakistan
Alessio Ishizaka, France
Benjamin Ivorra , Spain
Breno Jacob , Brazil
Reema Jain , India
Tushar Jain , India
Amin Jajarmi , Iran
Chiranjibe Jana , India
Łukasz Jankowski , Poland
Samuel N. Jator , USA
Juan Carlos Jáuregui-Correa , Mexico
Kandasamy Jayakrishna, India
Reza Jazar, Australia
Khalide Jbilou, France
Isabel S. Jesus , Portugal
Chao Ji , China
Qing-Chao Jiang , China
Peng-fei Jiao , China
Ricardo Fabricio Escobar Jiménez , Mexico
Emilio Jiménez Macías , Spain
Maolin Jin, Republic of Korea
Zhuo Jin, Australia
Ramash Kumar K , India
BHABEN KALITA , USA
MOHAMMAD REZA KHEDMATI , Iran
Viacheslav Kalashnikov , Mexico
Mathiyalagan Kalidass , India
Tamas Kalmar-Nagy , Hungary
Rajesh Kaluri , India
Jyotheeswara Reddy Kalvakurthi, India
Zhao Kang , China
Ramani Kannan , Malaysia
Tomasz Kapitaniak , Poland
Julius Kaplunov, United Kingdom
Konstantinos Karamanos, Belgium
Michal Kawulok, Poland

Irfan Kaymaz , Turkey
Vahid Kayvanfar , Qatar
Krzysztof Kecik , Poland
Mohamed Khader , Egypt
Chaudry M. Khalique , South Africa
Mukhtaj Khan , Pakistan
Shahid Khan , Pakistan
Nam-Il Kim, Republic of Korea
Philipp V. Kiryukhantsev-Korneev ,
Russia
P.V.V Kishore , India
Jan Koci , Czech Republic
Ioannis Kostavelis , Greece
Sotiris B. Kotsiantis , Greece
Frederic Kratz , France
Vamsi Krishna , India
Edyta Kucharska, Poland
Krzysztof S. Kulpa , Poland
Kamal Kumar, India
Prof. Ashwani Kumar , India
Michal Kunicki , Poland
Cedrick A. K. Kwuimy , USA
Kyandoghere Kyamakya, Austria
Ivan Kyrchei , Ukraine
Márcio J. Lacerda , Brazil
Eduardo Lalla , The Netherlands
Giovanni Lancioni , Italy
Jaroslaw Latalski , Poland
Hervé Laurent , France
Agostino Lauria , Italy
Aimé Lay-Ekuakille , Italy
Nicolas J. Leconte , France
Kun-Chou Lee , Taiwan
Dimitri Lefebvre , France
Eric Lefevre , France
Marek Lefik, Poland
Yaguo Lei , China
Kauko Leiviskä , Finland
Ervin Lenzi , Brazil
ChenFeng Li , China
Jian Li , USA
Jun Li , China
Yueyang Li , China
Zhao Li , China






























Zhen Li , China
En-Qiang Lin, USA
Jian Lin , China
Qibin Lin, China
Yao-Jin Lin, China
Zhiyun Lin , China
Bin Liu , China
Bo Liu , China
Heng Liu , China
Jianxu Liu , Thailand
Lei Liu , China
Sixin Liu , China
Wanquan Liu , China
Yu Liu , China
Yuanchang Liu , United Kingdom
Bonifacio Llamazares , Spain
Alessandro Lo Schiavo , Italy
Jean Jacques Loiseau , France
Francesco Lolli , Italy
Paolo Lonetti , Italy
António M. Lopes , Portugal
Sebastian López, Spain
Luis M. López-Ochoa , Spain
Vassilios C. Loukopoulos, Greece
Gabriele Maria Lozito , Italy
Zhiguo Luo , China
Gabriel Luque , Spain
Valentin Lychagin, Norway
YUE MEI, China
Junwei Ma , China
Xuanlong Ma , China
Antonio Madeo , Italy
Alessandro Magnani , Belgium
Toqeer Mahmood , Pakistan
Fazal M. Mahomed , South Africa
Arunava Majumder , India
Sarfranz Nawaz Malik, Pakistan
Paolo Manfredi , Italy
Adnan Maqsood , Pakistan
Muazzam Maqsood, Pakistan
Giuseppe Carlo Marano , Italy
Damijan Markovic, France
Filipe J. Marques , Portugal
Luca Martinelli , Italy
Denizar Cruz Martins, Brazil

Francisco J. Martos , Spain
Elio Masciari , Italy
Paolo Massioni , France
Alessandro Mauro , Italy
Jonathan Mayo-Maldonado , Mexico
Pier Luigi Mazzeo , Italy
Laura Mazzola, Italy
Driss Mehdi , France
Zahid Mehmood , Pakistan
Roderick Melnik , Canada
Xiangyu Meng , USA
Jose Merodio , Spain
Alessio Merola , Italy
Mahmoud Mesbah , Iran
Luciano Mescia , Italy
Laurent Mevel , France
Constantine Michailides , Cyprus
Mariusz Michta , Poland
Prankul Middha, Norway
Aki Mikkola , Finland
Giovanni Minafò , Italy
Edmondo Minisci , United Kingdom
Hiroyuki Mino , Japan
Dimitrios Mitsotakis , New Zealand
Ardashir Mohammadzadeh , Iran
Francisco J. Montáns , Spain
Francesco Montefusco , Italy
Gisele Mophou , France
Rafael Morales , Spain
Marco Morandini , Italy
Javier Moreno-Valenzuela , Mexico
Simone Morganti , Italy
Caroline Mota , Brazil
Aziz Moukrim , France
Shen Mouquan , China
Dimitris Mourtzis , Greece
Emiliano Mucchi , Italy
Taseer Muhammad, Saudi Arabia
Ghulam Muhiuddin, Saudi Arabia
Amitava Mukherjee , India
Josefa Mula , Spain
Jose J. Muñoz , Spain
Giuseppe Muscolino, Italy
Marco Mussetta , Italy

Hariharan Muthusamy, India
Alessandro Naddeo , Italy
Raj Nandkeolyar, India
Keivan Navaie , United Kingdom
Soumya Nayak, India
Adrian Neagu , USA
Erivelton Geraldo Nepomuceno , Brazil
AMA Neves, Portugal
Ha Quang Thinh Ngo , Vietnam
Nhon Nguyen-Thanh, Singapore
Papakostas Nikolaos , Ireland
Jelena Nikolic , Serbia
Tatsushi Nishi, Japan
Shanzhou Niu , China
Ben T. Nohara , Japan
Mohammed Nouari , France
Mustapha Nourelfath, Canada
Kazem Nouri , Iran
Ciro Núñez-Gutiérrez , Mexico
Włodzimierz Ogryczak, Poland
Roger Ohayon, France
Krzysztof Okarma , Poland
Mitsuhiro Okayasu, Japan
Murat Olgun , Turkey
Diego Oliva, Mexico
Alberto Olivares , Spain
Enrique Onieva , Spain
Calogero Orlando , Italy
Susana Ortega-Cisneros , Mexico
Sergio Ortobelli, Italy
Naohisa Otsuka , Japan
Sid Ahmed Ould Ahmed Mahmoud , Saudi Arabia
Taoreed Owolabi , Nigeria
EUGENIA PETROPOULOU , Greece
Arturo Pagano, Italy
Madhumangal Pal, India
Pasquale Palumbo , Italy
Dragan Pamučar, Serbia
Weifeng Pan , China
Chandan Pandey, India
Rui Pang, United Kingdom
Jürgen Pannek , Germany
Elena Panteley, France
Achille Paolone, Italy

George A. Papakostas , Greece
Xosé M. Pardo , Spain
You-Jin Park, Taiwan
Manuel Pastor, Spain
Pubudu N. Pathirana , Australia
Surajit Kumar Paul , India
Luis Payá , Spain
Igor Pažanin , Croatia
Libor Pekař , Czech Republic
Francesco Pellicano , Italy
Marcello Pellicciari , Italy
Jian Peng , China
Mingshu Peng, China
Xiang Peng , China
Xindong Peng, China
Yuexing Peng, China
Marzio Pennisi , Italy
Maria Patrizia Pera , Italy
Matjaz Perc , Slovenia
A. M. Bastos Pereira , Portugal
Wesley Peres, Brazil
F. Javier Pérez-Pinal , Mexico
Michele Perrella, Italy
Francesco Pesavento , Italy
Francesco Petrini , Italy
Hoang Vu Phan, Republic of Korea
Lukasz Pieczonka , Poland
Dario Piga , Switzerland
Marco Pizzarelli , Italy
Javier Plaza , Spain
Goutam Pohit , India
Dragan Poljak , Croatia
Jorge Pomares , Spain
Hiram Ponce , Mexico
Sébastien Poncet , Canada
Volodymyr Ponomaryov , Mexico
Jean-Christophe Ponsart , France
Mauro Pontani , Italy
Sivakumar Poruran, India
Francesc Pozo , Spain
Aditya Rio Prabowo , Indonesia
Anchasa Pramuanjaroenkij , Thailand
Leonardo Primavera , Italy
B Rajanarayan Prusty, India

Krzysztof Puszynski , Poland
Chuan Qin , China
Dongdong Qin, China
Jianlong Qiu , China
Giuseppe Quaranta , Italy
DR. RITU RAJ , India
Vitomir Racic , Italy
Carlo Rainieri , Italy
Kumbakonam Ramamani Rajagopal, USA
Ali Ramazani , USA
Angel Manuel Ramos , Spain
Higinio Ramos , Spain
Muhammad Afzal Rana , Pakistan
Muhammad Rashid, Saudi Arabia
Manoj Rastogi, India
Alessandro Rasulo , Italy
S.S. Ravindran , USA
Abdolrahman Razani , Iran
Alessandro Reali , Italy
Jose A. Reinoso , Spain
Oscar Reinoso , Spain
Haijun Ren , China
Carlo Renno , Italy
Fabrizio Renno , Italy
Shahram Rezapour , Iran
Ricardo Rianza , Spain
Francesco Riganti-Fulginei , Italy
Gerasimos Rigatos , Greece
Francesco Ripamonti , Italy
Jorge Rivera , Mexico
Eugenio Roanes-Lozano , Spain
Ana Maria A. C. Rocha , Portugal
Luigi Rodino , Italy
Francisco Rodríguez , Spain
Rosana Rodríguez López, Spain
Francisco Rossomando , Argentina
Jose de Jesus Rubio , Mexico
Weiguo Rui , China
Rubén Ruiz , Spain
Ivan D. Rukhlenko , Australia
Dr. Eswaramoorthi S. , India
Weichao SHI , United Kingdom
Chaman Lal Sabharwal , USA
Andrés Sáez , Spain

Bekir Sahin, Turkey
Laxminarayan Sahoo , India
John S. Sakellariou , Greece
Michael Sakellariou , Greece
Salvatore Salamone, USA
Jose Vicente Salcedo , Spain
Alejandro Salcido , Mexico
Alejandro Salcido, Mexico
Nunzio Salerno , Italy
Rohit Salgotra , India
Miguel A. Salido , Spain
Sinan Salih , Iraq
Alessandro Salvini , Italy
Abdus Samad , India
Sovan Samanta, India
Nikolaos Samaras , Greece
Ramon Sancibrian , Spain
Giuseppe Sanfilippo , Italy
Omar-Jacobo Santos, Mexico
J Santos-Reyes , Mexico
José A. Sanz-Herrera , Spain
Musavarah Sarwar, Pakistan
Shahzad Sarwar, Saudi Arabia
Marcelo A. Savi , Brazil
Andrey V. Savkin, Australia
Tadeusz Sawik , Poland
Roberta Sburlati, Italy
Gustavo Scaglia , Argentina
Thomas Schuster , Germany
Hamid M. Sedighi , Iran
Mijanur Rahaman Seikh, India
Tapan Senapati , China
Lotfi Senhadji , France
Junwon Seo, USA
Michele Serpilli, Italy
Silvestar Šesnić , Croatia
Gerardo Severino, Italy
Ruben Sevilla , United Kingdom
Stefano Sfarra , Italy
Dr. Ismail Shah , Pakistan
Leonid Shaikhet , Israel
Vimal Shanmuganathan , India
Prayas Sharma, India
Bo Shen , Germany
Hang Shen, China

Xin Pu Shen, China
Dimitri O. Shepelsky, Ukraine
Jian Shi , China
Amin Shokrollahi, Australia
Suzanne M. Shontz , USA
Babak Shotorban , USA
Zhan Shu , Canada
Angelo Sifaleras , Greece
Nuno Simões , Portugal
Mehakpreet Singh , Ireland
Piyush Pratap Singh , India
Rajiv Singh, India
Seralathan Sivamani , India
S. Sivasankaran , Malaysia
Christos H. Skiadas, Greece
Konstantina Skouri , Greece
Neale R. Smith , Mexico
Bogdan Smolka, Poland
Delfim Soares Jr. , Brazil
Alba Sofi , Italy
Francesco Soldovieri , Italy
Raffaele Solimene , Italy
Yang Song , Norway
Jussi Sopanen , Finland
Marco Spadini , Italy
Paolo Spagnolo , Italy
Ruben Specogna , Italy
Vasilios Spitas , Greece
Ivanka Stamova , USA
Rafał Stanisławski , Poland
Miladin Stefanović , Serbia
Salvatore Strano , Italy
Yakov Strelniker, Israel
Kangkang Sun , China
Qiuqin Sun , China
Shuaishuai Sun, Australia
Yanchao Sun , China
Zong-Yao Sun , China
Kumarasamy Suresh , India
Sergey A. Suslov , Australia
D.L. Suthar, Ethiopia
D.L. Suthar , Ethiopia
Andrzej Swierniak, Poland
Andras Szekrenyes , Hungary
Kumar K. Tamma, USA


Yong (Aaron) Tan, United Kingdom
Marco Antonio Taneco-Hernández , Mexico
Lu Tang , China
Tianyou Tao, China
Hafez Tari , USA
Alessandro Tasora , Italy
Sergio Teggi , Italy
Adriana del Carmen Téllez-Anguiano , Mexico
Ana C. Teodoro , Portugal
Efstathios E. Theotokoglou , Greece
Jing-Feng Tian, China
Alexander Timokha , Norway
Stefania Tomasiello , Italy
Gisella Tomasini , Italy
Isabella Torcicollo , Italy
Francesco Tornabene , Italy
Mariano Torrisi , Italy
Thang nguyen Trung, Vietnam
George Tsiatas , Greece
Le Anh Tuan , Vietnam
Nerio Tullini , Italy
Emilio Turco , Italy
Ilhan Tuzcu , USA
Efstratios Tzirtzilakis , Greece
FRANCISCO UREÑA , Spain
Filippo Ubertini , Italy
Mohammad Uddin , Australia
Mohammad Safi Ullah , Bangladesh
Serdar Ulubeyli , Turkey
Mati Ur Rahman , Pakistan
Panayiotis Vafeas , Greece
Giuseppe Vairo , Italy
Jesus Valdez-Resendiz , Mexico
Eusebio Valero, Spain
Stefano Valvano , Italy
Carlos-Renato Vázquez , Mexico
Martin Velasco Villa , Mexico
Franck J. Vernerey, USA
Georgios Veronis , USA
Vincenzo Vespri , Italy
Renato Vidoni , Italy
Venkatesh Vijayaraghavan, Australia

Anna Vila, Spain
Francisco R. Villatoro , Spain
Francesca Vipiana , Italy
Stanislav Vitek , Czech Republic
Jan Vorel , Czech Republic
Michael Vynnycky , Sweden
Mohammad W. Alomari, Jordan
Roman Wan-Wendner , Austria
Bingchang Wang, China
C. H. Wang , Taiwan
Dagang Wang, China
Guoqiang Wang , China
Huaiyu Wang, China
Hui Wang , China
J.G. Wang, China
Ji Wang , China
Kang-Jia Wang , China
Lei Wang , China
Qiang Wang, China
Qingling Wang , China
Weiwei Wang , China
Xinyu Wang , China
Yong Wang , China
Yung-Chung Wang , Taiwan
Zhenbo Wang , USA
Zhibo Wang, China
Waldemar T. Wójcik, Poland
Chi Wu , Australia
Qihong Wu, China
Yuqiang Wu, China
Zhibin Wu , China
Zhizheng Wu , China
Michalis Xenos , Greece
Hao Xiao , China
Xiao Ping Xie , China
Qingzheng Xu , China
Binghan Xue , China
Yi Xue , China
Joseph J. Yame , France
Chuanliang Yan , China
Xinggang Yan , United Kingdom
Hongtai Yang , China
Jixiang Yang , China
Mijia Yang, USA
Ray-Yeng Yang, Taiwan

Zaoli Yang , China
Jun Ye , China
Min Ye , China
Luis J. Yebra , Spain
Peng-Yeng Yin , Taiwan
Muhammad Haroon Yousaf , Pakistan
Yuan Yuan, United Kingdom
Qin Yuming, China
Elena Zaitseva , Slovakia
Arkadiusz Zak , Poland
Mohammad Zakwan , India
Ernesto Zambrano-Serrano , Mexico
Francesco Zammori , Italy
Jessica Zangari , Italy
Rafal Zdunek , Poland
Ibrahim Zeid, USA
Nianyin Zeng , China
Junyong Zhai , China
Hao Zhang , China
Haopeng Zhang , USA
Jian Zhang , China
Kai Zhang, China
Lingfan Zhang , China
Mingjie Zhang , Norway
Qian Zhang , China
Tianwei Zhang , China
Tongqian Zhang , China
Wenyu Zhang , China
Xianming Zhang , Australia
Xuping Zhang , Denmark
Yinyan Zhang, China
Yifan Zhao , United Kingdom
Debao Zhou, USA
Heng Zhou , China
Jian G. Zhou , United Kingdom
Junyong Zhou , China
Xueqian Zhou , United Kingdom
Zhe Zhou , China
Wu-Le Zhu, China
Gaetano Zizzo , Italy
Mingcheng Zuo, China


Contents

A High-Speed Elliptic Curve Cryptography Processor for Teleoperated Systems Security

Yong Xiao , Weibin Lin, Yun Zhao, Chao Cui, and Ziwen Cai




Research Article (8 pages), Article ID 6633925, Volume 2021 (2021)

Gait Recognition for Human-Exoskeleton System in Locomotion Based on Ensemble Empirical Mode Decomposition

Jing Qiu  and Huxian Liu

Research Article (13 pages), Article ID 5039285, Volume 2021 (2021)

Vaginal Secretions Epithelial Cells and Bacteria Recognition Based on Computer Vision

Shaozhi Guo , Haoyuan Guan , Jianzhong Li , Yonghua Liao , Weiwen Zhang , and Shengqiang Chen 






Research Article (9 pages), Article ID 8863147, Volume 2020 (2020)

Application of the Improved PSO-Based Extended Domain Method in Engineering

Bin Bai , Zhi-wei Guo, Qi-liang Wu , Junyi Zhang, and Yan-chao Cui 

Research Article (14 pages), Article ID 2846181, Volume 2020 (2020)

Restoration Methods of Respiratory Function for Spinal Cord Injury

X. Y. Gu , S. Ren , Y. Shi , N. Wang , Z. H. Tong , and M. L. Cai

Review Article (12 pages), Article ID 7398789, Volume 2020 (2020)

Research Article

A High-Speed Elliptic Curve Cryptography Processor for Teleoperated Systems Security

Yong Xiao , Weibin Lin, Yun Zhao, Chao Cui, and Ziwen Cai

Electric Power Research Institute of CSG, Guangzhou, Guangdong, 510663, China

Correspondence should be addressed to Yong Xiao; xiaoyong@csq.cn

Received 15 October 2020; Revised 8 November 2020; Accepted 26 November 2020; Published 23 January 2021

Academic Editor: Zhan Li

Copyright © 2021 Yong Xiao et al. This is an open access article distributed under the Creative Commons Attribution License, which permits unrestricted use, distribution, and reproduction in any medium, provided the original work is properly cited.

Teleoperated robotic systems are those in which human operators control remote robots through a communication network. The deployment and integration of teleoperated robot's systems in the medical operation have been hampered by many issues, such as safety concerns. Elliptic curve cryptography (ECC), an asymmetric cryptographic algorithm, is widely applied to practical applications because its far significantly reduced key length has the same level of security as RSA. The efficiency of ECC on $GF(p)$ is dictated by two critical factors, namely, modular multiplication (MM) and point multiplication (PM) scheduling. In this paper, the high-performance ECC architecture of SM2 is presented. MM is composed of multiplication and modular reduction (MR) in the prime field. A two-stage modular reduction (TSMR) algorithm in the SCA-256 prime field is introduced to achieve low latency, which avoids more iterative subtraction operations than traditional algorithms. To cut down the run time, a schedule is put forward when exploiting the parallelism of multiplication and MR inside PM. Synthesized with a 0.13 μm CMOS standard cell library, the proposed processor consumes 341.98k gate areas, and each PM takes 0.092 ms.

1. Introduction

In teleoperated robotic systems, human operators, often geographically distant, interact with and control robots through a communication network. Teleoperated robotic systems have many applications such as bomb disposal, search and rescue, robotic surgery, and medical operation. Teleoperated robotic surgery is a particularly important application of medical operation. Expert surgery is able to be performed remotely and without direct human presence. It is expected to have a significant impact on the quality of medical services in isolated regions, battlefields, or disaster areas. With the development of teleoperated systems and robots, the deployment and integration of teleoperated robots in the medical operation have encountered many problems such as safety concerns [1], time delay [2], and bilateral control [3]. Security is one of the biggest issues that hamper the deployment and integration of teleoperated robots and there are some works on it [4].

Telerobotic surgery is expected to be employed in extreme conditions, where teleoperated robots may have to

operate in harsh and low-power conditions, connecting to the Internet with potential loss. As depicted in Figure 1, the last communication link may even be a wireless link to a drone or a satellite, providing the connection to a trusted facility (possibly a large hospital with an established infrastructure) [5].

In such operating conditions, the security of the long-range control is significant, since if the teleoperated robotics are attacked by hackers, potential damage might be caused due to loss of proper control. Besides, verifying that these requirements are established and maintained during a teleoperated procedure is necessary [6].

In harsh conditions, low-power and time delay are significant. Hence, the security process, like digital signature/verification and encryption/decryption, should be implemented by hardware acceleration. Compared with software implementation, hardware implementation has many advantages, such as high efficiency, low power consumption, and safety. ECC is a kind of public key cryptography algorithm that can provide these security processes, proposed in 1986 by Miller [7] and Koblitz [8]. It

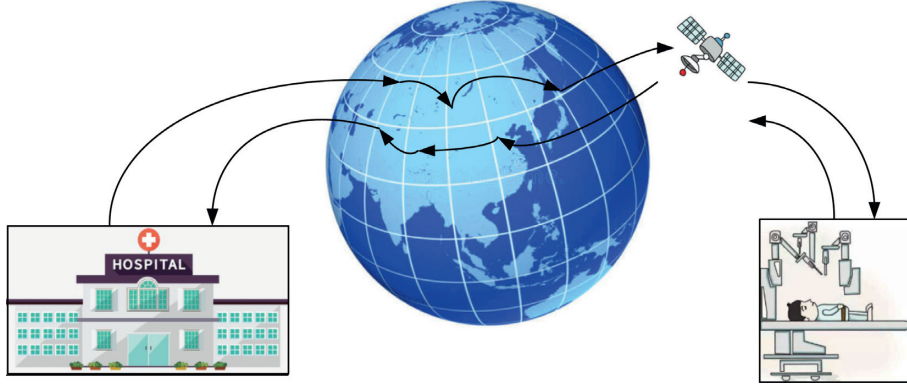


FIGURE 1: Visualization of a typical telerobotic surgery setup.

has been demonstrated to be used as an alternative to the classical RSA [9] thanks to its significantly reduced key lengths [10]. ECC when using 160–256 bits provides similar security compared with RSA or discrete logarithm schemes over finite fields (1024–4096 bits) [11]. SM2, as an ECC algorithm, was included in ISO/IEC14888-3/AMD1 in November 2017.

Considerable efforts have been made to implement the ECC with hardware as can be noticed in [12–22], during which MM operation is widely used for PM in ECC. In order to accelerate the MM, the proposed designs should be considered into three categories [23]: (1) the recommended prime modular multiplication algorithm, (2) Montgomery multiplication algorithm, and (3) the interleaved modular multiplication algorithm. Among those three categories, the first category is the fastest and it is limited by the specific prime field, such as NIST and SCA-256. The architecture in [12] equips Montgomery multiplier among 8-bit \times 8-bit to 64-bit \times 64-bit aiming to improve area efficiency and reduce delay at the cost of retarding speed. The designs in [9, 20] are based on the recommended prime modular multiplication algorithm. However, those MR algorithms only contain one stage, which will generate an intermediate result Z , such as $Z[0, 14p]$ in [9] and $Z[-4p, 5p]$ in [20]. Besides, an extra calculation is required to get the final result $Z[0, p]$. Notably, the architecture in [9] adopts a full-word 256-bit \times 256-bit multiplier, and all the calculations are executed in the SCA-256 prime field. In MR operation of design [9], 13 subtractions are taken to transfer the intermediate value Z ($0 \leq Z < 14p$) to the final value in the most needed situation, following with large latency.

Traditional software methods to implement cryptography algorithms will bring larger time delay and power consumption. However, hardware implementation can resolve these issues. Motivated to provide highly efficient safety assurance for teleoperated systems, we realize ECC by hardware implementation. The main contributions of this paper include the following:

We propose a high-performance hardware processor, which adopts a half-word multiplier to improve performance while reducing hardware consumption.

Compared with most of the other works, it has a better trade-off between performance and hardware overhead.

The TSMR algorithm in SCA-256 is proposed to implement low latency. The algorithm obtains the intermediate result $Z[0, 2p]$, which requires one subtraction to get the final result $Z[0, p]$. Compared with the traditional method [9] which obtains intermediate result $Z[0, 14p]$, our method avoids lots of subtractions to get the final result.

TSMR algorithm is implemented by a carry-save adder architecture to reduce latency and hardware overhead. Combined with Karatsuba-Ofman (KO) multiplication algorithm and pipeline design, MM requires an average of five clock cycles, even though one clock cycle for modular reduction and five clock cycles for multiplication are required.

The arrangement of this paper is as follows. In Section 2, the elliptic curve and PM are introduced. In Section 3, high-performance architecture is illustrated. Then, the proposed method is implemented and validated in Section 4. Finally, in Section 5, the conclusion of this work is provided.

2. Mathematical Background

2.1. Elliptic Curve. A nonsupersingular elliptic curve (EC) over $\text{GF}(p)$ is defined as a set of points (x, y) that conform to equation (1), also known as the Weierstrass equation, and an infinity point additionally:

$$y^2 = x^3 + ax + b, \quad (1)$$

where a and b are parameters, identifying the EC which satisfied $4a^3 + 27b^2 \neq 0 \pmod{p}$.

2.2. Point Multiplication. PM describes a transformation that k identical EC points add up to one, denoted as a scalar times an EC point “ kP ,” where $k = (k_{l-1} \cdots k_0)$, and l represents the binary length of k . In this work, the width NAF addition-subtraction method [24], given in Algorithm 1, is applied to point multiplication.

Input: width w , scalar k , EC point p
Output: EC point $Q = kP$
(1) Precomputation: $i \in \{1, 3, \dots, 2^{w-1} - 1\}, P[i] = iP$
(2) Compute $\text{NAF}_w(k) = \sum_{i=0}^{l-1} k_i 2^i$
(3) $Q = \infty$
(4) for i from $l-1$ downto 0 do
 $Q = 2Q$
 if $k_i \neq 0$ then
 if $k_i > 0$ then $Q = Q + P[k_i]$
 else $Q = Q - P[-k_i]$
(5) Return Q

ALGORITHM 1: Width NAF addition-subtraction method.

PM operation is the elemental operation of ECC and is performed as a sequence of elliptic curve addition (ECADD) and elliptic curve doubling (ECDBL). Let EC point $P_i = (X_i, Y_i, Z_i)$; the ECADD is defined as $P_3 = P_1 + P_2$ and ECDBL is defined as $P_3 = 2P_1$. To avoid time-consuming modular inversion/division operation, ECADD reaches the fastest efficiency in mixed affine-Jacobian coordinates, while there is ECDBL in Jacobian coordinates [25].

ECADD in mixed affine-Jacobian coordinates and ECDBL in Jacobian coordinates are given in the two following equations:

$$\begin{cases} X_3 = (Y_2 Z_1^3 - Y_1)^2 - (X_2 Z_1^2 - X_1)^2 (X_1 + X_2 Z_1^2), \\ Y_3 = (Y_2 Z_1^3 - Y_1)(X_1(X_2 Z_1^2 - X_1)^2 - X_3) - Y_1(X_2 Z_1^2 - X_1)^3, \\ Z_3 = (X_2 Z_1^2 - X_1) Z_1, \end{cases} \quad (2)$$

$$\begin{cases} X_3 = (3X_1^2 + aZ_1^4)^2 - 8X_1 Y_1^2, \\ Y_3 = (3X_1^2 + aZ_1^4)(4X_1 Y_1^2 - X_3) - 8Y_1^4, \\ Z_3 = 2Y_1 Z_1, \end{cases} \quad (3)$$

3. High-Performance Architecture of SM2

The PM architecture based on full-word multipliers is described below. TSMR and full-word multiplication constitute MM, while the binary modular inversion algorithm in [26] was applied to execute modular inversion (MI) operation.

3.1. Modular Reduction. SCA-256 has the characteristic that it can be denoted as $p = 2^{256} - 2^{224} - 2^{96} + 2^{64} - 1$. The traditional MR for SCA-256 [9] is given in Algorithm 2. After the fast reduction operation, the intermediate value can be represented as

$$Z = s_1 + s_2 + 2s_3 + 2s_4 + 2s_5 + s_6 + s_7 + s_8 + s_9 + 2s_{10} - s_{11} - s_{12} - s_{13} - s_{14}, \quad (4)$$

where $Z \in [0, 14p)$. It will cost at most 13 subtractions to get the final result $Z \in [0, p)$. Since the modular reduction would

be computed in a single clock cycle, the repetitive subtractions have a significant influence on the latency and bring about a lot of hardware resources consumption.

A TSMR algorithm on SCA-256 is proposed in this paper to address this problem (Algorithm 3). The first state takes sixteen addition/subtraction operations to calculate Z_1 , while the second one just costs two to calculate Z_2 . The intermediate value after two state fast reduction operations is $Z_2 = s_1 + s_{16} - s_{17}$, where $Z_2 \in [0, 2p)$, and it only needs one subtraction at most to obtain the final value $Z \in [0, p)$.

In ECADD or ECDBL operation, modular addition (MA) or modular subtraction (MS) operations are always required by the following MM operation. One cycle can be reduced when MA/MS was carried out. The max delay of carry-save addition only cares about the final carry. Therefore, adding one value to the other twenty values will not have a huge impact on latency. As shown in Algorithm 3, operand a in previous MA/MS is added to $(c + a) \bmod p$. In Algorithm 5 proposed below, such an operation appears twice in ECADD (Step 9: T2T2-T4, Step 11: T1T2-T4) and in ECDBL (Step 6: T2T2-T1, Step 8: T1T2-T5), respectively. The clock cycles, $m/(w+1) * 2 + m * 2 = 256/(4+1) * 2 + 26 * 2 = 614$, are reduced.

3.2. Carry-Save Adder Architecture. In TSFR algorithm, there are five subtraction operations in Z_1 and one in Z_2 . In order to reduce the area consumption and clock latency, a kind of new carry-save adder (CSA) architecture is presented for Algorithm 3, and the main advantage of CSA is that it can deal with subtraction operation. The subtraction operation becomes an addition operation by using the subtrahend's complement.

The first stage reduction result Z_1 , $0 \leq Z_1 < 16p$, was designed as 261-bit data, and it contains 21 operands and 20 256-bit CSAs. Due to one extended sign bit for five subtrahends' complement, as shown in Figure 2, it is noted that the 20 most significant bits (MSBs) of CSA cannot be cumulated. The CSA of 261 or more bits is not met. As shown in Figure 2, the MSB of Z_1 [261] could not be got from the sum of sc14 [260] to sc21 [260]. However, the 256-th to 260-th bits of subtrahend's complement are set to 1, while the 257-th to 261-th bits of addend are set to 0. The sum of the 256-th to 260-th bits of the subtrahend can be precalculated, getting $5 * 5'b11111 = 7'b1011011$. Only the low 5 bits ($5'b11011$) are needed, and it can be placed in row 1 of 1-bit CSA. In this case, the proposed CSA is completed with the function of settling the subtraction operations.

The first stage reduction operation architecture can be divided into two parts: the left part is a 1-bit CSA and the right part is a 32-bit CSA, as shown in Figure 3. To simplify the analysis, 1-bit CSA (1 full adder) is presented by a thin rectangle on the left, while a 32-bit CSA composed of 32 1-bit CSAs is presented by a wider rectangle on the right. For example, the subtraction operation in row 15 of the 32-bit CSA, $s_{12} = (0, 0, 0, 0, 0, c_9, 0, c_8)$, is represented by $-s_{12} = \sim s_{12} + 1 = (\overline{0}, \overline{0}, \overline{0}, \overline{0}, \overline{0}, \overline{c_9}, \overline{0}, \overline{c_8}) + 1$, where $\overline{0} = 32'hFFFFFFF$, $\overline{c_8} = \sim c_8$, and $1 = 32'h1$. The 32-bit CSA consists of 20 rows and 8 columns, which compute the result Z_1 [255: 0]. The 1-bit CSA is featured with 5 columns,

Input: Integer $c = (c_{15}, c_{14}, \dots, c_0)$ in base 2^{32} ; $c \in [0, p^2 - 1]$.
Output: $c \bmod p$

(1) $s1 = (c7, c6, c5, c4, c3, c2, c1, c0)$, $s2 = (c15, c14, c13, c12, c11, 0, c9, c8)$,
 $s3 = (c14, 0, c15, c14, c13, 0, c14, c13)$, $s4 = (c13, 0, 0, 0, 0, 0, c15, c14)$,
 $s5 = (c12, 0, 0, 0, 0, 0, 0, c15)$, $s6 = (c11, c11, c10, c15, c14, 0, c13, c12)$,
 $s7 = (c10, c15, c14, c13, c12, 0, c11, c10)$, $s8 = (c9, 0, 0, c9, c8, 0, c10, c9)$,
 $s9 = (c8, 0, 0, 0, c15, 0, c12, c11)$, $s10 = (c15, 0, 0, 0, 0, 0, 0, 0)$,
 $s11 = (0, 0, 0, 0, 0, c14, 0, 0)$, $s12 = (0, 0, 0, 0, 0, c13, 0, 0)$,
 $s13 = (0, 0, 0, 0, 0, c9, 0, 0)$, $s14 = (0, 0, 0, 0, 0, c8, 0, 0)$
 $Z = s1 + s2 + s3 + 2s4 + 2s5 + s6 + s7 + s8 + s9 + s10 -$
 $s11 - s12 - s13 - s14$

(2) Return $Z \bmod p$

ALGORITHM 2: Traditional modular reduction algorithm in SCA-256.

Input: integers a and $c = (c_{15}, c_{14}, \dots, c_0)$ in base 2^{32} ; $a \in [0, p - 1]$, $c \in [0, p^2 - 1]$.
Output: $(c+a) \bmod p$

(1) $s1 = (c7, c6, c5, c4, c3, c2, c1, c0)$; $s2 = (c15, 0, 0, 0, 0, 0, 0, c8)$;
 $s3 = (c14, 0, 0, c14, c14, 0, c14, c14)$; $s4 = (c13, 0, 0, 0, c13, 0, c13, c13)$;
 $s5 = (c12, 0, c15, 0, 0, 0, c15, c15)$; $s6 = (c11, c11, c13, c13, c11, 0, c11, c11)$;
 $s7 = (c10, c15, c10, 0, 0, 0, c10, c10)$; $s8 = (c9, c14, c14, c15, c15, 0, c9, c9)$;
 $s9 = (c8, 0, 0, c9, c8, 0, 0, 0)$; $s10 = (0, 0, 0, c12, c12, 0, c12, c12)$;
 $s11 = (0, 0, 0, 0, c14, c14, 0, 0)$; $s12 = (0, 0, 0, 0, 0, c9, 0, c8)$;
 $s13 = (0, 0, 0, 0, 0, c13, c13, 0)$; $s14 = (0, 0, 0, 0, 0, c8, 0, c8)$;
 $Z1 = s1 + 3s2 + 2s3 + 2s4 + 2s5 + s6 + s7 + s8 + s9 + s10 - s11 - s12 - s13 - s14 - a + p = (r8, r7, r6, r5, r4, r3, r2, r1, r0)$

(2) $s15 = (r7, r6, r5, r4, r3, r2, r1, r0)$; $s16 = (r8, 0, 0, 0, r8, 0, 0, r8)$; $s17 = (0, 0, 0, 0, 0, r8, 0, 0)$;
 $Z2 = s15 - s16 - s17$;
 $Z3 = Z2 - p$;
If $Z3 \geq 0$, return $Z3$
else return $Z2$

ALGORITHM 3: Two-stage modular reduction algorithm in SCA-256 (TSMR).

Input: A : 256-bit integer, satisfy $A = a_1 \times 2^{128} + a_0$
 B : 256 bit integer, satisfy $B = b_1 \times 2^{128} + b_0$.
Output: C : 512 bit product, satisfy $C = A \times B$.

(1) $P_{00} = a_0 \times b_0$; $a_{\text{sum}} = a_0 + a_1$;
(2) $P_{11} = a_1 \times b_1$; $b_{\text{sum}} = b_0 + b_1$;
(3) $P_{ss} = a_{\text{sum}} \times b_{\text{sum}}$, $C = (P_{11}, P_{00}) - P_{00} \times 2^{128}$;
(4) $C = C - P_{11} \times 2^{128}$;
(5) $C = C + P_{ss} \times 2^{128}$;
(6) return C

ALGORITHM 4: Karatsuba-Ofman multiplication algorithm.

and each of the columns has 10, 5, 2, 1, and 1 rows, respectively, which compute the result Z_1 [261: 256].

The second stage reduction operation is designed to compute the result of Z_2 , and it has 4 operands at most and needs 4 257-bit CSAs. Two 257-bit CSAs compute $Z_2 = s15 + s16 - s17$, one of which computes $(ss2_1, sc2_1) = s15 + s16 + \sim s17$, while the other computes $Z_2 = ss2_1 + sc2_1 + 1$. Besides, the remaining two 257-bit CSAs compute $Z_3 = ss2_1 + sc2_1 - p$, one of which

computes $(ss2_2, sc2_2) = ss2_1 + (sc2_2, 1'b1) + \sim p$, while the other computes $Z_3 = ss2_2 + sc2_2 + 1'b1$.

3.3. Integer Multiplication. Most of the traditional high-performance architectures are based on multipliers. Due to the disadvantages of full-word multipliers, long multiplication should be split into small bits and more operation cycles. Even though the one-cycle 256-bit multiplier in [20] possesses the best speed, it also consumes the most hardware area and the worst latency. To balance hardware consumption and performance, the KO multiplication algorithm based on divide-and-conquer is adopted in this paper, as shown in Algorithm 4:

$$\begin{aligned} A * B &= (a_1 2^{128} + a_0) * (b_1 2^{128} + b_0) \\ &= a_1 b_1 2^{256} + ((a_0 + a_1)(b_0 + b_1) - a_1 b_1 - a_0 b_0) 2^{128} + a_0 b_0, \end{aligned} \quad (5)$$

where $A, B \in GF(p)$, $a_0, a_1, b_0, b_1 \in [0, 2^{128} - 1]$. Compared with the cascading 128-bit \times 128-bit unsigned multipliers in [16] which use four amounts of half-word multiplication, the KO algorithm just uses three at the cost of one extra full-word

	ss14[260]	ss14[259]	ss14[258]	ss14[257]	ss14[256]	ss14[255]	...	ss14[0]
sc14[260]	sc14[259]	sc14[258]	sc14[257]	sc14[256]	sc14[255]	sc14[254]	...	1
	1	1	1	1	1	s12[255]	...	s12[0]
	ss15[260]	ss15[259]	ss15[258]	ss15[257]	ss15[256]	ss15[255]	...	ss15[0]
sc15[260]	sc15[259]	sc15[258]	sc15[257]	sc15[256]	sc15[255]	sc15[254]	...	1
	1	1	1	1	1	s13[255]	...	s13[0]
	ss16[260]	ss16[259]	ss16[258]	ss16[257]	ss16[256]	ss16[255]	...	ss16[0]
sc16[260]	sc16[259]	sc16[258]	sc16[257]	sc16[256]	sc16[255]	sc16[254]	...	1
	1	1	1	1	1	s14[255]	...	s14[0]
	ss17[260]	ss17[259]	ss17[258]	ss17[257]	ss17[256]	ss17[255]	...	ss17[0]
sc17[260]	sc17[259]	sc17[258]	sc17[257]	sc17[256]	sc17[255]	sc17[254]	...	1
	1	1	1	1	1	s15[255]	...	s15[0]
	ss18[260]	ss18[259]	ss18[258]	ss18[257]	ss18[256]	ss18[255]	...	ss18[0]
sc18[260]	sc18[259]	sc18[258]	sc18[257]	sc18[256]	sc18[255]	sc18[254]	...	1
	1	1	1	1	1	d[255]	...	d[0]
	ss19[260]	ss19[259]	ss19[258]	ss19[257]	ss19[256]	ss19[255]	...	ss19[0]
sc19[260]	sc19[259]	sc19[258]	sc19[257]	sc19[256]	sc19[255]	sc19[254]	...	0
	0	0	0	0	0	p[255]	...	p[0]
	ss20[260]	ss20[259]	ss20[258]	ss20[257]	ss20[256]	ss20[255]	...	ss20[0]
sc20[260]	sc20[259]	sc20[258]	sc20[257]	sc20[256]	sc20[255]	sc20[254]	...	0
sc21[260]	sc21[259]	sc21[258]	sc21[257]	sc21[256]	sc21[255]	sc21[254]	...	0
Z1[261]	Z1[260]	Z1[259]	Z1[258]	Z1[257]	Z1[256]	Z1[255]	...	Z1[0]

FIGURE 2: The carry-save addition in the first reduction.

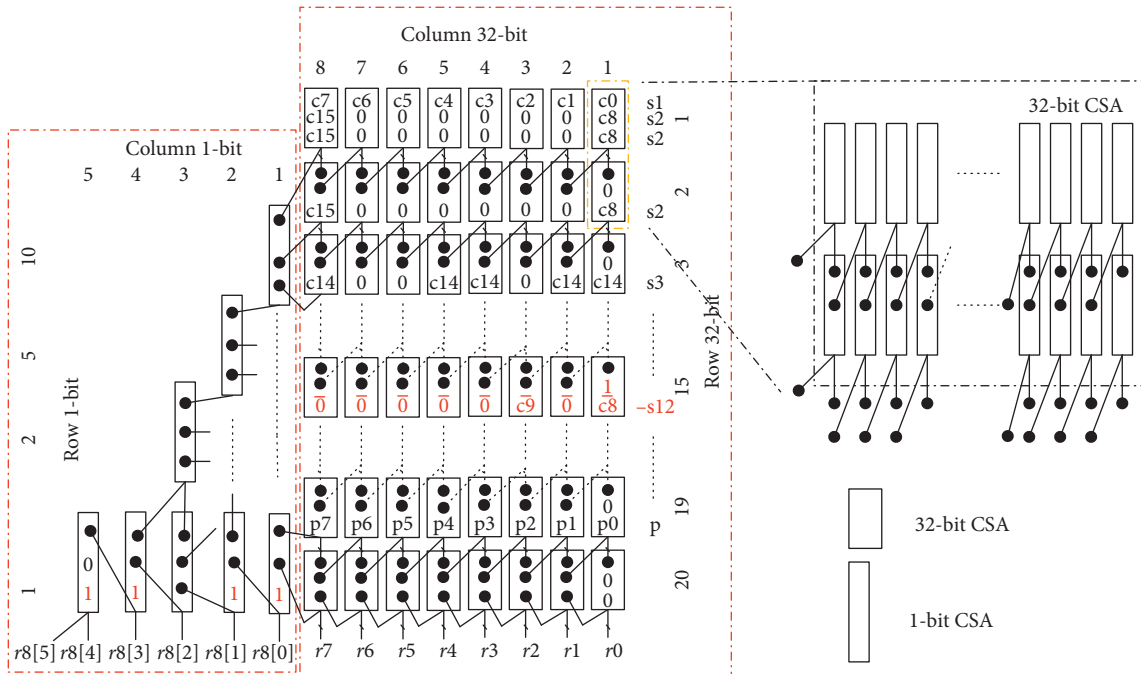
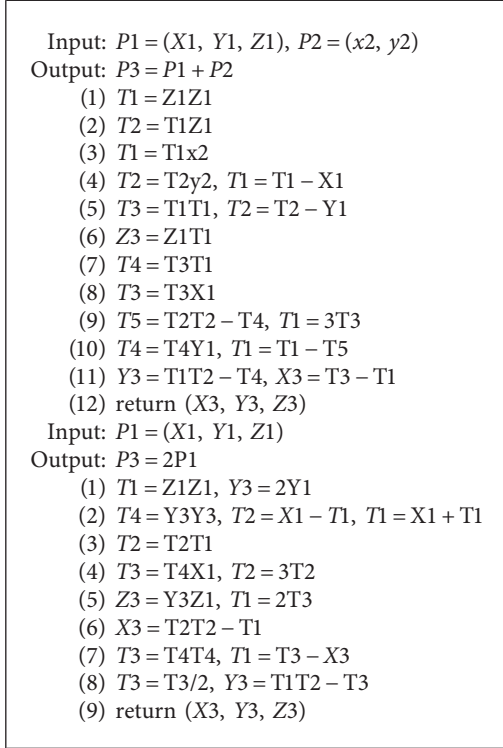


FIGURE 3: The first stage reduction with the carry-save addition.

subtraction and two extra half-word additions. While the KO algorithm presented in [11] requires six cycles, the KO algorithm presented in [27] requires only five cycles, shown in Algorithm 4.

3.4. Point Addition and Point Doubling. A series of ECADD and ECDBL operations make up PM. For no-idle cycles, a good

ECADD and ECDBL algorithm proposed in [27] is chosen for this architecture, given as Algorithm 5 below. The algorithm has three advantages. To be specific, firstly, the multiplication and MR are performing in parallel except for one case. It is noted that the second multiplication of the point addition must wait until the first modular multiplication finishes, because the one input of the second multiplication, multiplier T1, is the output of the first modular multiplication. Secondly,



ALGORITHM 5: Point addition and point doubling algorithm.

multiplication operation is constantly running, no matter whether shifting from ECDBL to ECDBL or switching between ECADD and ECDBL. Thirdly, hardware consumption is minimized by using only one modular multiplication unit and two modular addition/subtraction units. The proposed high-performance architecture is displayed in Figure 4. The MA/MS unit is designed to perform multiple functions, such as $T1 - X1$, $X1 + T1$, $3T1$, and $Y3/2$.

4. Implementation and Validation

The architecture described above is implemented with the Verilog-HDL language. It is synthesized using Design Compilers with the SMIC 130 nm CMOS standard cell library and is evaluated based on the 2-way NAND gate. Apart from that, for comparison with other designs on FPGA platform, it is also implemented on Xilinx Virtex-6 xc6vlx760, using Xilinx ISE 14.7. The performance is obtained by ModelSim simulation. The testing data meet the ECC cryptography protocol and are randomly generated. For a hardware design, the performance and hardware consumption are two main evaluation metrics. Besides, the time-area product is a metric to validate the trade-off between performance and hardware consumption.

With the window NAF recoding method, the time executing point multiplication is denoted as

$$\frac{m}{w+1}A + mD, \quad (6)$$

where $m = \log_2 p$; w refers to the width of NAF; A is the cycle that ECADD required, while D is ECDBL's cycle

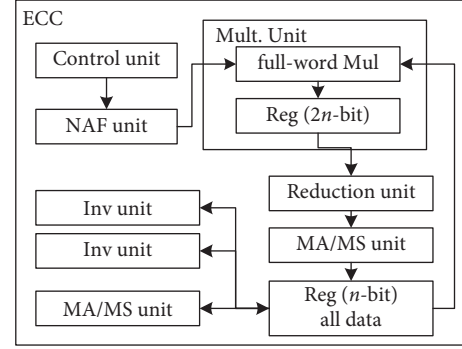


FIGURE 4: ECC architecture.

consumption. In this work, w is set to 4. The calculations of $1P$, $3P$, $5P$, and $7P$ are precalculated.

Table 1 shows the clocks that are required by each operation. In the fixed point, MM operation uses NAF4 recoding of scalar k and takes an average of 14242 cycles by testing 1000 times. After PM operation, two MI operations are required for coordinates conversion from Jacobian coordinates to affine coordinates.

Table 2 shows the comparison among other designs over 256-field-order GF (p). The architecture in [9] is using 256-bit multipliers. In this case, its area is large and there are 659 K gates. As it consumes many large hardware resources, it is not suitable for teleoperated robots. The architecture in [18] relies on two multiplier units using interleaved modular multiplication algorithms. Hence, it is featured with a smaller area but worse computation efficiency. The proposed design is 32.7 times faster in [18]. The architecture in [22] adopts a systolic arithmetic unit and obtains smaller areas but takes more clock cycles. The AT (area-time products) of our architecture are smaller than those of [18, 22].

The design in [28] adopts projective coordinates to avoid MI and employs a radix-2 modular multiplication algorithm for MM. In [29], Shah et al. presented a high-speed processor on the basis of redundant signed digit (RSD) arithmetic to prevent lengthy carry propagation delay. It is able to run at a high frequency of 327 MHz and requires 0.47 ms to perform a single PM operation. The architecture in [11] uses half-word multipliers based on the Barrett modular multiplication algorithm. In [19], a unified architecture of computing MA, MS, and MM is proposed. The designs in [30, 31] only apply adder results in a worse performance than ours. The radix-4 booth encoding interleaved modular multiplication algorithm is adopted in [30, 31]. Besides, the NAF point multiplication algorithm is applied in [31], while the double-and-always-add point multiplication algorithm is employed in [30]. As NAF2 has the merits of decreasing PM complexity from $(m/2 * A + mD)$ to $(m/3 * A + mD)$, the design in [30] takes more LUTs to get the comparable clock cycle consumption in the same platform compared with the design in [31]. The architecture proposed here needs fewer clock cycles and is faster when concerning performing point multiplication than those architectures in [11, 18, 19, 21, 30, 31].

The security concern is one of the most important issues in teleoperated robotics systems. In a harsh condition, time

TABLE 1: Cycle number of EC operations.

Operation	Cycle	Operation	Cycle
MA	1	ECADD	40
MS	1	ECDBL	56
MM	5	PM (fixed point)	14242
MI	544	PM (unfixed point)	18375

TABLE 2: Performance comparison.

Design	Platform	Field order	Area	Frequency (MHz)	Cycles (k)	PM (ms)	At
Ours	0.13um	SCA-256	341.98 <i>k</i> gate	153.8	14.24	0.092	31.66
[9]	0.13um	SCA-256	659 <i>k</i> gate	163.7	3.3	0.02	13.18
[18]	0.13um	256	167.5 <i>k</i> gate	110	331.1	3.01	504.18
[22]	0.13um	256	122 <i>k</i> gate	556	562	1.01	123.22
Ours	Virtex-6	SCA-256	10.06 <i>k</i> Slice, 80 DSP	38.388	14.24	0.37	3.72
[28]	Virtex-7	256	32.781 <i>k</i> LUTs	177.7	262.7	1.48	13.17
[29]	Virtex-6	256	65.6 <i>k</i> LUTs	327	153.16	0.47	30.83
[11]	Virtex-II	256	15.8 <i>k</i> Slice, 64 DSP	35.6	35	0.98	15.48
[19]	Virtex-4	256	13.16 <i>k</i> Slice	40	200	5.00	65.80
[30]	Virtex-4	256	35.7 <i>k</i> Slice	70	207.10	2.96	105.67
[31]	Virtex-4	256	20.579 <i>k</i> Slice	49	191.82	3.91	80.46

delay and power consumption are important, so using hardware to realize cryptographic algorithms has become an imperative tendency. The ECC processor we proposed here is implemented in hardware and can provide a high performance. The most complicated operations, such as PM, PA, and modular operations, are implemented by the hardware proposed here and this hardware module can be called by software to realize digital signature/verification and encryption/decryption to resolve the safety issue of teleoperated systems.

5. Conclusion

In a teleoperated system, robots interact with and are controlled by human operators through a communication network. Therefore, security becomes an import issue and ECC is the well choice among different cryptographic algorithms due to its lower key length. In this work, a high-performance ECC architecture of SM2 is proposed, which is suitable for the teleoperated robot's security. To reduce latency owing iterated subtractions, a TSMR algorithm on SCA-256 is presented. Thus, the intermediate result $Z \in [0, 2p)$ is improved when compared with $Z \in [0, 14p)$ of traditional algorithms. To avoid iterated subtractions, a TSMR algorithm in SCA-256 is shown and implemented with a carry-save adder architecture with the subtraction. To the area/performance trade-off, the half-word multiplier is adopted, equipped with pipeline design fully enhancing the calculation parallelism. The experimental results show that the proposed design takes 0.092 ms to perform 256-bit PM with 153.8 MHz frequency and consumes 341.98 *k* gate areas. Furthermore, the implementation result indicates that the proposed architecture has better performance and smaller AT than previous works.

In the future, the optimization of modular multiplication will be studied to further reduce the hardware overhead. The

portability of the hardware modules and the software-hardware codesign will be further studied to extend the application fields. Antiattack technology is another interesting piece of work worth studying.

Data Availability

The raw/processed data required to reproduce these findings cannot be shared at this time as the data also form part of an ongoing study.

Conflicts of Interest

The authors declare that there are no conflicts of interest regarding the publication of this paper.

Acknowledgments

This work was supported by the Independent High Safe Security Chip Research for the Metering and Electricity Program under Grant no. ZBKJXM20180014/SEPRI-K185011, and this support is acknowledged by the authors.

References

- [1] T. Bonaci and H. J. Chizeck, "Surgical telerobotics meets information security," in *Proceedings of the Robotics, Science and Systems (RSS) Workshop on Algorithmic Frontiers in Medical Robotics*, Freiburg, Germany, July 2012.
- [2] J. Guo, C. Liu, and P. Poignet, "A scaled bilateral teleoperation system for robotic-assisted surgery with time delay," *Journal of Intelligent & Robotic Systems*, vol. 95, no. 1, pp. 165–192, 2019.
- [3] H. Su, Y. Schmirander, Z. Li et al., "Bilateral teleoperation control of a redundant manipulator with an RCM kinematic constraint," in *Proceeding of the IEEE International Conference on Robotics and Automation (ICRA)*, Montreal, Canada, May 2020.

- [4] T. Bonaci, J. Yan, J. Herron et al., "Experimental analysis of denial-of-service attacks on teleoperated robotic systems," in *Proceedings of the 6th ACM/IEEE International Conference on Cyber-Physical Systems*, Seattle, WA, USA, April 2015.
- [5] T. Bonaci, J. Herron, T. Yusuf, T. Kohno, and H. J. Chizeck, "To make a robot secure: an experimental analysis of cyber security threats against teleoperated surgical robots," 2015, <http://arxiv.org/abs/1504.04339>.
- [6] T. Bonaci, A. Alva, J. Herron, R. Calo, and H. J. Chizeck, "I did it my way: on law and operator signatures for teleoperated robots," in *Proceedings of the Annual Conference on Robotics, Law and Policy*, Seattle, WA, USA, April 2015.
- [7] V. S. Miller, "Use of elliptic curves in cryptography," *Proceeding of CRYPTO*, vol. 1986, pp. 417–426, 1985.
- [8] N. Koblitz, "Elliptic curve cryptosystems," *Mathematics of Computation*, vol. 48, no. 177, p. 203, 1987.
- [9] Z. Zhao and G. Bai, "Ultra-high-speed SM2 ASIC implementation," in *Proceeding of the IEEE 13th International Conference*, pp. 182–188, Washington, DC, USA, October 2014.
- [10] State Cryptography Administration of China, *ISO/IEC 14888-3: SM2 Digital Signature Mechanism*, State Cryptography Administration of China, 2017.
- [11] X. Feng and S. Li, "A high performance FPGA implementation of 256-bit elliptic curve cryptography processor over GF (p)," *IEICE Transactions on Fundamentals of Electronics, Communications and Computer Sciences*, vol. E98.A, no. 3, pp. 863–869, 2015.
- [12] A. Satoh and K. Takano, "A scalable dual-field elliptic curve cryptographic processor," *IEEE Transactions on Computers*, vol. 52, no. 4, pp. 449–460, 2003.
- [13] H. Marzouqi and M. Al-Qutayri, "Review of elliptic curve cryptography processor designs," *Microprocessors and Microsystems*, vol. 39, no. 2, pp. 97–112, 2015.
- [14] I. H. Salah, F. Zhou, F. Gebali, and T. F. Al-Somani, "Review of elliptic curve processor architectures," in *Proceeding of the IEEE Pacific Rim Conference on Communications, Computers and Signal Processing (PACRIM)*, pp. 192–200, Victoria, BC, USA, August 2015.
- [15] H. Eberle, S. Shantz, V. Gupta, N. Gura, L. Rarick, and L. Spracklen, "Accelerating next-generation public-key cryptosystems on general-purpose CPUs," *IEEE Micro*, vol. 25, no. 2, pp. 52–59, 2005.
- [16] C. J. McIvor, M. McLoone, and J. V. McCanny, "Hardware elliptic curve cryptographic processor over," *IEEE Transactions on Circuits and Systems II*, vol. 53, no. 9, pp. 1946–1957, 2006.
- [17] A. K. Zia-Uddin and B. Mohammed, "Throughput/area-efficient ECC processor using Montgomery point multiplication on FPGA," *IEEE Transactions on Circuits and Systems II*, vol. 62, no. 11, pp. 1078–1082, 2015.
- [18] S. Ghosh and M. Alam, "DR Chowdhury, IS Gupta, "Parallel crypto-devices for GF (p) elliptic curve multiplication resistant against side channel attacks," *Computers & Electrical Engineering*, vol. 35, no. 2, pp. 329–338, 2009.
- [19] K. Javeed and X. Wang, "FPGA based high speed SPA resistant elliptic curve scalar multiplier architecture," *International Journal of Reconfigurable Computing*, vol. 5, pp. 1–10, 2016.
- [20] T. Güneysu and C. Paar, *Ultra High Performance ECC over NIST Primes on Commercial FPGAs*, Springer Berlin Heidelberg, Berlin, Germany, 2008.
- [21] S. Ghosh, M. Alam, I. S. Gupta, and D. R. Chowdhury, "A Robust GF (p) parallel arithmetic unit for public key cryptography," *EUROMICRO DSD*, pp. 109–115, 2007.
- [22] G. Chen, G. Bai, and H. Chen, "A High-Performance elliptic curve cryptographic processor for general curves over GF (p) based on a systolic arithmetic unit," *IEEE Transactions on Circuits and Systems II*, vol. 54, no. 5, pp. 412–416, 2007.
- [23] K. Javeed, X. Wang, and M. Scott, *Serial and Parallel Interleaved Modular Multipliers on FPGA Platform*, FPL, Juno Beach, FL, USA, 2015.
- [24] J. A. Solinas, "Efficient arithmetic on koblitz curves," *Designs Codes & Cryptography*, vol. 19, no. 2, pp. 195–249, 2000.
- [25] S. Ghosh, D. Mukhopadhyay, and D. Roychowdhury, "Petrel: power and timing attack resistant elliptic curve scalar multiplier based on programmable GF (p) arithmetic unit," *IEEE Transactions on Circuits & Systems I: Regular Papers*, vol. 58, no. 8, pp. 1798–1812, 2011.
- [26] D. Hankerson, A. Menezes, and S. Vanstone, *Guide to Elliptic Curve Cryptography*, Springer, Berlin, Germany, 2004.
- [27] X. Hu, X. Zheng, S. Zhang et al., "A high-performance elliptic curve cryptographic processor of SM2 over GF (p)," *Electronics*, vol. 8, no. 4, p. 431, 2019.
- [28] M. M. Islam, M. S. Hossain, M. K. Hasan et al., "FPGA implementation of high-speed area-efficient processor for elliptic curve point multiplication over prime field," *IEEE Access*, vol. 7, pp. 178811–178826, 2019.
- [29] Y. A. Shah, K. Javeed, S. Azmat et al., "Redundant-signed-digit-based high speed elliptic curve cryptographic processor," *Journal of Circuits, Systems, and Computers*, vol. 28, no. 5, pp. 120–126, 2019.
- [30] K. Javeed and X. Wang, "Low latency flexible FPGA implementation of point multiplication on elliptic curves over GF (p)," *International Journal of Circuit Theory & Applications*, vol. 45, no. 2, pp. 214–228, 2017.
- [31] K. Javeed, X. Wang, and M. Scott, "High performance hardware support for elliptic curve cryptography over general prime field," *Microprocess & Microsyst*, vol. 51, pp. 331–342, 2016.

Research Article

Gait Recognition for Human-Exoskeleton System in Locomotion Based on Ensemble Empirical Mode Decomposition

Jing Qiu ¹ and Huxian Liu²

¹School of Mechanical and Electrical Engineering, University of Electronic Science and Technology of China, Chengdu 611731, China

²School of Automation Engineering, Center for Robotics, University of Electronic Science and Technology of China, Chengdu 611731, China

Correspondence should be addressed to Jing Qiu; qiuqing@uestc.edu.cn

Received 23 June 2020; Revised 2 November 2020; Accepted 3 December 2020; Published 5 January 2021

Academic Editor: Jing Guo

Copyright © 2021 Jing Qiu and Huxian Liu. This is an open access article distributed under the Creative Commons Attribution License, which permits unrestricted use, distribution, and reproduction in any medium, provided the original work is properly cited.

As exoskeleton robots are more frequently applied to impaired people to regain mobility, detection and recognition of human gait motions is important to prepare suitable control modes for exoskeletons. This paper proposes to explore the potential of the ensemble empirical mode decomposition (EEMD) method to help analyze and recognize gait motions for human subjects who wear the exoskeleton to walk. The intrinsic mode functions (IMFs) extracted from the original gait signals by EEMD are utilized to act as inputs for classification algorithms. Evident correlations are found between some IMFs and original gait kinematic sequences. Experimental results on gait phase recognition performance on 14 able-bodied subjects are shown. The performance of the composing signals extracted from the original signals as IMF1 ~ IMF8 is investigated, which indicates that IMF8 might be helpful when wearing exoskeleton and IMF5 might be helpful when walking without exoskeleton on gait recognition. And the similarity of joint synergy between wearing and without wearing exoskeleton is analyzed, and the result shows that the joint synergy might change between with and without wearing exoskeleton. The quantitative results show that based on some IMFs of the same orders, these machine learning algorithms can achieve promising performances.

1. Introduction

Exoskeletons are encountered increasingly and frequently in assisting the movement of people in various aspects, helping them regain locomotion ability and reconstructing their lost gait. In order to achieve better gait transition for exoskeletons with different gait modulation modes switched, it is important to make accurate recognition of different gait phases for the human-exoskeleton system. In the past decades, researchers and engineers have developed a variety of methods for detecting and recognizing human gait with and without wearable robots. Aertbelien and Schutter developed a statistical model method to learn the joint gait trajectory and the variations for the control of the lower limb exoskeleton [1]. Brinker et al. proposed a gait recognition model that can fast adapt to a novel user's movements in

exoskeleton control by using previously collected other users' data and generate one side of leg exoskeleton movement based on the other side of the leg movement [2]. Kim et al. presented a novel shape-based and model-based combined gait recognition algorithm by extracting mode-based gait cycle based on the prediction-based hierarchical active shape mode [3]. Recently, Torricelli et al. presented a methodology to predict the human joint motion based on exoskeleton motion by combining personalized skeletal models of human subject with a kinematic model of the exoskeleton [4].

As some previous works mentioned, the human-exoskeleton system is a hybrid and complicated cognitive dynamics system. In particular, different subjects with exoskeletons may present different physical and dynamic parameters to be identified, which makes the whole

dynamic motion model hard to establish and personalize [5]. When the control system of exoskeleton wants to perform precise control tasks, it needs to know the accurate gait status of the human-exoskeleton system [6]. However, classification and recognition of gait phase through primal modeling and identification of the dynamic human-exoskeleton may be cumbersome. In this instance, utilization of some suitable machine learning algorithms driven by immediately acquired gait data might be feasible for the exoskeleton system to recognize different gait motions.

Since it is quite difficult to measure multiple joint torques and ground reaction forces simultaneously for the human-exoskeleton system, employing gait data acquired by motion capture devices is more convenient for the control system to process and configure [7]. Due to different influence factors such as subjects' biomechanics and physiological movement diversity, gait kinematic signals can be still characterized as nonlinear and nonstationary signals [8]. Thus, it would be suitable to use the empirical mode decomposition (EMD) method to analyze and extract the potential features concealed in gait data, as an alternative [9]. Some researchers have utilized such pathway to analyze gait signals [10]. For example, Cui et al. proposed a novel concept as step stability index (SSI) which evaluates subjects gait stability and fall risk by utilizing the decomposed the 1st ~ 4th intrinsic mode functions (IMFs) from its original signals [11]. Wen et al. found a new way based on improved EMD using Gaussian process to denoise gait accelerator data, and it gets better performance on denoising gait data [9]. Ren et al. discovered a good performance of neurodegenerative disease characterization by utilizing EMD to extract gait rhythm features from gait rhythm fluctuations which is based on signals of vertical ground reaction force [12]. Wang et al. achieved to characterize and differentiate the single waist accelerator signals through EMD between 5 gait patterns with high accuracy [13].

In this paper, we propose a framework of gait phase recognition for a human-exoskeleton system based on EMD. In such EMD-based recognition framework, eight IMF components are extracted from the original gait signals of 14 able-bodied subjects whose kinematics data are acquired by the optical-marked motion capture device. Six kinds of machine learning algorithms are applied for gait phase classification and recognition as follows: support vector machine (SVM), Kmeans, decision tree, logistic regression, Naive Bayes, and random forest methods. The extracted IMFs are used as the input for the training models with these six algorithms. The gait recognition results based on the 5th ~ 8th IMFs with some of these algorithms generally show promising performance. In the meanwhile, nonlinear fitting is used to examine the correlation between the decomposed IMFs and the original gait signals, and such fitting results could help to improve quantitatively evident observations on the correlations between IMFs and original gait data addressed in [11]. The difference and similarity of joint synergy between wearing with or without exoskeleton is analyzed. To our best knowledge, there is little work specifically focusing on human-exoskeleton gait phase recognition based on the EMD method in such manner.

2. Materials and Methods

In this section, experiments are divided into two parts. In the 1st part, kinematics data with and without exoskeletons during locomotion for the 14 subjects are measured by the optical motion capture system. In the 2nd part, another 3 subjects' joint angles are captured by the inertial measurement unit (IMU) system. For the 1st part and 2nd part of experiments, IMFs are extracted from the measured original kinematics data by ensemble empirical mode decomposition (EEMD) algorithm, and the method of evaluation of the correlation between them is proposed. For the 1st part experiments, joint synergy is extracted from joint angle data.

2.1. Experiment Setup. In the 1st part of experiments, 14 able-bodied subjects (all males, 22.88 ± 1.32 years old, 173.65 ± 5.22 cm height, and 54.59 ± 5.21 kg weight) took part in optical-object motion capture experiments to capture their kinematics data with and without exoskeletons during locomotion. In the 2nd part of experiments, another 2 able-bodied subjects and 1 paraplegia subject (all males, 25.66 ± 2.44 years old, 177.10 ± 19.33 cm height, and 62.13 ± 1.91 kg weight) also participated in the IMU-based motion acquisition experiments to measure their joint angles. All motion capture studies were performed with their consent. The experiments followed the institutional guidelines of the University of Electronic Science and Technology of China, and all the experiment operations were in accordance with the Declaration of Helsinki. They were all instructed to utilize the lower limb exoskeletons to perform the normal walking tasks during part of the optical-object motion capture experiments. The lower limb exoskeleton system used in the experiments was developed by the University of Electronic Science and Technology of China. Such lower limb exoskeleton system is with four active degrees of freedom (flexion/extension) of motion in hip and knee joints, and its ankle joints are with two passive degrees of freedom of motion (dorsi/plantar flexion). The subjects are required to use crutches to maintain the balance during their locomotion for safety reasons.

In the 1st part of experiments, during optical-object motion capture experiments, 39 infrared markers were attached to each subject's body for the VICON (Oxford Metrics Limited, UK) motion capture system according to the Plug-in Gait full body model [14]. The VICON system captured the locomotion of these 39 markers by 8 cameras with a frame rate of 100 Hz. The locomotion on elbow, shoulder, hip, knee, and ankle joints was acquired and converted to the angles of these joints through the algorithm provided by VICON. Each subject was required to perform 12 experiment sessions with different conditions, and a group of 30 joint angle signals (i.e., hip joint, knee joint, ankle joint, shoulder joint, and elbow joint at X, Y, and Z axes on both left side and right side, respectively) were captured correspondingly for each experiment session.

In the 2nd part of experiments, 7 IMU sensors (Perception Neuron, Noitom Limited) were bonded to the subjects lower body. The Perception Neuron system

captured the locomotion of these 7 sensors with a frame rate of 120 Hz. Raw data on the angles of hip, knee, and ankle joints were captured.

2.2. Experimental Protocol. In the 1st part of experiments, all the 14 subjects were required to perform walking tasks with wearing or without wearing exoskeleton on 6 different floors with different frictions and materials, which include normal floor, wood floor, ceramic floor, carpet, plastic lawn, and floor with cobble. The first session of the test for each subject was to let him walk on 6 different floor conditions wearing an exoskeleton, and the second session of the test was to let him walk on 6 different floor conditions without wearing an exoskeleton. These two sessions are independent and separate. Each subject was told to walk about 5 m for several times for both test sessions. For each experiment in different floor conditions with or without wearing exoskeleton, we clipped some of experiment sessions when some of markers are found to be lost on camera during the motion capture. Figure 1 shows the subjects walking on the floor with different materials.

2.3. EEMD Computation and IMF Extraction. In each experiment session, we need a group of 18 joint angle signals (hip joint, knee joint, and ankle joint at X, Y, and Z axes on both left side and right side, respectively) from 30 joint angle signals mentioned above to perform gait recognition. According to the EEMD design principle [10], the 18 original gait time signals $x(t)$ for each experiment session are to be decomposed into the following n intrinsic mode function (IMF) components, respectively:

$$x(t) = \sum_{j=1}^n c_j + r_n, \quad (1)$$

where c_j denotes the j th IMF component (i.e., termed as IMF $_j$) decomposed from the gait sequence $x(t)$ and r_n is the residue of $x(t)$. The EEMD algorithm for gait signals can be described by the following algorithm (Algorithm 1).

Figure 2(a) shows one of the 18 joint angle signals generated by one experiment session and its decomposed 8 IMF signals. Figure 2(b) shows the FFT of Figure 2(a); this shows that with the increase of IMF order number, the frequency of components the IMF contains decreases.

2.4. Gait Recognition. For the purpose of investigating how the various floor materials would affect the gait on subjects and how the different machine learning classifications and the traits of IMF would affect gait recognition when it comes to processing with VICON data in the part one experiments, we try to make gait recognition based on the 14 subjects' motion capture data, by applying classification/recognition approaches with the extracted IMF components. Before making recognition, first an algorithm is developed to tag gait phase status for every frame of dataset according to the signals of toe and heel marker on Z axis captured by VICON.

The tagged phase status contains four tags as left and right foot both on land, left foot on land and right foot off land, left foot off land and right foot on land, and the uncertain mode, where gait phase status information was used to generate dataset Y as label set. Then, we remove those frames labeled as uncertain mode in Y set and their corresponding frame in the VICON data. We make gait recognition on 3 perspectives: gait recognition modes A , B , and C .

2.4.1. Gait Recognition Mode A. In this mode, we randomly divided the dataset which we acquired from each experiment session into two parts as training set and testing set with 2 : 1 ratio for the whole gait dataset of each experiment session.

The original training dataset X and labeled dataset Y were composed of 8 IMFs as IMF1 ~ IMF8 dataset. And we let the IMF1 ~ IMF8 dataset signal train different machine learning models (SVM, Kmeans, decision tree, logistic regression, Naive Bayes, and random forest) and use the corresponding testing set to count the recognition accuracy.

2.4.2. Gait Recognition Mode B. In this mode, for each subject, we set the dataset on the *Normal Floor* as the training set and let the others of the same subject as the testing set. Because one subject's experiment with the floor with cobble was abandoned, we got 69 accuracies for the original dataset gait recognition. Then, the 8 IMFs as IMF1 ~ IMF8 dataset were generated by decomposing the original dataset, and we let the IMF1 ~ IMF8 dataset signal to evaluate different machine learning algorithms.

2.4.3. Gait Recognition Mode C. In this mode, for each floor material, we set the dataset of the same subject as the training set and let the others on the same floor material as the testing set. Because one subject's experiment with the floor with cobble was abandoned, we got 77 accuracies for the original dataset gait recognition. Then, we decompose the original data into 8 IMFs as IMF1 ~ IMF8 dataset, and we let the IMF1 ~ IMF8 dataset signal go through the same procedure as its original signal dataset X had been processed.

2.5. Evaluation of Correlation between IMF Components and Original Gait Trajectory. For the kinematics data of the subjects measured by VICON, 12 experiment sessions in the 1st part of experiments are performed on each subject to capture and thus produce a group of 18 original gait signals (i.e., hip, knee, and ankle angles for X, Y, and Z axes on both left side and right side, respectively) for each experiment session. For the joint data acquired by IMU in part two experiments, 3 experiment sessions are performed on all 3 subjects, and thus we generate a group of 3 original gait signals (i.e., left hip, left knee, and left ankle). For all those original signals S_n mentioned above, we divide them with dividing parameter $p \in [0, 1]$ into $S_{1,n}$ and $S_{2,n}$. It means that $S_{1,n}$ is the former p part of S_n and $S_{2,n}$ is the latter $(1 - p)$ part of S_n . And after the IMFs (IMF1 $_n$ ~ IMF8 $_n$, $n \in \{1, 2, \dots, 12 \times 18\}$) are extracted from these original gait



FIGURE 1: Experimental setup and walk test. The subjects walk on flat floors with 6 different friction situations with and without exoskeletons. Their gait information is acquired by motion capture devices and sensors.

Input: Original gait signal $x(t)$

Output: IMF1 ~ IMF8

- (1) For different N noisy signals $w_i(t)$, $i \in N$, we generate different $x_i(t)$ and calculate its corresponding decomposing results, IMF1 _{i} ~ IMF8 _{i} . This means we extract IMFs for N trials for different noisy signals $w_i(t)$.
- (2) **for** $i \in [1, N]$ **do**
 $x_i(t) = x(t) + w_i(t)$
 $r_{i,0} = x_i(t)$
- (3) Calculate (IMF j) _{i} for the original signal $x_i(t)$.
- (4) **for** $j \in [1, 8]$ **do**
 $k = 0$
 $h_{j,k}(t) = r_{i,j-1}$
- (5) Check SD to see whether $m(t)$ meets two conditions of IMF which is (1) in the whole dataset, the number of extrema and the number of zero crossings must either equal or differ at most by one; (2) at any point, the mean value of the envelope defined by the local maxima and the envelope defined by the local minima is zero.
- (6) **while** ((SD > threshold) or ($k == 0$)) **do**
 $m_k(t) = 1/2(u_k(t) + l_k(t))$
 $h_{j,k+1}(t) = h_{j,k}(t) - m_k(t)$
 $SD = \sum_{t=0}^T (h_{j,k+1}(t) - h_{j,k}(t))^2 / (h_{j,k}(t))^2$
 $k = k + 1$
- (7) where $u_k(t)$ is the upper envelope of $h_{j,k}(t)$ which is a cubic spline line connecting all the local maxima of $h_{j,k}(t)$ and $l_k(t)$ is the lower envelope of $h_{j,k}(t)$ which is a cubic spline line connecting all the local minima of $h_{j,k}(t)$
- (8) **end while**
- (9) (IMF j) _{i} = $h_{j,k}(t)$
- (10) $r_{i,j} = r_{i,j-1}(t) - (\text{IMF } j)_i$
- (11) $j = j + 1$
- (12) **end for**
- (13) Calculate the average value of (IMF j) _{i}
 $\text{IMF } j = 1/N \sum_{i=1}^N (\text{IMF } j)_i$ $j \in [1, 8]$
- (14) **end for**

signals S_n , $\text{IMF1}_{1,n} \sim \text{IMF8}_{1,n}$ and $\text{IMF1}_{2,n} \sim \text{IMF8}_{2,n}$ are also generated, respectively, for two data sequences $S_{1,n}$ and $S_{2,n}$. In order to investigate the correlation between the original gait signals and IMFs by cross validation in a nonlinear fitting manner, first, we construct the matrix U_n for each S_n as follows:

$$\begin{aligned}
 U_{j,n}^1 &= \begin{bmatrix} \text{IMF5}_{j,n} \\ \dots \\ \text{IMF8}_{j,n} \\ (\text{IMF5}_{j,n})^2 \\ \dots \\ (\text{IMF8}_{j,n})^2 \end{bmatrix} \\
 U_{j,n}^2 &= \begin{bmatrix} \text{IMF4}_{j,n} \\ \dots \\ \text{IMF8}_{j,n} \\ (\text{IMF4}_{j,n})^2 \\ \dots \\ (\text{IMF8}_{j,n})^2 \end{bmatrix}, \\
 U_{j,n}^3 &= \begin{bmatrix} \text{IMF4}_{j,n} \\ \dots \\ \text{IMF8}_{j,n} \\ (\text{IMF4}_{j,n})^2 \\ \dots \\ (\text{IMF8}_{j,n})^2 \\ (\text{IMF4}_{j,n})^3 \\ \dots \\ (\text{IMF8}_{j,n})^3 \end{bmatrix}, \\
 U_{j,n}^4 &= \begin{bmatrix} \text{IMF3}_{j,n} \\ \dots \\ \text{IMF8}_{j,n} \\ (\text{IMF3}_{j,n})^2 \\ \dots \\ (\text{IMF8}_{j,n})^2 \end{bmatrix}, \\
 & \quad j \in 1 \text{ or } 2.
 \end{aligned} \tag{2}$$

Next, we produce a number of new signal matrices $\widehat{S}_{2,n}^m$ ($m \in \{1, 2, \dots, 6\}$, $n \in \{1, 2, \dots, 108\}$) as follows:

$$\begin{aligned}
 \widehat{S}_{2,n}^1 &= U_{2,n}^1 (U_{1,n}^1)^{-1} S_{1,n}, \quad (p = 0.6), \\
 \widehat{S}_{2,n}^2 &= U_{2,n}^2 (U_{1,n}^2)^{-1} S_{1,n}, \quad (p = 0.4), \\
 \widehat{S}_{2,n}^3 &= U_{2,n}^2 (U_{1,n}^2)^{-1} S_{1,n}, \quad (p = 0.5), \\
 \widehat{S}_{2,n}^4 &= U_{2,n}^2 (U_{1,n}^2)^{-1} S_{1,n}, \quad (p = 0.6), \\
 \widehat{S}_{2,n}^5 &= U_{2,n}^3 (U_{1,n}^3)^{-1} S_{1,n}, \quad (p = 0.6), \\
 \widehat{S}_{2,n}^6 &= U_{2,n}^4 (U_{1,n}^4)^{-1} S_{1,n}, \quad (p = 0.6).
 \end{aligned} \tag{3}$$

Thus, we describe the variance between $\widehat{S}_{2,n}$ and $S_{2,n}$ by index VAF_n (variance accounted for) counted through the following equation:

$$\text{VAF}_n^m = 1 - \frac{\text{var}(\widehat{S}_{2,n}^m - S_{2,n})}{\text{var}(S_{2,n})}, \quad m \in [1, 6]. \tag{4}$$

As $\text{VAF}_n > 0$ is closer to 1, it indicates that they may possess more correlation evidence.

2.6. Joint Synergy Extraction. In addition, it is also important to further compare the joint synergy for subjects between them with wearing exoskeleton and without wearing exoskeleton to walk. We adopt principal component analysis (PCA) to extract the principal components of the five joints' angle data (i.e., ankle, knee, hip, shoulder, and elbow joints' angle) in the part one experiments. Some researchers have found that utilizing PCA to analyze the movement coordination patterns for human-exoskeleton might be useful [15, 16]. Firstly, we generate the following joint motion matrix D acquired for each individual.

$$D = \begin{bmatrix} D_{\text{ANK}} \\ D_{\text{KNEE}} \\ D_{\text{HIP}} \\ D_{\text{SLDR}} \\ D_{\text{ELBW}} \end{bmatrix} = \begin{bmatrix} D_{\text{ANK}}(1) & \dots & D_{\text{ANK}}(N) \\ D_{\text{KNEE}}(1) & \dots & D_{\text{KNEE}}(N) \\ D_{\text{HIP}}(1) & \dots & D_{\text{HIP}}(N) \\ D_{\text{SLDR}}(1) & \dots & D_{\text{SLDR}}(N) \\ D_{\text{ELBW}}(1) & \dots & D_{\text{ELBW}}(N) \end{bmatrix}, \tag{5}$$

where D_j ($j \in \{\text{ANK}, \text{KNEE}, \text{HIP}, \text{SLDR}, \text{ELBW}\}$) denotes the data about the degree of ankle, knee, hip, shoulder, and elbow joints which contain the information about joint synergy. The method of PCA creates a new set of variables called principal components. Each principal component is a linear projection of the original variables. We can generate PCA through the following equations:

$$\Sigma \alpha_l = \lambda_l \alpha_l, \tag{6}$$

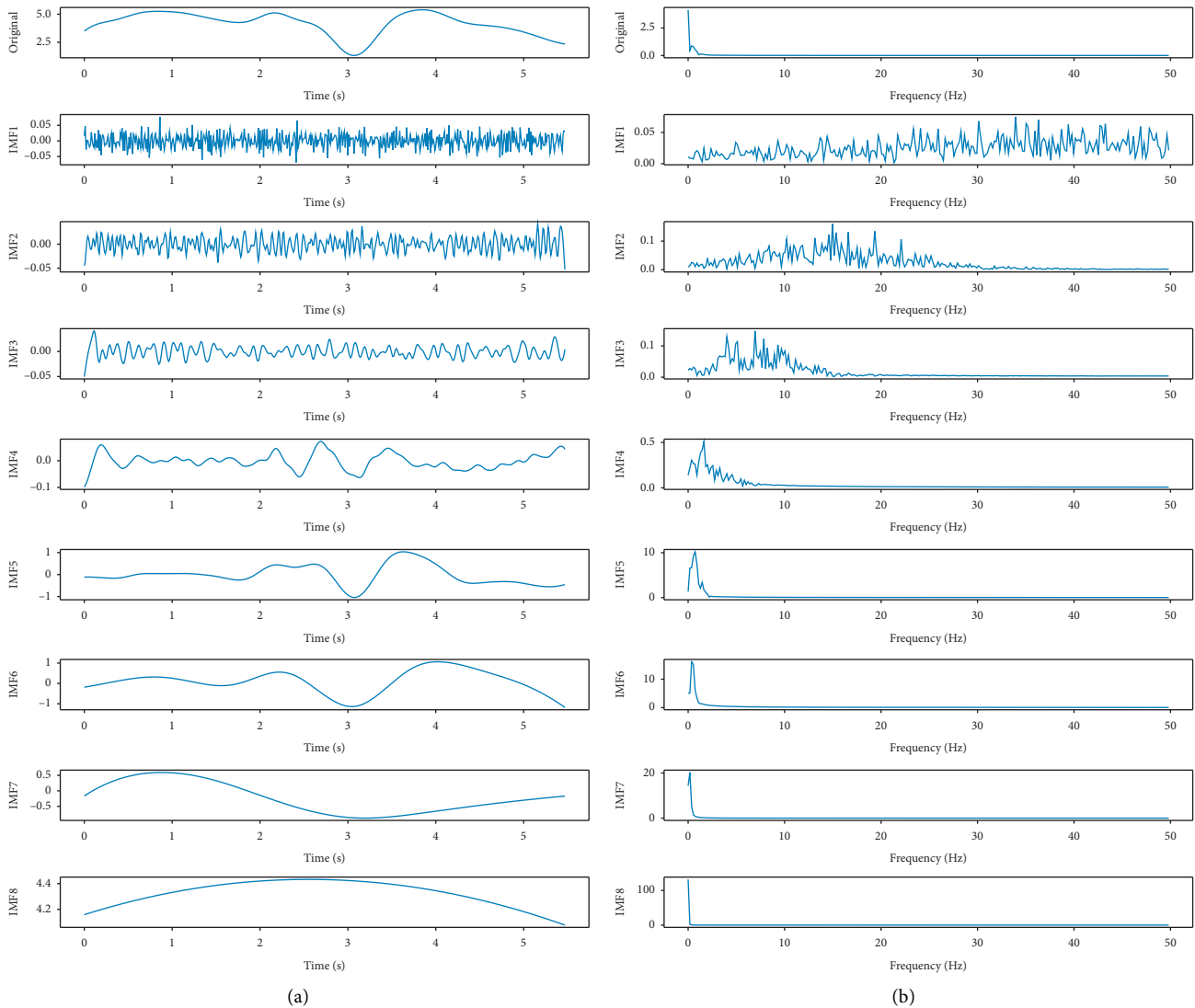


FIGURE 2: (a) One of the 18 joint angle signals generated by one experiment session and its decomposed 8 IMF signals and (b) FFT signals.

where Σ denotes the covariance of the matrix D we constructed, α_l denotes the direction that the original variables project on and also is the l th eigenvector for matrix Σ , and λ_l is the l th principal component corresponding to α_l .

3. Results and Discussion

In this section, the results of gait recognition modes A , B , and C for the human-exoskeleton system based on EEMD with the six machine learning methods are presented. The influence of floor materials on gait recognition has also been analyzed. Additionally, joint synergy for the subjects who walk with and without exoskeletons is also drawn.

3.1. Gait Recognition Mode A Results. Figure 3 shows the results of gait recognition mode A for the decomposing signals IMF1 ~ IMF8 of the original signals based on all the six machine learning methods (SVM, Kmeans, decision tree,

logistic regression, Naive Bayes, and random forest) for the 14 subjects who walked on flat floors with different friction situations with and without exoskeletons. Tables 1 and 2 show the detailed information of Figure 3. In this mode, we could figure out the performance for the six learning algorithms recognizing the gait status on each experiment session.

According to these two subfigures in Figure 3, recognition performance with IMF5 ~ IMF8 can be generally better than that with IMF1 ~ IMF4. From Tables 1 and 2, conclusion can be made that when IMF1 ~ IMF4 are used for the six algorithms, the recognition performance is not satisfactory since the accuracy generally cannot reach 80%. The performance of IMF5 ~ IMF8 is generally good for recognition. These comparative results might indicate that IMF5 ~ IMF8 may be considered to be involved in the recognition algorithms. Besides, in these results, especially when SVM, Kmeans, logistic regression, decision tree, and random forest approaches are applied for IMF5 ~ IMF8,

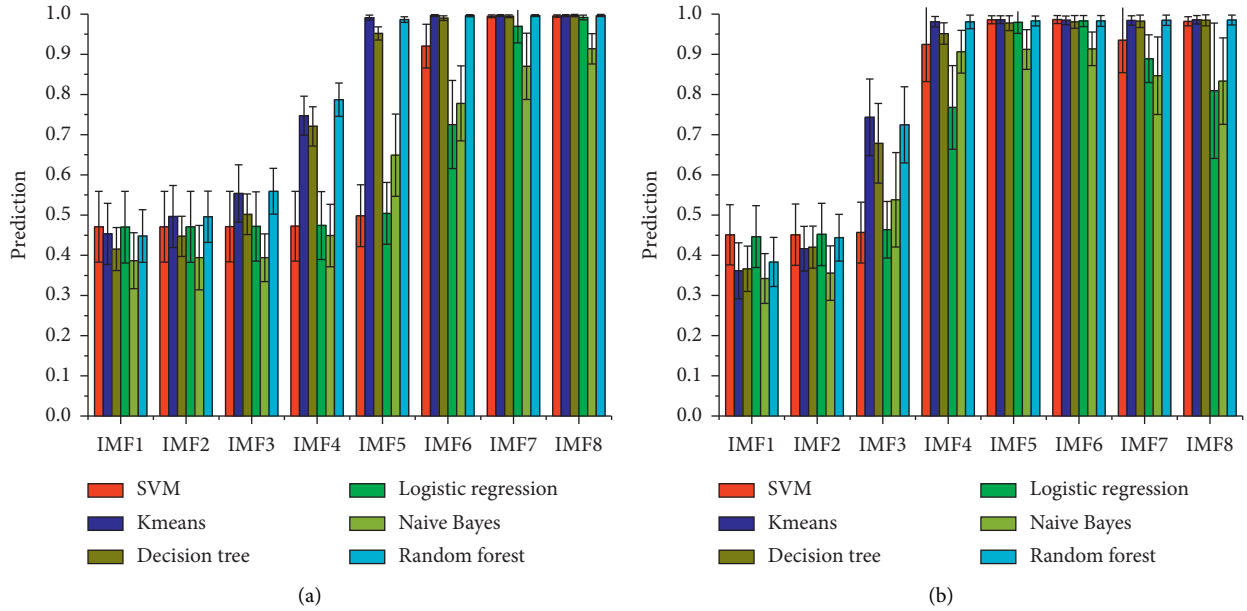


FIGURE 3: Gait recognition results for gait recognition mode A based on the IMFs of the original signal for the 14 subjects who walked on flat floors under different friction situations. (a) With exoskeleton. (b) Without exoskeleton.

TABLE 1: Gait recognition accuracy for gait recognition mode A based on the IMFs of the original signal for the 14 subjects who wore exoskeletons to walk (mean \pm SD%).

Component	SVM	Kmeans	Decision tree	Logistic regression	Naive Bayes	Random forest
IMF1	47.10 \pm 8.80	45.31 \pm 7.59	41.53 \pm 5.36	47.00 \pm 8.92	38.65 \pm 6.95	44.81 \pm 6.54
IMF2	47.09 \pm 8.82	49.64 \pm 7.71	44.71 \pm 5.02	47.07 \pm 8.81	39.42 \pm 8.02	49.60 \pm 6.37
IMF3	47.13 \pm 8.78	55.37 \pm 7.12	50.19 \pm 5.07	47.17 \pm 8.64	39.39 \pm 5.95	55.93 \pm 5.70
IMF4	47.23 \pm 8.67	74.74 \pm 4.85	72.09 \pm 4.87	47.40 \pm 8.43	44.91 \pm 7.78	78.70 \pm 4.15
IMF5	49.84 \pm 7.68	99.14 \pm 0.60	95.19 \pm 1.63	50.42 \pm 7.69	64.91 \pm 10.26	98.67 \pm 0.70
IMF6	92.06 \pm 5.44	99.65 \pm 0.21	99.00 \pm 0.58	72.54 \pm 10.96	77.79 \pm 9.33	99.63 \pm 0.26
IMF7	99.47 \pm 0.33	99.65 \pm 0.22	99.48 \pm 0.37	96.97 \pm 4.08	87.00 \pm 8.24	99.64 \pm 0.22
IMF8	99.54 \pm 0.29	99.66 \pm 0.22	99.65 \pm 0.29	99.20 \pm 0.59	91.38 \pm 3.77	99.66 \pm 0.27

promising recognition accuracy can be generated. Otherwise, in Tables 1 and 2, we can see that when we know the gait mode for someone in certain floor material, the gait recognition can reach 98% through IMF6, which means that IMF contains information for gait recognition.

Furthermore, Figure 4 shows the frequency that the maximum accuracies may occur in each order of IMF in all experiments, which stands for the probability that each IMF contributes to the recognition accuracy for the six algorithms. We generally can see that IMF7 and IMF8 have a higher probability to enhance the recognition accuracy for subjects who walk with exoskeletons, and IMF4 ~ IMF8 can have a higher probability for subjects who walk without exoskeletons. As we can see, the signal in IMF1 ~ IMF8 that can get the highest probability changes between wearing exoskeleton and without wearing exoskeleton. The reason behind this phenomenon may be that the gait locomotion mode changes between wearing exoskeleton and without wearing exoskeleton.

In conclusion, we can see that when it comes to recognizing gait with VICON data for each experiment session, all six algorithms are useful for recognition, and

IMF7 ~ IMF8 might be useful for recognition when wearing exoskeleton, while IMF4 ~ IMF8 might be helpful for recognition when walking without wearing exoskeleton.

3.2. Gait Recognition Mode B Results. Figure 5 shows the results of gait recognition mode B with the original signal's decomposing signals IMF1 ~ IMF8 for the same subject and various floor materials. Tables 3 and 4 show the detailed information of Figure 5. In this mode, we could evaluate the performance of the learning algorithm when we acquire one subject's gait data in one floor material to establish the recognition model and try to recognize the same subject's gait on other floor materials based on the model.

Kmeans could get good performance when wearing with or without exoskeleton as their highest recognition average accuracy all exceed 80% when with or without exoskeleton in both Figure 5(a) and 5(b).

When subjects wear exoskeleton, we can see that for different gait recognition algorithms, generally the higher the IMF order number is and the higher the accuracy is in Figure 5(a). Thus, the accuracy of IMF8 is the highest

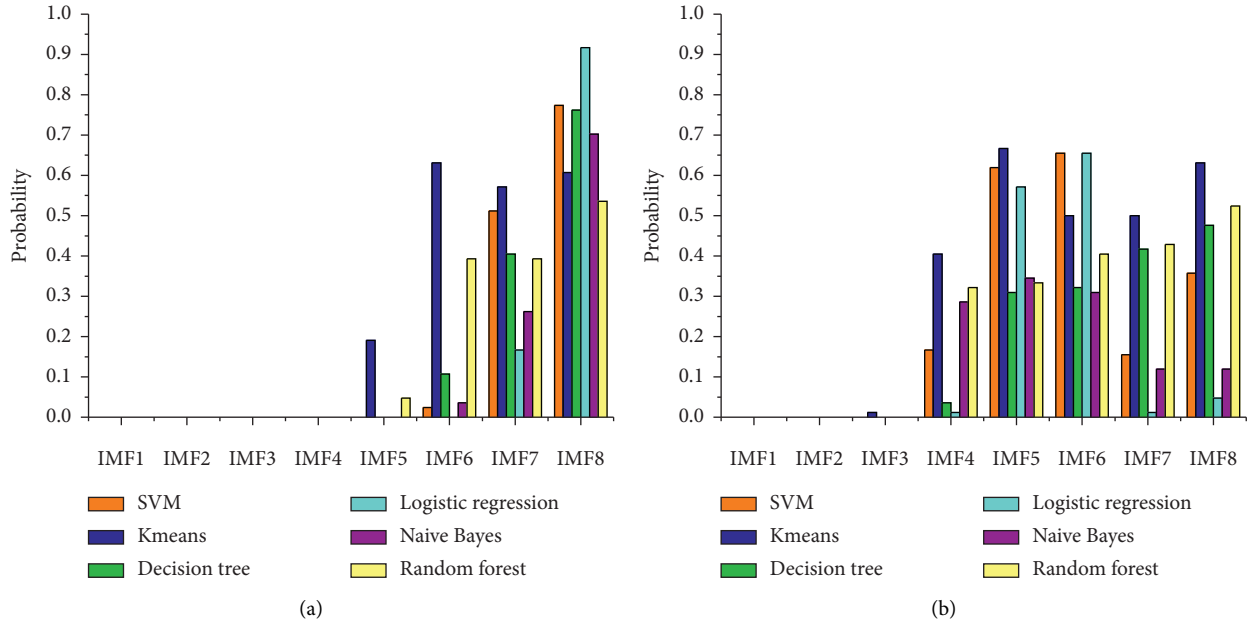


FIGURE 4: Maximum probability that each IMF contributes to the recognition accuracy on gait recognition mode A. (a) With exoskeleton. (b) Without exoskeleton.

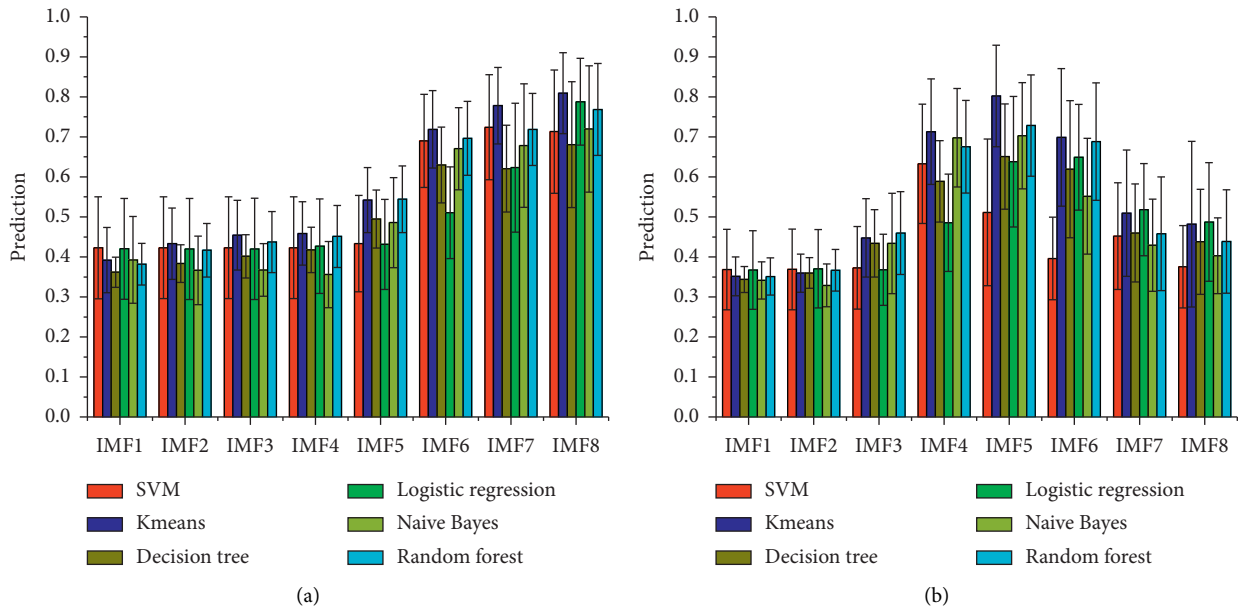


FIGURE 5: Gait recognition results of gait recognition mode B based on the IMFs of the original signal for the 14 subjects who walked on flat floors with different friction situations. (a) With exoskeleton. (b) Without exoskeleton.

(80.94%) with Kmeans according to Table 3. Kmeans, logistic regression, and random forest have a good performance with IMF8 in Table 3. Figure 5(b) shows that when subjects walk without exoskeleton, generally IMF4 ~ IMF6 have relatively better performance among IMF1 ~ IMF8, and IMF5 is the highest (80.24%) with Kmeans.

Additionally, Figure 6 shows the probability for IMF1 ~ IMF8 that each IMF may be the highest accuracy among IMF1 ~ IMF8 for the six algorithms. From Figure 6,

we could generally conclude that IMF8 has the highest probability to get the maximum accuracy among IMF1 ~ IMF8 when wearing exoskeleton and IMF5 is most likely to get the maximum accuracy among IMF1 ~ IMF8 when walking without exoskeleton. Signal in IMF1 IMF8 that can get the highest probability changes between wearing exoskeleton and without wearing exoskeleton. As with mode A, signal in IMF1 ~ IMF8 that can get the highest probability in mode B changes between wearing an exoskeleton

TABLE 2: Gait recognition accuracy for gait recognition mode A based on the IMFs of the original signal for the 14 subjects who walked without exoskeletons (mean \pm SD%).

Component	SVM	Kmeans	Decision tree	Logistic regression	Naive Bayes	Random forest
IMF1	45.10 \pm 7.49	36.13 \pm 6.97	36.62 \pm 5.63	44.63 \pm 7.69	34.23 \pm 6.20	38.33 \pm 6.09
IMF2	45.11 \pm 7.61	41.64 \pm 5.53	42.00 \pm 5.24	45.20 \pm 7.74	35.55 \pm 6.79	44.36 \pm 5.81
IMF3	45.65 \pm 7.58	74.32 \pm 9.56	67.86 \pm 9.90	46.35 \pm 7.03	53.79 \pm 11.74	72.47 \pm 9.47
IMF4	92.45 \pm 9.22	98.13 \pm 1.26	95.17 \pm 2.65	76.79 \pm 10.41	90.65 \pm 5.34	98.08 \pm 1.69
IMF5	98.59 \pm 0.98	98.62 \pm 0.95	97.75 \pm 1.85	97.96 \pm 2.75	91.20 \pm 4.96	98.30 \pm 1.24
IMF6	98.64 \pm 1.00	98.45 \pm 1.08	98.05 \pm 1.58	98.29 \pm 1.39	91.36 \pm 4.17	98.32 \pm 1.36
IMF7	93.52 \pm 8.11	98.42 \pm 1.17	98.22 \pm 1.56	88.90 \pm 5.94	84.67 \pm 9.65	98.47 \pm 1.29
IMF8	98.20 \pm 1.14	98.59 \pm 1.05	98.45 \pm 1.35	80.94 \pm 16.84	83.31 \pm 10.76	98.56 \pm 1.24

TABLE 3: Gait recognition accuracy for gait recognition mode B based on the IMFs of the original signal for the 14 subjects who wore exoskeletons to walk (mean \pm SD%).

Component	SVM	Kmeans	Decision tree	Logistic regression	Naive Bayes	Random forest
IMF1	42.28 \pm 12.73	39.19 \pm 8.16	36.19 \pm 3.77	42.03 \pm 12.61	39.25 \pm 10.85	38.17 \pm 5.20
IMF2	42.29 \pm 12.73	43.31 \pm 8.90	38.34 \pm 4.69	41.99 \pm 12.61	36.66 \pm 8.57	41.67 \pm 6.70
IMF3	42.29 \pm 12.73	45.44 \pm 8.72	40.16 \pm 5.41	42.00 \pm 12.67	36.75 \pm 6.58	43.73 \pm 7.62
IMF4	42.29 \pm 12.73	45.86 \pm 7.94	41.74 \pm 5.67	42.68 \pm 11.82	35.60 \pm 8.27	45.12 \pm 7.73
IMF5	43.33 \pm 12.05	54.22 \pm 8.15	49.49 \pm 7.25	43.14 \pm 11.27	48.57 \pm 11.27	54.42 \pm 8.32
IMF6	69.01 \pm 11.65	71.89 \pm 9.70	63.00 \pm 9.47	51.07 \pm 11.46	67.05 \pm 10.27	69.62 \pm 9.24
IMF7	72.41 \pm 13.12	77.81 \pm 9.57	62.07 \pm 10.83	62.32 \pm 16.11	67.84 \pm 15.42	71.87 \pm 8.98
IMF8	71.34 \pm 15.41	80.94 \pm 10.13	68.07 \pm 15.73	78.78 \pm 10.84	72.00 \pm 15.80	76.87 \pm 11.48

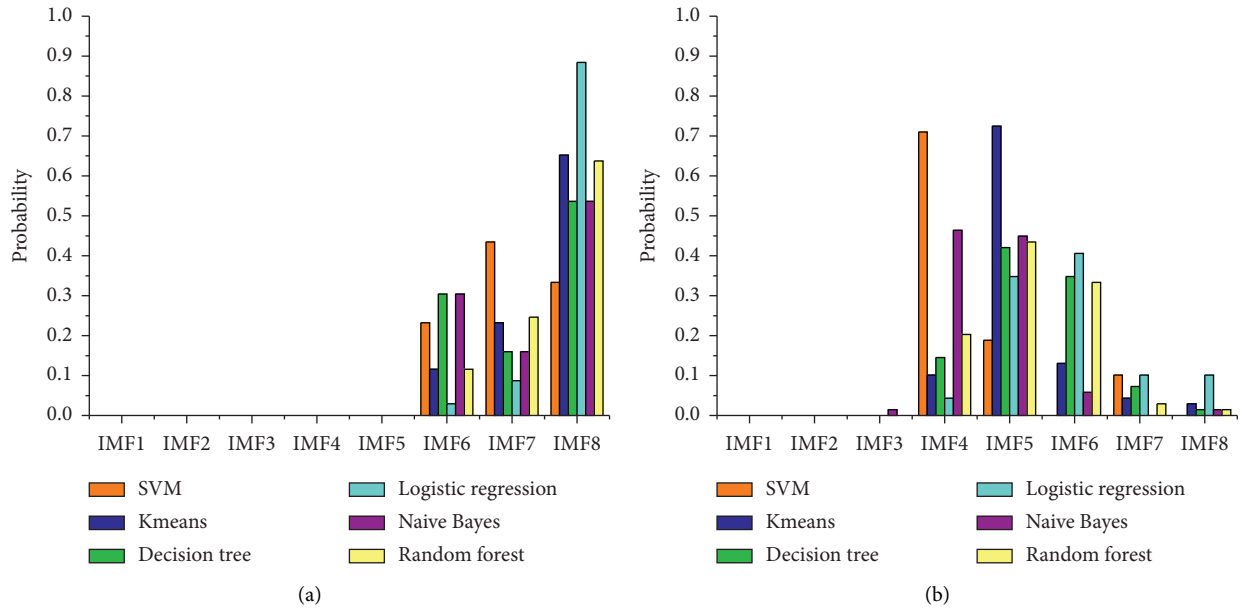


FIGURE 6: Maximum probability that each IMF contributes to the recognition accuracy on gait recognition mode B. (a) With exoskeleton. (b) Without exoskeleton.

and without wearing exoskeleton. This shows again that gait locomotion mode may change between wearing exoskeleton and without wearing exoskeleton.

In general, the result of this section tells us that when we tend to utilize someone’s gait data on the normal floor as the model to recognize the same subject’s gait in other materials, Kmeans may be a more helpful algorithm to analyze gait recognition among the six algorithms. Also, IMF8 may be more helpful for analyzing gait recognition when subjects

walk with exoskeleton on flat floor, and meanwhile IMF5 may be more useful to recognize gait among IMF1 ~ IMF8 when subjects walk without exoskeleton on flat floor.

3.3. *Gait Recognition Mode C Results.* The results of gait recognition mode C that the decomposing data of the original data as IMF1 ~ IMF8 for the same floor material and various subjects can be analyzed from Figure 7. Tables 5 and 6 show the elaborate information for Figure 7. In this

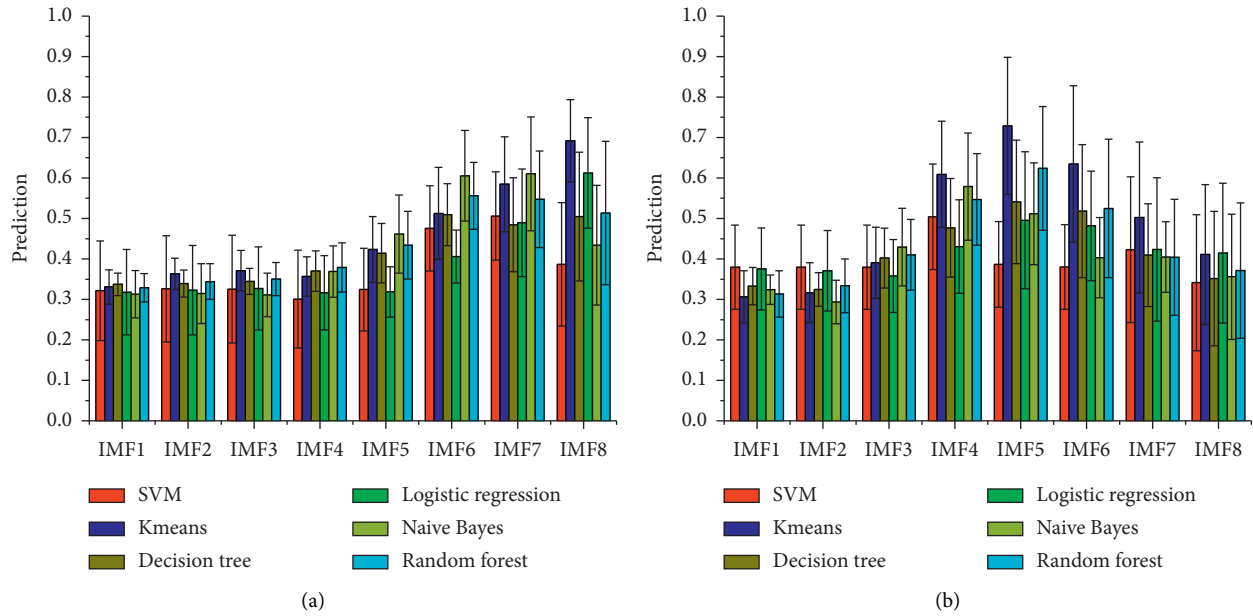


FIGURE 7: Gait recognition results of gait recognition mode *C* based on the IMFs of the original signal for the 14 subjects walking on flat floors with different friction situations. (a) With exoskeleton. (b) Without exoskeleton.

TABLE 4: Gait recognition accuracy of gait recognition mode *B* based on the IMFs of the original signal for the 14 subjects who walked without exoskeletons (mean \pm SD%).

Component	SVM	Kmeans	Decision tree	Logistic regression	Naive Bayes	Random forest
IMF1	36.85 \pm 10.04	35.14 \pm 4.86	34.36 \pm 3.22	36.72 \pm 9.81	34.13 \pm 4.66	35.12 \pm 4.68
IMF2	36.88 \pm 10.09	35.94 \pm 4.75	35.99 \pm 3.83	37.04 \pm 9.81	32.89 \pm 5.35	36.67 \pm 5.22
IMF3	37.27 \pm 10.31	44.75 \pm 9.79	43.39 \pm 8.43	36.77 \pm 8.89	43.37 \pm 12.52	45.98 \pm 10.36
IMF4	63.27 \pm 14.92	71.30 \pm 13.18	58.90 \pm 10.17	48.55 \pm 12.15	69.78 \pm 12.30	67.57 \pm 11.58
IMF5	51.14 \pm 18.31	80.24 \pm 12.68	65.07 \pm 13.16	63.80 \pm 16.31	70.29 \pm 13.26	72.85 \pm 12.66
IMF6	39.60 \pm 10.32	69.88 \pm 17.20	61.95 \pm 17.14	64.91 \pm 13.19	55.16 \pm 14.47	68.83 \pm 14.67
IMF7	45.20 \pm 13.34	50.94 \pm 15.79	45.98 \pm 12.26	51.83 \pm 11.52	42.92 \pm 11.51	45.78 \pm 14.22
IMF8	37.52 \pm 10.29	48.20 \pm 20.72	43.78 \pm 13.13	48.74 \pm 14.82	40.31 \pm 9.48	43.88 \pm 12.93

TABLE 5: Gait recognition accuracy for gait recognition mode *C* based on the IMFs of the original signal for the 14 subjects who wore exoskeletons to walk (mean \pm SD%).

Component	SVM	Kmeans	Decision tree	Logistic regression	Naive Bayes	Random forest
IMF1	32.14 \pm 12.32	33.08 \pm 4.23	33.73 \pm 2.78	31.77 \pm 10.56	31.30 \pm 5.86	32.86 \pm 3.52
IMF2	32.61 \pm 13.14	36.33 \pm 3.85	33.92 \pm 3.34	32.30 \pm 11.05	31.44 \pm 7.39	34.41 \pm 4.39
IMF3	32.53 \pm 13.30	37.09 \pm 5.00	34.45 \pm 3.22	32.71 \pm 10.26	31.11 \pm 5.36	35.01 \pm 4.08
IMF4	30.08 \pm 12.06	35.67 \pm 4.84	37.00 \pm 4.99	31.62 \pm 9.19	36.87 \pm 6.33	37.90 \pm 6.11
IMF5	32.45 \pm 10.20	42.35 \pm 8.11	41.41 \pm 7.34	31.86 \pm 6.24	46.13 \pm 9.66	43.40 \pm 8.38
IMF6	47.53 \pm 10.52	51.25 \pm 11.39	50.92 \pm 7.65	40.57 \pm 6.55	60.54 \pm 11.20	55.60 \pm 8.28
IMF7	50.59 \pm 10.91	58.46 \pm 11.73	48.44 \pm 11.60	48.94 \pm 13.30	61.02 \pm 14.07	54.75 \pm 11.94
IMF8	38.65 \pm 15.24	69.18 \pm 10.20	50.49 \pm 15.91	61.25 \pm 13.64	43.37 \pm 14.80	51.35 \pm 17.74

mode, we can compare the performance of different machine learning algorithms when we establish the recognition model by one subject experiment session and recognize gait with the same floor material in different subjects.

When it comes to the performance of IMF1 \sim IMF8 while wearing an exoskeleton in Figure 7(a) and Table 5, Kmeans is also the best algorithm compared to others and IMF8 contains the highest accuracy among IMF1 \sim IMF8 with Kmeans (69.18%). In Figure 7(b) and Table 6, we can

see that Kmeans performs best and IMF5 gets the highest accuracy among IMF1 \sim IMF8 with Kmeans (72.87%).

Furthermore, Figure 8 shows the probability for IMF1 \sim IMF8 that each IMF may be the highest accuracy among IMF1 \sim IMF8 for the six algorithms. In Figure 8(a), we could say that the most likely to get the maximum accuracy among IMF1 \sim IMF8 when wearing exoskeleton is IMF7 and IMF8 especially for Kmeans, Decision tree, logistic regression, and random forest. From Figure 8(b), we

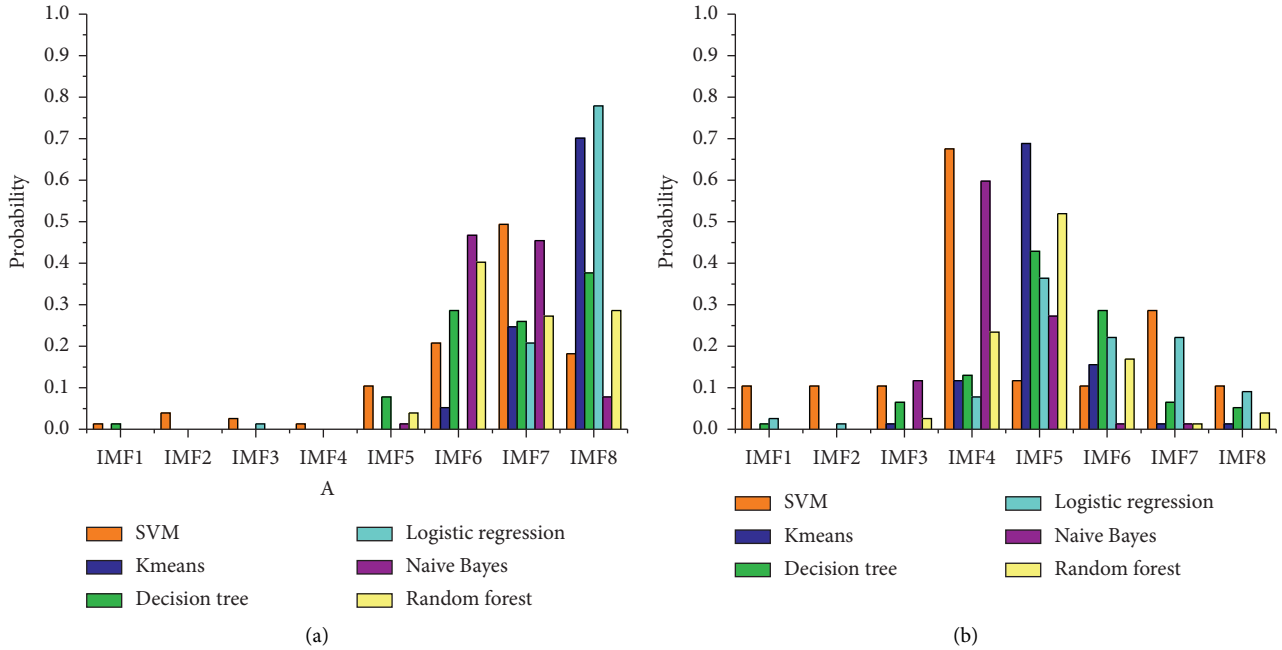


FIGURE 8: Maximum probability that each IMF contributes to the recognition accuracy of gait recognition mode C. (a) With exoskeleton. (b) Without exoskeleton.

TABLE 6: Gait recognition accuracy for gait recognition mode C based on the IMFs of the original signal for the 14 subjects who walked without exoskeletons (mean ± SD%).

Component	SVM	Kmeans	Decision tree	Logistic regression	Naive Bayes	Random forest
IMF1	37.96 ± 10.39	30.65 ± 6.43	33.30 ± 4.62	37.53 ± 10.16	32.38 ± 3.62	31.35 ± 5.74
IMF2	37.96 ± 10.39	31.65 ± 7.41	32.46 ± 4.15	37.09 ± 9.95	29.37 ± 5.37	33.37 ± 6.64
IMF3	37.96 ± 10.39	39.06 ± 8.80	40.21 ± 7.41	35.76 ± 9.01	42.92 ± 9.60	41.02 ± 8.74
IMF4	50.43 ± 13.04	60.88 ± 13.13	47.69 ± 12.17	43.07 ± 11.55	57.88 ± 13.25	54.70 ± 11.32
IMF5	38.65 ± 10.57	72.87 ± 16.95	54.08 ± 15.26	49.54 ± 16.93	51.17 ± 12.55	62.38 ± 15.30
IMF6	38.00 ± 10.47	63.47 ± 19.32	51.82 ± 16.42	48.16 ± 13.55	40.32 ± 9.91	52.48 ± 17.08
IMF7	42.30 ± 18.02	50.23 ± 18.64	40.93 ± 12.69	42.34 ± 17.73	40.47 ± 8.71	40.40 ± 14.34
IMF8	34.13 ± 16.80	41.09 ± 17.28	35.15 ± 16.60	41.45 ± 17.29	35.60 ± 15.47	37.13 ± 16.72

can see that IMF4 ~ IMF6, especially IMF5 can get the maximum accuracy among IMF1 ~ IMF8 when walking without exoskeleton.

In sum, from the result of mode C, we could generalize that when we try to recognize various subjects' gait based on another subject with the same floor materials, Kmeans may be better to perform gait recognition among the six algorithms on mode C. IMF8 may be more helpful for analyzing gait recognition when subjects walk with exoskeleton on flat floor, and meanwhile IMF5 may be more useful to recognize gait among IMF1 ~ IMF8 when subjects walk without exoskeleton on flat floor. This is the same as mode B.

3.4. Correlation Analysis between IMF Components and Original Gait. As addressed in previous gait recognition results, we see that there might be potential evident correlation between the latter IMFs and the original signals. Now the aforementioned nonlinear fitting approach is adopted to investigate the trajectory correlation between the

latter IMFs and the original signals. Table 7 shows the VAF results for finding correlation between the IMF combination and the original gait signals acquired from the VICON system on the 14 subjects in part one experiments and IMU sensors on the 3 subjects in part two experiments. We can see that IMF4 ~ IMF8 of some combinations can be used to identify the original gait signals. It reveals that the combination of IMFs may be utilized to identify the original gait trajectory.

3.5. Joint Synergy Results. In addition to gait motion recognition results, in order to investigate the possible similarity of joint synergy, we performed PCA on the five joints: elbow, shoulder, hip, knee, and ankle joints, to extract the principal components which can represent joint synergy indexes. For these five joints on X axis, from Figure 9, we could see the comparison on the joint synergy for the subjects who walk with and without exoskeleton.

TABLE 7: VAF_n^m for evaluating correlation between IMF combinations and original gait signal captured by VICON and IMU sensors (mean \pm SD%).

Correlation	VICON	IMU
VAF^1	55.11 \pm 944.89	94.1 \pm 5.4
VAF^2	41.94 \pm 945.09	98.7 \pm 1.7
VAF^3	95.78 \pm 65.56	98.9 \pm 1.2
VAF^4	99.09 \pm 11.44	98.9 \pm 1.2
VAF^5	-20782.26 \pm 870032.49	96.81 \pm 7.28
VAF^6	98.71 \pm 33.32	99.7 \pm 0.3

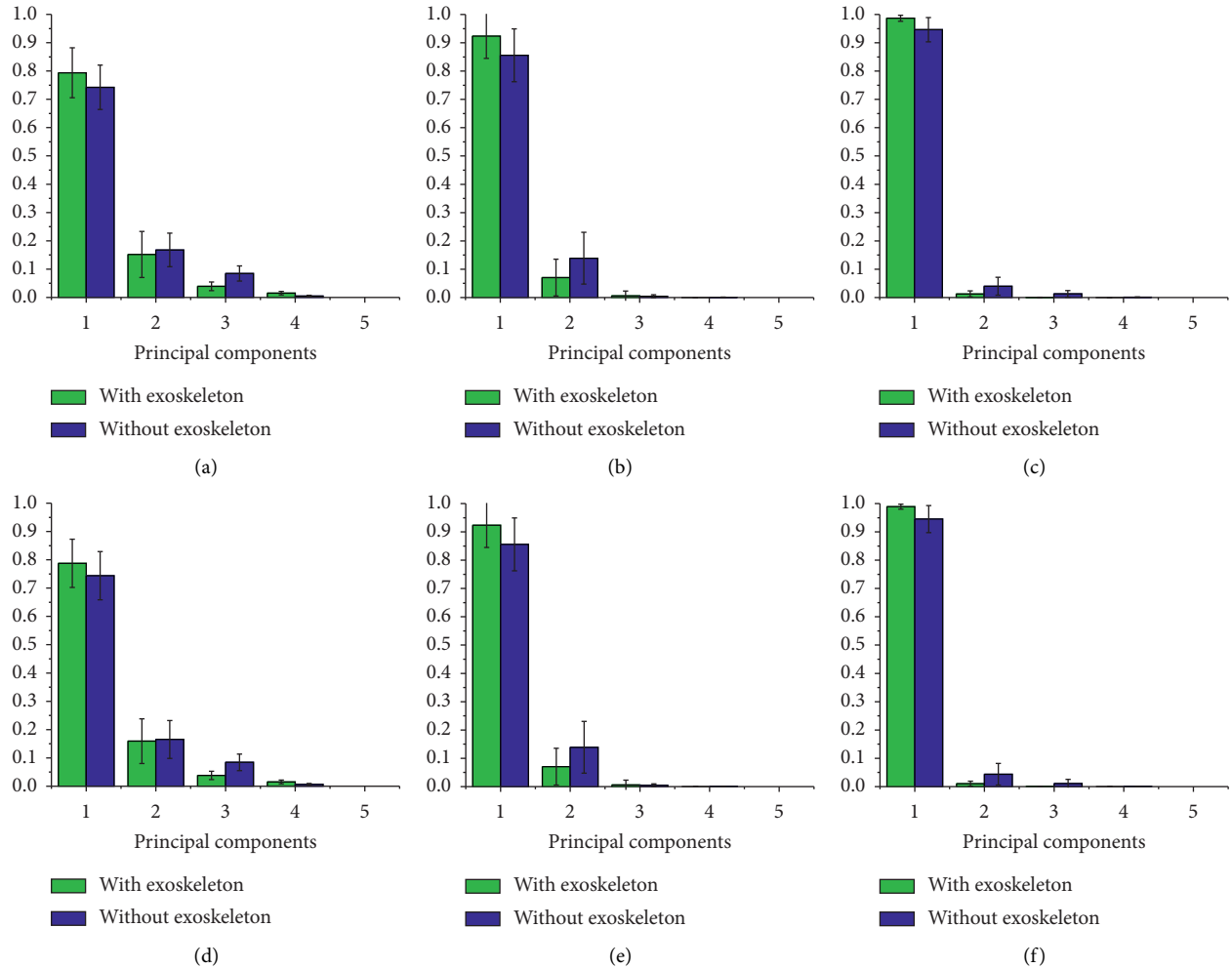


FIGURE 9: Normalized PCA of the joint synergy of five joints. (a) Left side joints on X axis. (b) Left side joints on Y axis. (c) Left side joints on Z axis. (d) Right side joints on X axis. (e) Right side joints on Y axis. (f) Right side joints on Z axis.

In Figures 9(a)–9(c), the first average principal components without exoskeletons on X , Y , and Z axes of left side joints are, respectively, 74.24%, 85.59%, and 94.63%, and the first average principal components with exoskeletons on X , Y , and Z axes of left side joints are, respectively, 79.38%, 92.36%, and 98.67%. In Figures 9(d)–9(f), the first average principal components without exoskeletons on X , Y , and Z axes of right side joints are, respectively, 74.39%, 85.89%, and 94.52%, and the first average principal components with exoskeletons on X , Y , and Z axes of right side joints are, respectively, 78.76%, 92.64%, and 98.92%. The second

principal components also show different values for the two groups on the left side and right side joints. It can be seen that when the subjects wear exoskeletons to walk, such PCA-based synergy extraction results show that the principal components can be altered.

4. Conclusions

In this paper, EEMD-based gait recognition modes A , B , and C are proposed for the human-exoskeleton system. SVM (support vector machine), Kmeans, decision tree, logistic

regression, Naive Bayes, and random forest methods are used as training algorithms for such framework, and the performance of these six algorithms is discussed. Thus, we estimate how various algorithms, IMF order number, different floor materials, and various subjects would affect the result of recognition. And the results show that when it comes to gait recognition among various subjects and various floor materials, Kmeans might be better on performance whenever with or without wearing exoskeleton. For the contribution of gait recognition with IMF1 ~ IMF8 among various subjects and various floor materials, IMF8 might be helpful when wearing exoskeleton, and IMF5 might be useful when walking without exoskeleton. And floor materials have little influence on gait recognition.

The correlation of original gait data and their decomposing signal IMFs through EEMD is investigated, which reveals that the combination of IMFs may be utilized to identify the original gait trajectory.

At last, joint synergy of five joints for the subjects who walked with and without exoskeletons is also drawn, which showed that the joint synergy might change between with and without wearing exoskeleton.

Data Availability

The VICON and IMU data used to support the findings of this study were supplied by Jing Qiu under license and so cannot be made freely available. Requests for access to these data should be made to Jing Qiu, qiuqing@uestc.edu.cn.

Conflicts of Interest

The authors declare that they have no conflicts of interest.

Acknowledgments

This work was supported by the National Natural Science Foundation of China (no. U19A2082), the Sichuan Major Scientific and Technological Special Project (no. 2018GZDZX0037), and the Fundamental Research Funds for the Central Universities (no. ZYGX2019Z010).

References

- [1] E. Aertbelien and J. D. Schutter, "Learning a predictive model of human gait for the control of a lower-limb exoskeleton," in *Proceedings of the 5th IEEE RAS/EMBS International Conference on Biomedical Robotics and Biomechatronics*, pp. 520–525, Sao Paulo, Brazil, August 2014.
- [2] J. O. Brinker, T. Matsubara, T. Teramae et al., "Walking pattern prediction with partial observation for partial walking assistance by using an exoskeleton system," in *Proceedings of the 2015 IEEE International Conference on Rehabilitation Robotics (ICORR)*, pp. 139–144, Singapore, August 2015.
- [3] D. Kim, D. Kim, and J. Paik, "Gait recognition using active shape model and motion prediction," *IET Computer Vision*, vol. 4, no. 1, pp. 25–36, 2010.
- [4] D. Torricelli, C. Cortés, N. Lete et al., "A subject-specific kinematic model to predict human motion in exoskeleton-assisted gait," *Frontiers in Neurobotics*, vol. 12, p. 18, 2018.
- [5] Z. Li, M. Hayashibe, D. Andreu, and D. Guiraud, "Real-time closed-loop fes control of muscle activation with evoked emg feedback," in *Proceedings of the 2015 7th International IEEE/EMBS Conference On Neural Engineering (NER)*, pp. 623–626, IEEE, Montpellier, France, April 2015.
- [6] Z. Li, W. Zuo, and S. Li, "Zeroing dynamics method for motion control of industrial upper-limb exoskeleton system with minimal potential energy modulation," *Measurement*, vol. 163, Article ID 107964, 2020.
- [7] Z. Li, C. Li, S. Li, and X. Cao, "A fault-tolerant method for motion planning of industrial redundant manipulator," *IEEE Transactions on Industrial Informatics*, vol. 99, 2019.
- [8] Z. Li, H. Liu, Z. Yin, and K. Chen, "Muscle synergy alteration of human during walking with lower limb exoskeleton," *Frontiers in Neuroscience*, vol. 12, p. 1050, 2019.
- [9] S. Wen, F. Wang, C. Wu, and Y. Zhang, "Gait data de-noising based on improved Emd," in *Proceedings of the 2010 Chinese Control and Decision Conference*, pp. 2766–2770, Xuzhou, China, May 2010.
- [10] S. Chandra, M. Hayashibe, and A. Thondiyath, "Empirical mode decomposition-based filtering for fatigue induced hand tremor in laparoscopic manipulation," *Biomedical Signal Processing and Control*, vol. 31, pp. 339–349, 2017.
- [11] X. Cui, C.-K. Peng, M. D. Costa, A. Weiss, A. L. Goldberger, and J. M. Hausdorff, "Development of a new approach to quantifying stepping stability using ensemble empirical mode decomposition," *Gait & Posture*, vol. 39, no. 1, pp. 495–500, 2014.
- [12] P. Ren, S. Tang, F. Fang et al., "Gait rhythm fluctuation analysis for neurodegenerative diseases by empirical mode decomposition," *IEEE Transactions on Biomedical Engineering*, vol. 64, no. 1, pp. 52–60, 2017.
- [13] N. Wang, E. Ambikairajah, B. G. Celler, and N. H. Lovell, "Accelerometry based classification of gait patterns using empirical mode decomposition," in *Proceeding of the 2008 IEEE International Conference on Acoustics, Speech and Signal Processing*, pp. 617–620, Las Vegas, NV, USA, March 2008.
- [14] Virtualization Documentation, "Full body modeling with plug in gait," <https://docs.vicon.com/pages/viewpage.action?pageId=50888852>.
- [15] M. Hassan, H. Kadone, K. Suzuki, and Y. Sankai, "Exoskeleton robot control based on cane and body joint synergies," in *Proceedings of the 2012 IEEE/RSJ International Conference on Intelligent Robots and Systems*, pp. 1609–1614, Algarve, Portugal, October 2012.
- [16] S. Senda, N. Takata, and K. Tsujita, "A study on lower limb's joint synergy in human locomotion with physical constraints on the knee," in *Proceedings of the 2012 IEEE/SICE International Symposium on System Integration (SII)*, pp. 349–354, Fukuoka, Japan, December 2012.

Research Article

Vaginal Secretions Epithelial Cells and Bacteria Recognition Based on Computer Vision

Shaozhi Guo ¹, Haoyuan Guan ², Jianzhong Li ^{1,3}, Yonghua Liao ⁴,
Weiwen Zhang ⁵ and Shengqiang Chen ⁶

¹School of Automation, Guangdong University of Technology, Guangzhou 511436, China

²Guangdong Institute of Scientific & Technical Information, Guangzhou, China

³Research Institute of Integrated Circuit Innovation, Guangdong University of Technology, Guangzhou 511436, China

⁴School of Basic Medical Sciences, Guangzhou Medical University, Guangzhou 511436, China

⁵Third Affiliated Hospital of Guangzhou Medical University, Guangzhou, China

⁶Department of Applied Psychology, Guangzhou Medical University, Guangzhou 511436, China

Correspondence should be addressed to Weiwen Zhang; zhangweiwen@gzhmu.edu.cn and Shengqiang Chen; shengqiangchen@gzhmu.edu.cn

Received 15 September 2020; Revised 23 October 2020; Accepted 10 November 2020; Published 2 December 2020

Academic Editor: Zhan Li

Copyright © 2020 Shaozhi Guo et al. This is an open access article distributed under the Creative Commons Attribution License, which permits unrestricted use, distribution, and reproduction in any medium, provided the original work is properly cited.

The examination of vaginal secretions epithelial is of great importance to female reproductive health. The results of manual detection will be affected by subjective judgment and fatigue. In this paper, an identification method based on computer vision is proposed to identify vaginal secretions epithelial cells and some bacteria. The experimental results demonstrate that the method can significantly distinguish the vaginal secretions epithelial cells from the bacteria and virus.

1. Introduction

Vaginitis is one of the most common diseases in women. It brings burning sensation and pain to the affected areas, and, even worse, it will cause symptoms of general discomfort and reduce the immune function of people, resulting in other complications [1]. The examination of the vaginal secretions is necessary to help to discover vaginal lesions early and to implement timely and effective treatment to patients. The vaginal secretions are mainly examined using Gram staining. After the steps of making smear, drying, fixing, and staining, with counting the number of cells and bacteria in the smear, the state of vaginal microecological environment can be preliminarily judged [2, 3]. Moreover, the health situation of reproductive system can be predicted.

The results of Gram staining microscopy of vaginal secretions provide important information for the diagnosis of vaginal health [4]. However, counting results relies

heavily on the professionalism, as well as the state of the operators. The results provided by different operators would be quite different. And even for the same operator, the results may not be the same at different time. Therefore, an automatic system should be required to detect efficiently cells and bacteria in vaginal secretions Gram stained smear images.

The automatic recognition of cells or bacteria has been attracting the attention of scholars from all over the world. Yi-De Ma et al. used the logical and morphological feature of blood cell images to count the number of cells [5]. Jacey-Lynn Minoi et al. developed an image processing technique on smart mobile App, which can detect and isolate colonies on real environment by shape, color, and other morphological features [6]. However, with the above methods, it may be difficult to achieve good recognition results for the objects with fuzzy edge and low contrast with the background, especially those with irregular shape and area. Aslı Genctav et al. proposed an

unsupervised method based on a multiscale hierarchical segmentation algorithm and binary classifier for the separation of nuclei in cervical cell image [7]. Kuan Li et al. proposed a method named Radiating Gradient Vector Flow (RGVF) Snake that can more accurately extract the contours of nucleus and cytoplasm in cervical smear images [8]. However, both works are carried out on images with relative simple content and could not provide a good effect in smear images of vaginal secretions with complex content including impurities. Machine learning algorithms have been also introduced to detect cell in recent years [9–11]. However, these algorithms need an experimental training step, which is difficult to achieve due to the lack of label data of cell images. Moreover, indeterminacy of manual annotation of class label can greatly affect the accuracy of machine learning algorithms [12].

The content of vaginal secretions smear images includes cytoplasts, nuclei, cells (completely composed by cytoplasm and nucleus), bacteria, and impurities. In this paper, we propose a dual process and nucleus-cytoplasm cross verification method to recognize vaginal secretions epithelial cells in vaginal secretions smear images. The number of the cells can be counted, which works as the feedback. In addition, the method can generate pixel-level label data of vaginal secretions epithelial cells and bacteria rapidly and efficiently, which can be used in model training process of machine learning or deep learning, reducing the manual burden of labeling medical images.

The rest of this paper is organized as follows. Section 2 analyses the smear images. The realization of recognition method is shown in Section 3. Then, Section 4 gives the experimental results. Section 5 presents the discussion and conclusion.

2. Image Analysis

The vaginal secretions smear images used in this paper were provided by the Third Affiliated Hospital of Guangzhou Medical University. The vaginal secretions were observed with gram stain in white back-light illumination. Figure 1 shows several kinds of objects in the smear images, which can be divided into targets and jamming information. According to the recognition requirements, the targets include nuclei, cells, and bacteria, while the jamming information includes cytoplasts, impurities, and background.

The features of the objects in vaginal secretions smear images are explained in the following:

- (1) Nucleus. Nucleus may be inside a cell as a part of it, or outside. Its color is dark purple after Gram stain, and its shape is ideally round or oval but sometime strange shape. Generally, the area is between 40 and 250 pixels.
- (2) Bacterium. A bacterium is much smaller than nucleus with slender shape, in dark purple, randomly distributed in the image and may appear in the regions of background or a cell.
- (3) Cell. A cell consists of nucleus and cytoplasm with an area greater than 500 pixels, of which the color is red

distinct from nucleus. Due to the uneven distribution of intracellular substances, there is Gaussian noise in the region of cytoplasm [13].

- (4) Cytoplast. The only difference between a cell and a cytoplast is that there is no nucleus in the cytoplast.
- (5) Impurity. In addition to all kinds of physiological objects, there are impurities in the cell smear, such as bubbles, black spots, and staining agent residues, which are close to the cell or nucleus in morphology.
- (6) Background. The image light source is white back-light. Thus, the background is a uniform and high brightness area in white and is brighter than other areas.

3. Recognition Method

The recognition targets are cells and bacteria. However, in order to recognize effective cells, it is necessary to recognize the cytoplast as well as the nucleus. Some bacteria and nuclei may overlap with the cytoplasmic, and the image information of bacteria and nuclei will be covered up when the cytoplasmic image information is enhanced for extracting the cytoplasmic regions. Therefore, in order to obtain the information of bacteria and cells more effectively and simultaneously, a dual process structure is adopted. The regions of cells and bacteria are separately extracted in one process and the regions of cytoplasm are extracted in the other one [14, 15]. After that, the regions of nuclei and cytoplasm are verified mutually to distinguish cells from cytoplasts and impurities. Figure 2 outlines the overall flow.

The original image is a color image using RGB color model to store data. There are three decimal values from 0 to 1 representing the brightness of red, green, and blue in each pixel. The recognition results are reflected by generated binary images marking the regions of interest (ROI) with true value and other regions with false value.

3.1. Process for Cells and Bacteria. The steps to detect nuclei and bacteria can be found as follows.

Step 1. Separating the red component from a color image as gray-scale image for weakening cytoplasm information: the cytoplasm is stained red, which hardly blocks the light in the red. As a result, the cytoplasm information in the red component of original image is less than that in the blue and green components. In conclusion, using red component for graying can effectively weaken the information of cytoplasm, highlight the information of nuclei and bacteria, and reduce the amount of data to 1/3.

Step 2. Segment background by threshold segmentation: the gray values of background and cytoplasm is higher than that of bacteria and nuclei. Therefore, threshold segmentation is used to segment ROI:

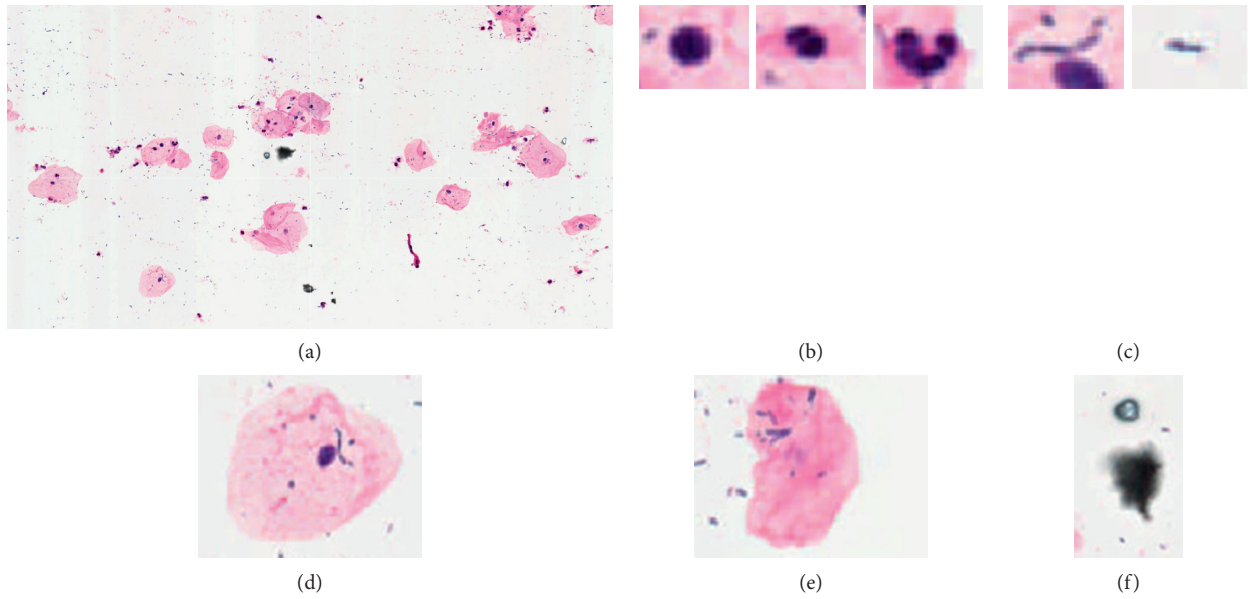


FIGURE 1: A part of a smear image and the content of it: (a) original image, (b) nuclei, (c) bacteria, (d) cell, (e) cytoplasm, and (f) impurities.

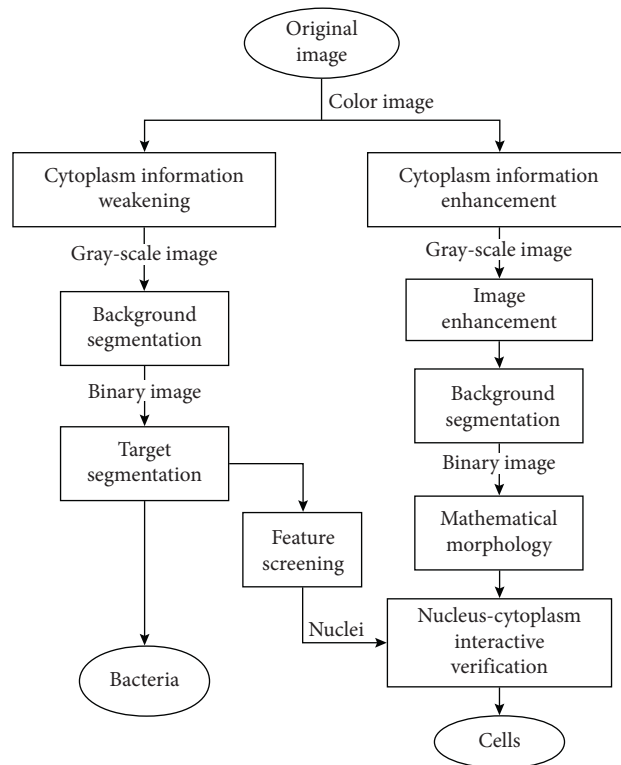


FIGURE 2: Overall flow.

$$B(x, y) = \begin{cases} 1, & \text{if } f(x, y) \leq T, \\ 0, & \text{if } f(x, y) > T, \end{cases} \quad (1)$$

where f is the gray-scale image from Step 1 and T is a fixed threshold value.

Step 3. Isolate bacteria for targets segmentation through morphological operation and complement operation: first, it is primary to label the connected components in the binary image from Step 2 forming a label matrix. And then, the opening arithmetic of mathematical morphology is used to eliminate small connected components:

$$L_N = (L \ominus b) \oplus b, \quad (2)$$

where b is the structuring element, L is the label matrix, \ominus is the erosion operation, and \oplus is the dilation operation. The ROI binary image of bacteria can be generated by complement operation:

$$S = C_{\{|l| \in L\}} \{l_n | l_n \in L_N\},$$

$$B_B(x, y) = \begin{cases} 1, & \text{if } L(x, y) \in S, \\ 0, & \text{else.} \end{cases} \quad (3)$$

Step 4. Filter targets through area feature: as the area of a cell is between 50 and 250 pixels, it is helpful to calculate the connected component areas and remove the regions with more than 250 pixels or fewer than 50 pixels:

$$L'_N(x, y) = \begin{cases} L_N(x, y), & \text{if } 50 < n_{L_N(x, y)} < 250, \\ 0, & \text{else,} \end{cases} \quad (4)$$

$$B_N(x, y) = \text{sgn}(L'_N(x, y)),$$

where n_i is the number of i label and sgn is the symbolic function.

After the above steps, the binary image of bacteria B_B and that of nuclei B_N are obtained.

3.2. Process for Cytoplasm. The steps to obtain the regions of cytoplasm are described as follows.

Step 1. Gray the original image using green component for cytoplasm information enhancement.

Step 2. Enhance image with Gaussian filtering: there is Gaussian noise in the region of cytoplasm due to the uneven staining. It is necessary to apply Gaussian filtering, and the result is shown in Figure 3. The image enhancement step is not applied in process for cells and bacteria. In contrast to cytoplasm containing a large number of moistures, which lead to the uneven staining, bacteria can be evenly stained. In fact, the Gaussian filter will undermine the contour information of bacteria in image instead as can be seen in Figure 3.

Step 3. Segment Background by weighted Otsu [16] threshold segmentation: since the cytoplasm is not as dark as the nucleus and its gray value is related to the staining effect, the weighted Otsu algorithm is used to obtain the adaptive segmentation threshold, which should be in the valley part of the gray histogram:

$$T_w = w \times \arg\max [p_B(\mu_B - \mu)^2 + p_O(\mu_O - \mu)^2],$$

$$B(x, y) = \begin{cases} 1, & \text{if } f(x, y) \leq T_w, \\ 0, & \text{else,} \end{cases} \quad (5)$$

where f is the gray-scale image from Step 2, w is the weight, p_B and μ_B are the probability distribution and the gray mean of background regions, and p_O and μ_O are that of object regions. Through numerous experiments, when the weight is 1.1, the cytoplasm regions can be segmented from the background very well.

Step 4. Remove irrelevant regions by mathematical morphology: opening arithmetic is used to remove the bacteria regions in the binary image from Step 3. The edges of ROIs can be deburred as well through the operation:

$$B_p = (B \ominus b) \oplus b, \quad (6)$$

where B is the binary image and b is the structuring element.

After the above steps, the binary image of cytoplasm B_p is generated.

3.3. Nucleus-Cytoplasm Cross Verification. In fact, the binary image of cytoplasm includes the regions of cells, cytoplasts, free nuclei without enough cytoplasm, and impurities, while the binary image of nuclei includes the regions of nuclei and impurities with the area between 50 and 250 pixels. To distinguish cells from cytoplasts and meanwhile eliminate the interference of impurities, the nucleus-cytoplasm cross verification is designed as follows.

Step 1. Label the connected components in the binary image of cytoplasm so that the corresponding region can be operated by the label value.

Step 2. Set up a set of regions containing nuclei: the elements in the set are the label values of regions with nuclei:

$$S_N = \{l_N | l_N \in L_p \cdot B_N\}. \quad (7)$$

Step 3. Set up a set of regions with enough cytoplasm area: after removing the regions of nuclei from the regions of cytoplasm, the quantity of each label value is calculated as the area of corresponding region. Then, those label values with the quantity greater than 500 will become the element of the set:

$$S_p = \{l_p | l_p \in L_p \cdot (1 - B_N), n(l_p) > 500\}, \quad (8)$$

where $n(i)$ is the quantity of the label value i .

Step 4. According to the sets, reserve the regions with nucleus and with enough area of cytoplasm:

$$S_C = S_N \cap S_p,$$

$$B_C(x, y) = \begin{cases} 1, & \text{if } L_p(x, y) \in S_C, \\ 0, & \text{else.} \end{cases} \quad (9)$$

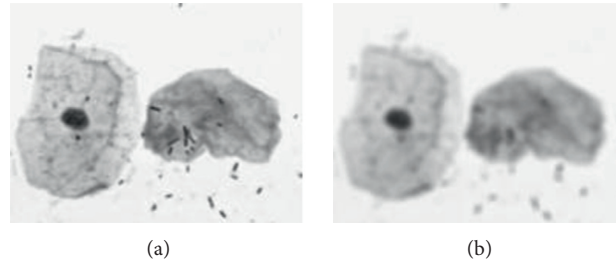


FIGURE 3: The effect of Gaussian filtering: (a) before filtering and (b) after filtering.

After all of the above steps, the binary images of cells and bacteria are separately obtained. The number of cells and bacteria can be obtained by counting the number of connected components.

4. Experimental Result

An image with a size of 1920 pixels * 1024 pixels is selected for the experiment. The results of each step in the process for cells and bacteria are shown in Figures 4–6. Those in the process for cytoplasm are shown in Figures 7 and 8, and the results of cross verification are shown in Figure 9.

As shown in Figure 4, the regions of cytoplasm are similar to the background region in the gray-scale image of (b), which is formed of the red component of the original image of (a). Therefore, it is possible to segment the regions without background and cytoplasm of (c) using a fixed threshold.

As shown in Figure 5, by opening arithmetic of mathematical morphology, the regions of bacteria are removed leaving the regions without bacteria of (a), while the regions of bacteria of (b) are formed of those eliminated regions.

In view of the fact that the area of nucleus is between 50 and 250 pixels, area filtering is used to remove the regions of impurities, and the result is shown in Figure 6.

Figure 7 shows the results of the enhancement of cytoplasm information, in which the gray value of the regions of cytoplasm is lower than that of background regions after enhancement of cytoplasm by graying image using the green component and noise reduction by Gaussian filtering.

For the sake of segmentation of background, the weighted Otsu threshold is adopted, which, as shown in Figure 8, is at the valley of the gray histogram of (a). As a result, the segmentation regions of (b) remain the regions of cytoplasm very well. After a morphological opening operation to remove regions of bacteria, the regions of cytoplasm of (c) are obtained.

As shown in Figure 9, the cross verification firstly removes the regions of nuclei from regions of cytoplasm and reserves the regions with an area greater than 500 pixels of (a). Then, the regions of nuclei are used again to reserve the regions with nuclei, the regions of cells of (b).

Marking the original image with the mark of region contours of cells in red, that of bacteria in blue, and that of nuclei in green, the effect is shown in Figure 10, where the bacteria and cells are significantly distinguished from cytoplasts, free nuclei, and impurities.

The results of each object are shown in Figures 11–16. The results of free nucleus in Figure 11 suggest that the nuclei are not mistaken for bacteria, and the free nuclei will not be misidentified as cells during cross verification due to the insufficient of cytoplasm. The results of bacterium in Figure 12 show that bacteria can be identified correctly. The results of cell in Figure 13 indicate that, as the regions of cells include both the regions of nuclei and cytoplasm, it can be identified correctly, and the regions of bacteria can be obtained without hindrance. The results of cytoplast in Figure 14 show that as a result of the lack of nucleus, the regions of cytoplasts are removed in cross verification. The results also demonstrate that cells and cytoplasts can be distinguished well with the cross verification. The results of impurities in Figures 15 and 16 suggest that, in the case that the areas of impurities are similar to the cells, the impurities would be removed as nuclei, due to the fact that regions of the impurities are reserved in the regions of both nuclei and cytoplasm resulting in insufficient area of cytoplasm in cross verification. In other cases, the impurities would be removed like cytoplasts for the lack of regions of nuclei owing to the area filtering step.

5. Discussion and Conclusion

For assisting in the diagnosis of vaginal health, a dual process and nucleus-cytoplasm cross verification method is proposed in this paper to identify bacteria and cells in vaginal secretions Gram stained smear images. The proposed method can effectively distinguish bacteria and cells from impurities, free nuclei, and cytoplasts and extract regions of bacteria and cells, respectively, which can be used to count the generate pixel-level label data of vaginal secretions epithelial cells and bacteria.

The proposed method was designed according to the features of nuclei, bacteria, cells, cytoplasts, and impurities after Gram stain. Therefore, the method is not applicable in the cases of images made with other techniques or containing other objects. The method is considered to be able to recognize other cells in different smear images with some adjustments, provided the images belong to the applicable cases. Because of the constant color feature of Gram stain and the morphology difference between cells, by modifying the upper and lower limit of nucleus area of Step 4 in process for cells and bacteria and adjusting the threshold for cytoplasm area of Step 3 in nucleus-cytoplasm cross verification, the proposed method can be suitable for a new smear image.

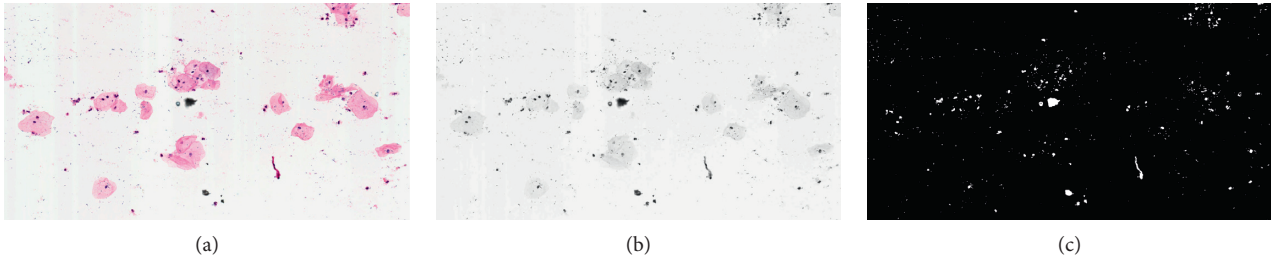


FIGURE 4: Results of separating regions without background and cytoplasm: (a) original image, (b) gray-scale image with weakened cytoplasm, and (c) regions without background and cytoplasm.



FIGURE 5: Results of separating regions of bacteria: (a) regions without bacteria and (b) regions of bacteria.

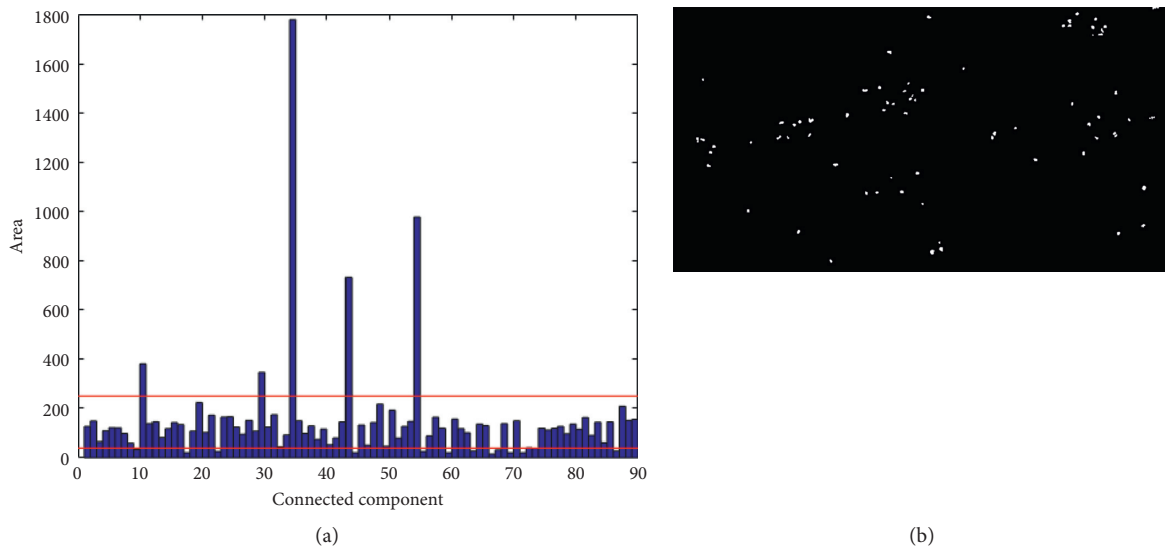


FIGURE 6: Result of area filtering: (a) area histogram of the regions without bacteria and (b) regions of nuclei.

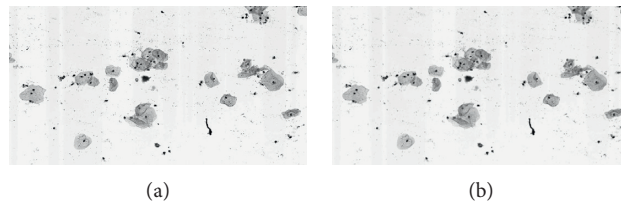


FIGURE 7: The results of enhancement of cytoplasm information: (a) gray-scale image with enhanced cytoplasm and (b) image after Gaussian filtering.

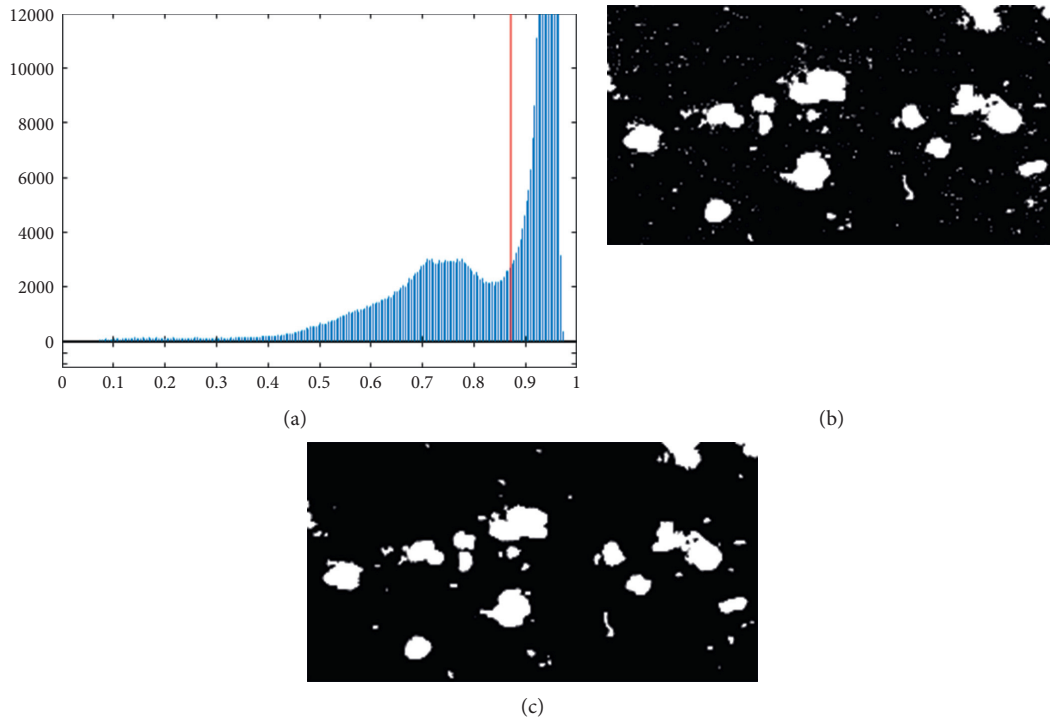


FIGURE 8: Result of segmentation: (a) gray histogram and threshold, (b) segmentation regions, and (c) regions of cytoplasm.



FIGURE 9: Result of cross verification: (a) the regions with area greater than 500 pixels and (b) the region of cells.

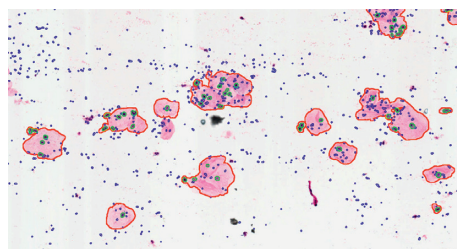


FIGURE 10: Final effect image.

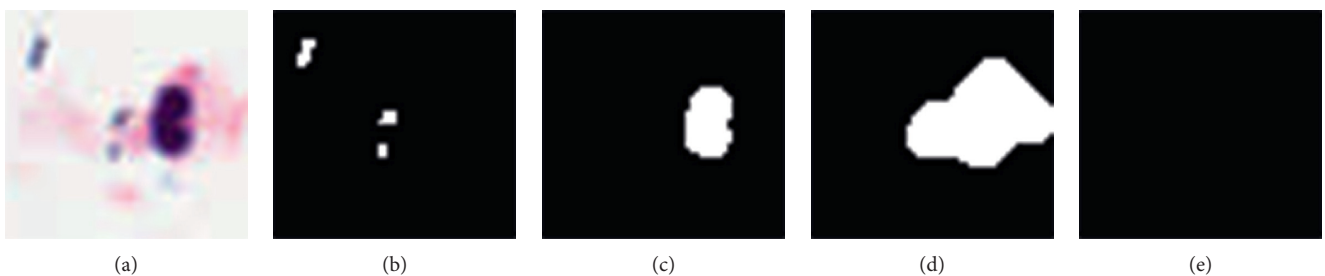


FIGURE 11: The results of free nucleus: (a) original image, (b) regions of bacteria, (c) region of nucleus, (d) region of cytoplasm, and (e) region of cell.

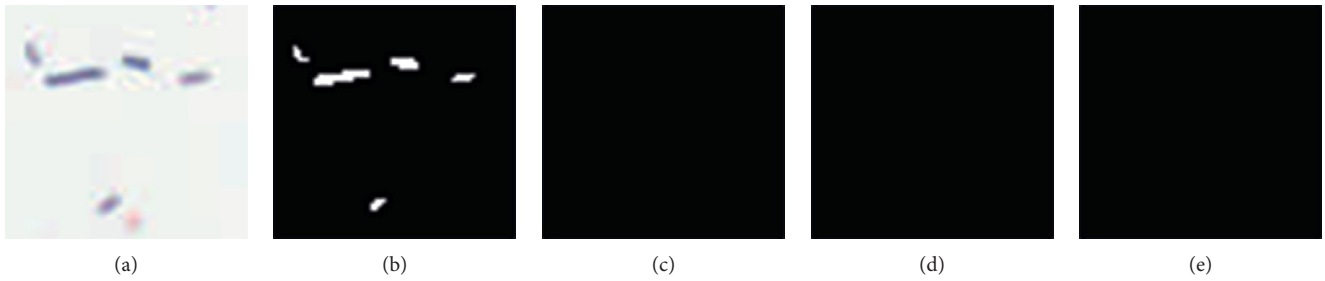


FIGURE 12: The results of bacterium: (a) original image, (b) regions of bacteria, (c) region of nucleus, (d) region of cytoplasm, and (e) region of cell.

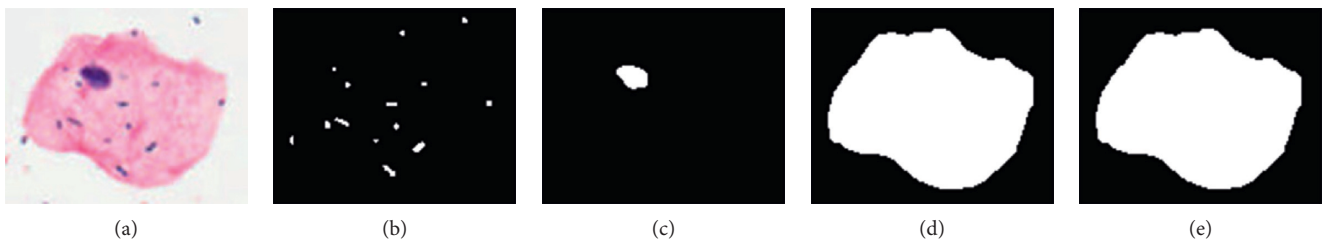


FIGURE 13: The results of cell: (a) original image, (b) regions of bacteria, (c) region of nucleus, (d) region of cytoplasm, and (e) region of cell.

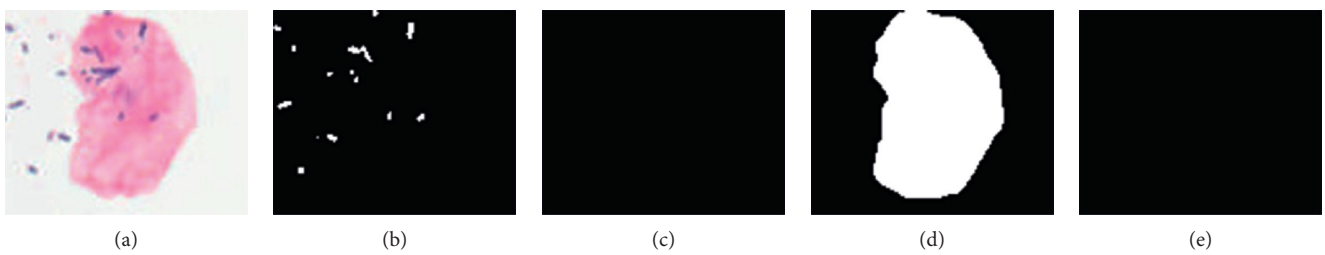


FIGURE 14: The results of cytoplasm: (a) original image, (b) regions of bacteria, (c) region of nucleus, (d) region of cytoplasm, and (e) region of cell.

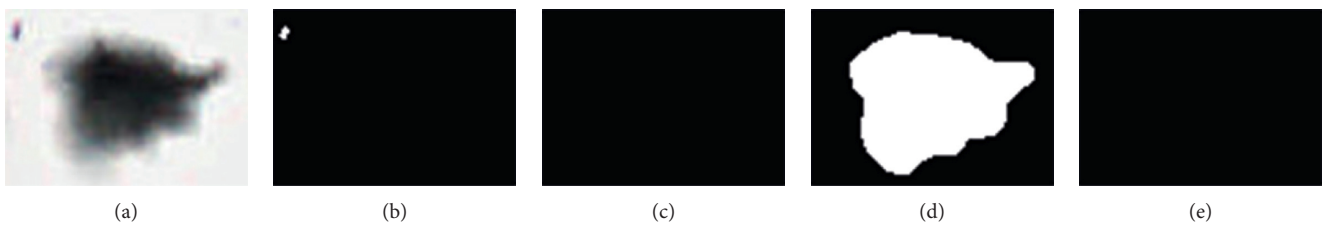


FIGURE 15: The results of large impurity: (a) original image, (b) region of bacterium, (c) region of nucleus, (d) region of cytoplasm, and (e) region of cell.

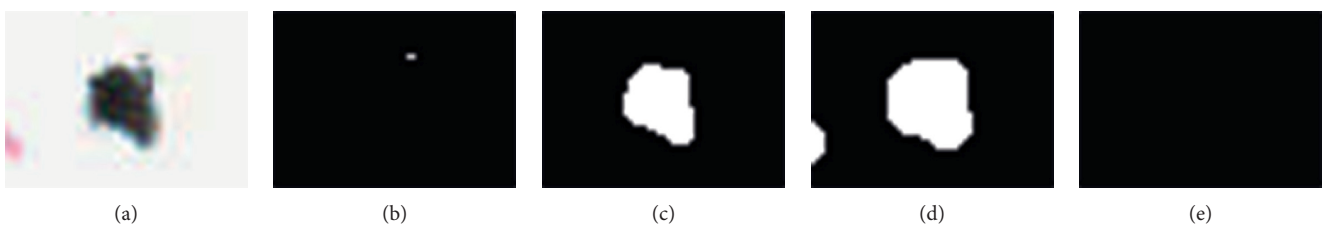


FIGURE 16: The results of nucleus like impurity: (a) original image and (b) region of bacterium (c) region of nucleus, (d) region of cytoplasm, and (e) region of cell.

Data Availability

The raw data required to reproduce these findings cannot be shared at this time as the data are concerned with personal conceal.

Disclosure

Shaozhi Guo and Haoyuan Guan are co-first authors.

Conflicts of Interest

The authors declare that they have no conflicts of interest.

Authors' Contributions

Shaozhi Guo and Haoyuan Guan contributed equally to this work.

Acknowledgments

This work was supported by the Key-Area Research & Development Program of Guangdong Province under grant no. 2019B010145001 and the Science & Technology Program of Guangdong under grant no. 2019A141401005.

References

- [1] S. M. Kovachev, "Obstetric and gynecological diseases and complications resulting from vaginal dysbacteriosis," *Microbial Ecology*, vol. 68, no. 2, pp. 173–184, 2014.
- [2] J. Ravel, P. Gajer, Z. Abdo et al., "Vaginal microbiome of reproductive-age women," *Proceedings of the National Academy of Sciences*, vol. 108, no. Supplement_1, pp. 4680–4687, 2011.
- [3] C. A. Spiegel, R. Amsel, and K. K. Holmes, "Diagnosis of bacterial vaginosis by direct gram stain of vaginal fluid," *Journal of Clinical Microbiology*, vol. 18, no. 1, pp. 170–177, 1983.
- [4] R. P. Nugent, M. A. Krohn and S L. Hillier, "Reliability of diagnosing bacterial vaginosis is improved by a standardized method of gram stain interpretation," *Journal of Clinical Microbiology*, vol. 29, no. 2, pp. 297–301, 1991.
- [5] Y. Ma, R.-L. Dai, L. Lian, and Z.-F. Zhang, "An counting and segmentation method of blood cell image with logical and morphological feature of cell," *Chinese Journal of Electronics*, vol. 11, no. 1, 2002.
- [6] J. L. Minoi, T. T. Chiang, T. Lim, Z. Yusoff, and A. Zulharnain, "Mobile vision-based automatic counting of bacteria colonies," in *2016 International Conference on Information and Communication Technology (ICICTM)*, IEEE, Kuala Lumpur, Malaysia, April 2017.
- [7] A. Gençtav, S. Aksoy, and S. Önder, "Unsupervised segmentation and classification of cervical cell images," *Pattern Recognition*, vol. 45, no. 12, pp. 4151–4168, 2012.
- [8] K. Li, Z. Lu, W. Liu, and J. Yin, "Cytoplasm and nucleus segmentation in cervical smear images using radiating gvf snake," *Pattern Recognition*, vol. 45, no. 4, pp. 1255–1264, 2012.
- [9] J. Zhang, S. Lu, X. Wang et al., "Automatic identification of fungi in microscopic leucorrhoea images," *Journal of the Optical Society of America A*, vol. 34, no. 9, p. 1484, 2017.
- [10] L. Zhou, L. Wang, Z. Gao, and J. Zhang, "HEp-2 cell image classification with convolutional neural networks," in *2014 1st Workshop on Pattern Recognition Techniques for Indirect Immunofluorescence Images*, IEEE, Stockholm, Sweden, December 2014.
- [11] C.-J. Tseng, C.-J. Lu, C.-C. Chang, and G.-D. Chen, "Application of machine learning to predict the recurrence-proneness for cervical cancer," *Neural Computing and Applications*, vol. 24, no. 6, pp. 1311–1316, 2014.
- [12] A. Torralba and A. A. Efros, "Unbiased look at dataset bias," in *Computer Vision & Pattern Recognition CVPR 2011*, IEEE, Providence, RI, USA, August 2011.
- [13] W. Liping and L. Renren, "Red blood cell recognition based on bp neural networks," *Computer & Digital Engineering*, vol. 46, no. 3, 584 pages, 2018.
- [14] R. M. Haralick, S. R. Sternberg, and X. Zhuang, "Image analysis using mathematical morphology," *IEEE Transactions on Pattern Analysis and Machine Intelligence*, vol. 9, no. 4, pp. 532–550, 1987.
- [15] M. Sezgin and B. Sankur, "Survey over image thresholding techniques and quantitative performance evaluation," *Journal of Electronic Imaging*, vol. 13, no. 1, pp. 146–168, 2004.
- [16] N. Otsu, "A threshold selection method from gray-level histograms," *IEEE Transactions on Systems, Man, and Cybernetics*, vol. 9, no. 1, pp. 62–66, 1979.

Research Article

Application of the Improved PSO-Based Extended Domain Method in Engineering

Bin Bai ^{1,2}, Zhi-wei Guo,³ Qi-liang Wu ⁴, Junyi Zhang,^{1,2} and Yan-chao Cui ⁵

¹State Key Laboratory of Reliability and Intelligence of Electrical Equipment, Hebei University of Technology, Tianjin 300401, China

²School of Mechanical Engineering, Hebei University of Technology, Tianjin 300401, China

³Shenyang Engine Research Institute, Shenyang 110015, China

⁴School of Electrical Engineering and Automation, Tiangong University, Tianjin 300387, China

⁵AVIC Tianjin Aviation Electromechanical Co., Ltd., Tianjin 300308, China

Correspondence should be addressed to Yan-chao Cui; duji2008@126.com

Received 21 May 2020; Revised 22 July 2020; Accepted 29 July 2020; Published 7 September 2020

Guest Editor: Jing Guo

Copyright © 2020 Bin Bai et al. This is an open access article distributed under the Creative Commons Attribution License, which permits unrestricted use, distribution, and reproduction in any medium, provided the original work is properly cited.

The standard particle swarm optimization (PSO) algorithm is the boundary constraints of simple variables, which can hardly be directly applied in the constrained optimization. Furthermore, the standard PSO algorithm often fails to obtain the global optimal solution when the dimensionality is high for unconstrained optimization. Thus, an improved PSO-based extended domain method (IPSO-EDM) is proposed to solve engineering optimization problems. The core idea of this method is that the original feasible region is expanded in the constrained optimization which is transformed into the unconstrained optimization by combining the ergodicity of chaos optimization and the evolutionary variation to realize global search. In addition, to verify the effectiveness of the IPSO-EDM, an unconstrained optimization case study, four constrained optimization case studies, and one engineering example are investigated. The results indicate that the computational accuracy of the IPSO-EDM is comparable to that provided by the existing literature, and the computational efficiency of the IPSO-EDM is significantly improved. Meanwhile, this method has conspicuous global search ability and stability in engineering optimization.

1. Introduction

Optimization began in the 17th century, which originated from differential and integral calculus invented by Newton and Leibnitz. Then, optimization algorithms [1–5] were rapidly developed, such as artificial neural network, simulated annealing, genetic algorithm, ant colony optimization, and particle swarm optimization (PSO). All these methods were widely used in different fields [6–12], such as chemical engineering, biomedicine, navigation, robot, automobile, architecture, and aerospace.

Actually, the mechanical engineering optimization can be expressed as continuity interval constraint optimization. To investigate this problem, some traditional gradient methodologies [13–15] were investigated such as the penalty function and Lagrange multiplier. Although the theory of

these methods is impeccable, the objective function and the constraint condition must be differentiable. However, the constraint function and objective function are non-differentiable and discontinuous implicit functions in practical engineering. Consequently, a new optimization method was developed to study this problem, which plays an important role for the development of engineering optimization design.

Initially, the PSO was presented by Kennedy and Eberhart [16] to investigate the flight behaviour of birds, which was termed as the global PSO algorithm. This method has been extended to different kinds of fields. For instance, Xue et al. [17] used analytical method with modified PSO to establish the subdomain model and optimize cogging torque. Han et al. [18] adopted an adaptive gradient multiobjective PSO to improve the computational

performance for a mechanism. Yi et al. [19] presented a parallel chaotic local search algorithm to solve constrained engineering design problems. Park et al. [20] used chaotic sequences with conventional linearly decreasing inertia weights to increase the exploitation capability. However, the essence of these methods is not improved, thus some scholars renewed the equation of the global PSO. For instance, Phung et al. [21] proposed a discrete PSO algorithm to solve the extended travelling salesman problem for robotic inspection. Wang and Zhang [22] presented an optimization method to describe a planar parallel 3-DOF nano positioner in modelling. Nickabadi et al. [23] successfully regarded the adaptive inertia weight factor as the feedback parameter to ascertain the situation of the particles in the search space. Mojarrad and Nayeripour [24] used a fuzzy adaptive PSO to solve the non-convex economic dispatch problems. Khan et al. [25] proposed a modified PSO algorithm to avoid the premature convergence and strengthen its robustness. This algorithm can adaptively update parameters to keep the diversity of the swarm. However, the convergence speed of inertia weight method is not very fast, so another method is developed. Liang et al. [26] proposed a fuzzy multilevel algorithm-based PSO to optimize support vector regression machine and realize a fuzzy multilevel drilling leak risk evaluation system. Tian et al. [27] utilized sigmoid-based acceleration coefficients to avoid premature convergence and entrapment into local optima when they handled complex multimodal problems. Hsieh et al. [28] developed a discrete cooperative coevolving PSO algorithm to study the influence of detour distance constraints on the carpooling performance. Zahara et al. [29, 30] put forward the hybrid Nelder-Mead-PSO algorithm for unconstrained optimization, and then they presented embedded constraint handling methods for dealing with constraints. Liu et al. [31] adopted a bottleneck objective learning strategy for many-objective optimization to improve convergence on all objectives. Xia et al. [32] proposed a triple archives PSO to deal with the selecting proper exemplars and designing an efficient learning model. Wang et al. [33] investigated the evolutionary computation community for large-scale optimization.

The above investigations on the PSO algorithm indicate that some constrained points are not located in the feasible region but outside the feasible region; however, these excluded constrained points are closer to the boundary than the points located in the feasible region. Obviously, this is unreasonable. Based on the above research studies, a new methodology named improved particle swarm optimization-based extended domain method (IPSO-EDM) is proposed to investigate engineering optimization.

In the following, Section 2 describes the basic theory of the IPSO-EDM, including standard PSO, improved PSO, and the algorithm principle. Section 3 gives an unconstrained optimization case study, four numerical constrained optimization case studies, and one engineering case study to verify the effectiveness of the IPSO-EDM. Section 4 gives the conclusions.

2. Improved Particle Swarm Optimization

2.1. Standard PSO. Assuming that the particle swarm is composed of M particles in an N -dimensional space, the position of the i th particle of the k th iteration is expressed as $\mathbf{X}_i(k) = (x_{i1}(k), x_{i2}(k), \dots, x_{iN}(k))^T$, the flight speed is described as $\mathbf{V}_i(k) = (v_{i1}(k), v_{i2}(k), \dots, v_{iN}(k))^T$, the local optimal position is $\mathbf{P}_i = (p_{i1}, p_{i2}, \dots, p_{iN})^T$, and the global optimal location is $\mathbf{P}_g = (p_{g1}, p_{g2}, \dots, p_{gN})^T$. Each particle updates its speed and position according to the following equation, which are expressed as

$$\begin{aligned} v_{ij}(k+1) &= v_{ij}(k) + c_1 r_{1j} \times [p_{ij}(k) - x_{ij}(k)] + c_2 r_{2j} \\ &\quad \times [p_{gj}(k) - x_{ij}(k)], \\ x_{ij}(k+1) &= x_{ij}(k) + v_{ij}(k+1), \end{aligned} \quad (1)$$

where j is the j th component of the i th particle, c_1 and c_2 are positive constants and they are called learning factor, c_1 adjusts the step length for particles to their optimal location, and c_2 adjusts the step length for particles to the global optimal position, and r_{1j} and r_{2j} are, respectively, random numbers that obey a uniform distribution, and their values are within $[0, 1]$.

To prevent particles from flying out of the search space in the optimization, the velocity and position are limited as $v_{ij} \in [v_{j\min}, v_{j\max}]$ and $x_{ij} \in [x_{j\min}, x_{j\max}]$. Meanwhile, the inertia weight w is involved. This method is termed as the standard PSO algorithm. The update equations are expressed as

$$\begin{aligned} v_{ij}(k+1) &= w(k) \times v_{ij}(k) + c_1 r_{1j} \times [p_{ij}(k) - x_{ij}(k)] \\ &\quad + c_2 r_{2j} \times [p_{gj}(k) - x_{ij}(k)], \\ x_{ij}(k+1) &= x_{ij}(k) + v_{ij}(k+1). \end{aligned} \quad (2)$$

The standard PSO does not have too many requirements on the objective function and constraint function, which can conduct constraint optimization, and these constraints limit the range of each variable interval value such as $x_j \in [x_{j\min}, x_{j\max}]$. This is different from the gradient method, but it becomes more complicated if there are equality or inequality constraints in the optimization. One obvious reason is that the feasible region has changed from a hypercube to a less regular region, and the variables are not independent on each other. For this reason, the standard PSO must be improved to deal with the constraints.

2.2. Improved PSO

2.2.1. Constraint Methods of PSO. At present, there are four typical methods to deal with constraints:

- (1) Discriminant function method: inequality and equality constraints are used as discriminant functions to determine whether the search points are feasible points in the optimization process. It will be discarded or modified to be a feasible point during search if the search point is not a feasible point. Thus,

this method has strict restrictions to the search point, and it is very difficult to generate the initial feasible point when the feasible region composed by equality and inequality constraints is small.

- (2) Penalty function method: the optimization and constraint functions are combined to form the penalty function. The original constrained optimization with equality and inequality constraints has become an unconstrained optimization with the penalty function. However, the disadvantage of this method is that the penalty factor must be chosen correctly; otherwise, it can hardly obtain the optimal solution.
- (3) Multiobjective optimization method: optimization and constraint functions are, respectively, used as the new optimization targets. However, solving the multiobjective optimization is more difficult than solving a single-objective optimization in many cases.
- (4) “Competitive selection” method: deals with the feasible particles (the design points represented by particles satisfy all constraint requirements) and infeasible particles (some or all design points represented by particles dissatisfy the optimization constraint requirements) in PSO. However, it is not appropriate to deem that feasible particles are superior to infeasible ones in competitive selection, and the infeasible region can be extended into a feasible region to find the optimal point.

2.2.2. *Core Idea of the “Competitive Selection” Constraint.* The “competitive selection” constraint can be summarized in three aspects:

- (1) All feasible particles are superior to infeasible particles
- (2) The particle with a better objective function is selected for two feasible particles
- (3) The advantages and disadvantages of the particle are judged according to the degree of constraint violation for two infeasible particles; the lesser the degree of the constraint, the larger the violation

In Figure 1(a), unconstrained optimal point A is in the feasible region, and the constraint is useless to the whole optimization; essentially, the constrained optimal point is the unconstrained optimal point. However, the unconstrained optimal point is not located in the feasible region but at its boundary for some optimization. For example, point B is the constrained optimal point, point C is in the feasible region, and point D is outside the feasible region in Figure 1(b). According to the competitive selection, point C is superior to D . However, point D is closer to B than C ; thus, the optimal information provided by D is superior to C . As a result, point D is labelled as suboptimal, which is not appropriate. So, the algorithm must be improved. Figure 1(c) shows an improved method, which expands the original feasible region to include points such as D which is

unfeasible but close to the feasible region and can provide better function information and is taken as the feasible point. This methodology is termed as extended domain method (EDM).

In addition, the new speed depends on the current speed in the updated formula for standard PSO. However, the algorithm is random, and it is impossible to predict and control the size of particle speed. To solve this problem, a control variable ξ is introduced in the extended domain, and the result is shown in Figure 2, where \mathbf{x}^* is the optimal location, \mathbf{x} is the current particle position, \mathbf{p}_g is the optimal historical position of the particle swarm, \mathbf{p}_x is the optimal historical position of the current particle, $\hat{\mathbf{x}}$ is the optimal location of the current particle swarm, and \mathbf{v}_l and \mathbf{v}_s are, respectively, the largest and smallest speeds.

Figure 2 shows that the particle with higher speed may miss a better position, while the particle with smaller speed improves the position, but it is not the optimal position. Thus, the current particle speed is expected to be controlled. One method is to use current location information of the particle swarm to determine its speed. The difference value between the particle swarm and the particle in the current optimal position is used to determine current particle velocity. The results indicate that the position \mathbf{x}_x determined using this method is better than the positions \mathbf{x}_l and \mathbf{x}_s . In fact, the constrained optimization is transformed into an unconstrained optimization by the EDM, so a scientific and reasonable unconstrained optimization method needs to be developed.

2.2.3. *Unconstrained PSO.* Firstly, the initial particle swarm position and velocity are determined in a random way in standard PSO. Generally, the designers expect the particles in the particle swarm space can better reflect the information which is studied in the initial state. One of the direct ways is to generate many particles which fill in the whole search space. However, this will consume a lot of computational resources in subsequent iterations. The PSO algorithm will lose its characteristics of group cooperation if the number of particles in the particle swarm space is too small, which is meaningless. Usually, the particle swarm with dozens of particles can solve the complex optimization problem, but random arrangements of particles often result in a “cluster” in an area. To enable the particles to be relatively “evenly” distributed in the search space, the uniform design method based on statistical theory is used to initialize the particle swarm space. The random distribution and uniform distribution of the initial particle swarm space are shown in Figure 3.

Secondly, the standard PSO algorithm itself cannot obtain global information of the objective function, and it is easy to fall into the local optimal. Generally, the particle can jump out of the local optimal and give new global information by dynamically adjusting the inertia factor, but simply adjusting the inertia factor is not enough for the complex multipeak function. To handle this problem, the ergodicity of chaos optimization [22] is combined with evolutionary variation to realize global search. In this

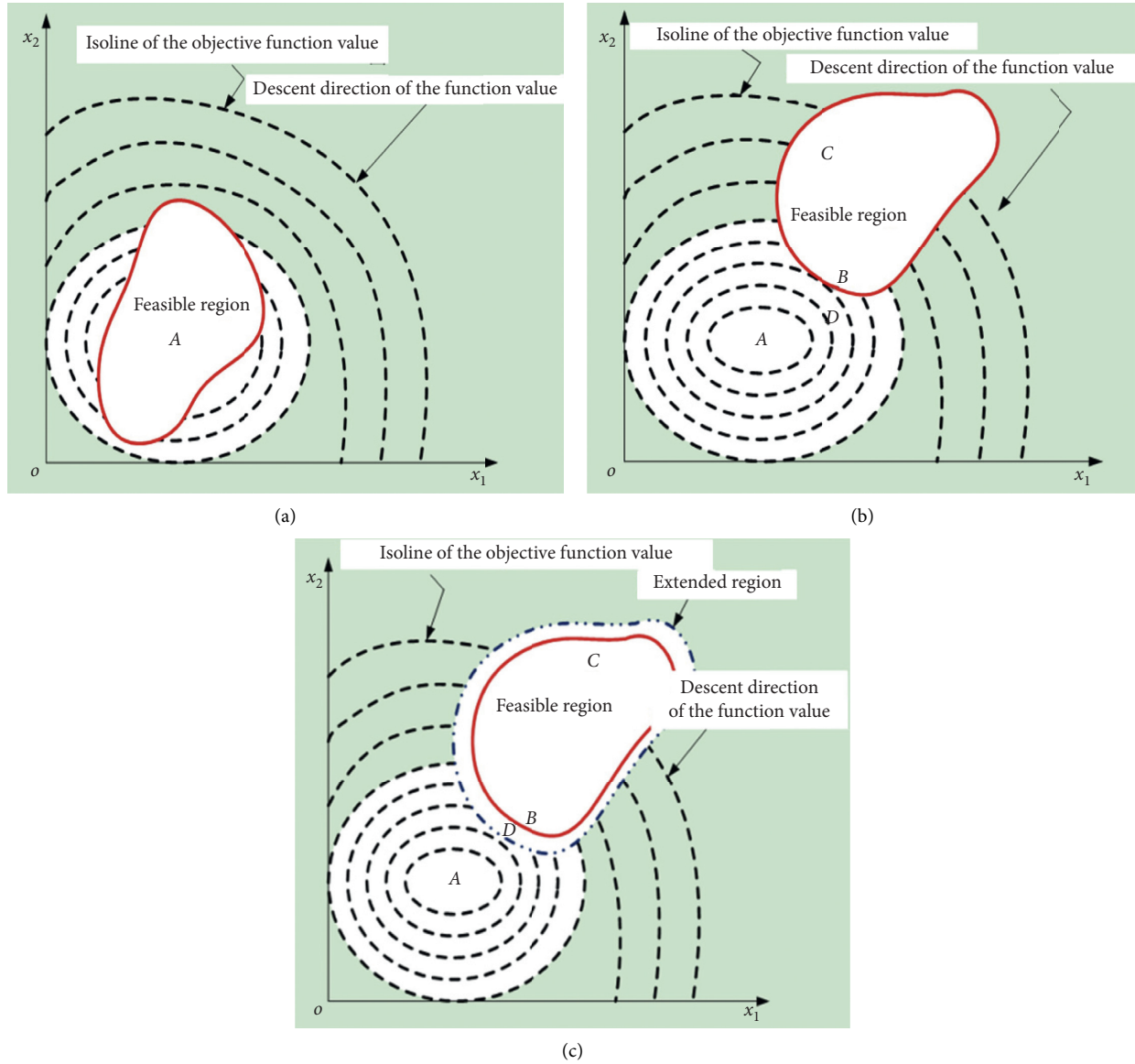


FIGURE 1: Relationship among the optimal point, feasible domain, and extended domain: (a) optimal point in the feasible region; (b) optimal point outside the feasible region; (c) optimal point in the extended domain.

method, logistic chaotic system equation is applied in the PSO algorithm and obeys Chebyshev distribution, as shown in Figure 4.

Figure 4 indicates that the middle value of the logistic chaotic sequence is relatively uniform, while the probability of both sides is relatively large. It means that the chance of finding the global optimal point will be reduced using the logistic chaotic sequence if the global optimal point is not at ends of the design variable. Therefore, it is very necessary to find a chaotic sequence, which can not only maintain ergodicity but also keep uniform statistical distribution. According to this problem, evolutionary variation strategy is developed. Generally, this strategy introduces a mutation operator to change the design variable. This method can help the particle swarm escape local optimal and maintain its overall vitality and prevent the particle swarm from falling

into the condition of “precocity” at the earlier iteration. Based on the above research, the idea of uniform design, chaos optimization, and evolutionary variation is introduced into unconstrained PSO, and this method is improved to realize global search and local search.

Firstly, the uniform design of the Halton sequence [34] is adopted to initialize the particle swarm. Assume that the particle position scope of the j th design variable is $[x_{j\min}, x_{j\max}]$, whose component values of the i th particle are h_{ij} , and the position x_{ij} of the initialized particle swarm is expressed as

$$x_{ij}(0) = x_{j\min} + (x_{j\max} - x_{j\min}) \times h_{ij}. \quad (3)$$

Similarly, the velocity v_{ij} for the j th component values of the i th particle is expressed as

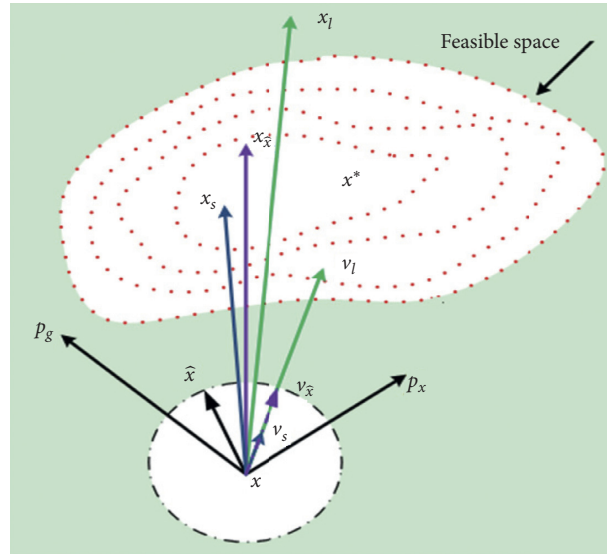


FIGURE 2: Renewal schematic diagram of the particle position.

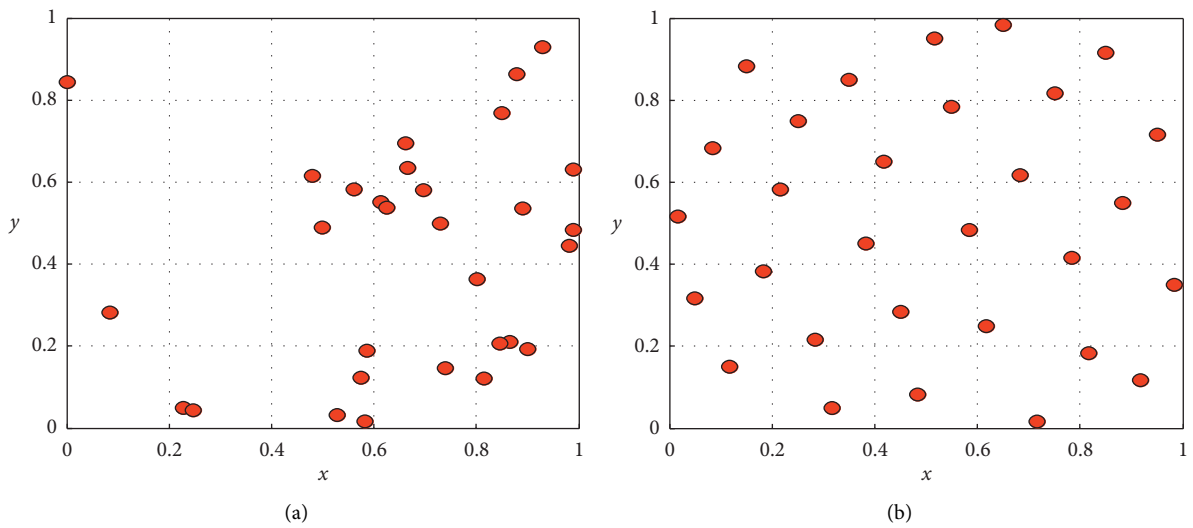


FIGURE 3: Distribution diagram of the initial particle swarm space: (a) random distribution; (b) uniform distribution.

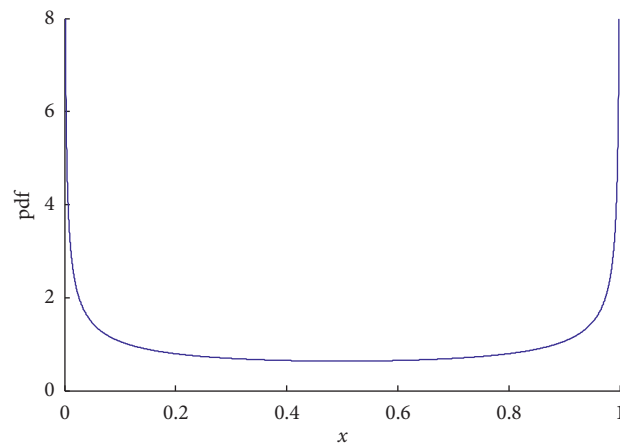


FIGURE 4: Probability density curve of the logistic chaotic sequence.

$$v_{ij}(0) = v_{j\min} + (v_{j\max} - v_{j\min}) \times h_{ij}. \quad (4)$$

In the process of particle swarm evolution, the points around the optimal position still need to be searched to get a better position when the optimal position of the particle swarm is found. This is called as the chaos optimization search method, which is expressed as

$$z(l+1) = 1 - \mu \times z(l)^2. \quad (5)$$

However, the chaotic sequence generated by equation (5) is not uniform in statistics; therefore, the chaotic sequence needs to be transformed as follows:

$$t(l) = \frac{\arccos[z(l)]}{\pi}. \quad (6)$$

Equation (6) not only satisfies the ergodicity of the chaotic sequence but also complies with the uniform distribution in $[0, 1]$. The uniform logistic chaotic sequence and original logistic chaotic sequence of the frequency curve and ergodic graph are shown in Figures 5 and 6. The point set of the chaotic sequence is $1e4$.

The optimal position of the particle swarm is denoted as $\mathbf{P}_g(k)$ after the k th evolution, and the i th component is denoted as $p_{gi}(k)$; then, the initial value of the chaotic sequence is expressed as

$$z_i(0) = \frac{p_{gi}(k) - x_{i\min}}{x_{i\max} - x_{i\min}}. \quad (7)$$

According to equations (5) and (6), the chaotic sequence $z_i(l)$, $l = 1, 2, \dots, m$, is generated, and its coordinate value corresponding to the original space is obtained via reverse transformation, which is expressed as

$$\bar{p}_i(l) = x_{i\min} + (x_{i\max} - x_{i\min}) \times z_i(l), \quad (8)$$

where l is the number of iterations of the chaotic sequence and k is the number of iterations.

However, the chaos optimization can hardly make particle swarm get rid of local optimal, and the evolutionary variation is used to help it jump out local optimal. The mutation operator plays a key role in evolutionary variation. The Gaussian operator and Cauchy operator are two commonly used mutation operators. The global searching ability of the Cauchy mutation is stronger than that of the Gaussian mutation, but Cauchy mutation may produce large stride length in search, which means its local search ability is not as good as that of the Gaussian mutation. Therefore, according to the characteristics of Cauchy variation and Gaussian variation, the ‘‘coarse tune’’ of the particle swarm is obtained through the Cauchy mutation at first, and then its ‘‘fine tune’’ is obtained through the Gaussian mutation. The mutation formula is described as

$$z_k^* = z_k + \beta^{(g-1)} \times r, \quad (9)$$

where z_k and z_k^* represent the value of the k th design variable before and after mutation, respectively; r is a random number; β is the contraction coefficient and $\beta = 0.1$; and g is the number of mutations.

The design variable value can hardly exceed its interval after mutation because of its range limitation in optimization process. The design variable value will be mutated again when its value is not in the definition domain after mutation until its solution is convergence. The maximum number of mutations is stipulated as q when the mutation value still does not satisfy the value range in the procedure. Then, the mutation can be judged according to the absolute value of the difference between the mutation value and interval endpoint value, namely, the mutation value is the left endpoint value and vice versa if the variation value is close to the left endpoint.

2.2.4. Algorithm Principle. Generally, the optimization model is described as

$$\begin{aligned} \min \quad & f(x) \\ \text{s.t.} \quad & g_i(x) \leq 0, \quad i = 1, 2, \dots, N \\ & h_j(x) = 0, \quad j = 1, 2, \dots, M, \\ & x_k \in [x_{k\min}, x_{k\max}], \quad k = 1, 2, \dots, n \end{aligned} \quad (10)$$

where $f(\cdot)$ is the objective function; $g(\cdot)$ is the inequality constraint function; and $h(\cdot)$ is the equality constraint function.

To divide the particle swarm space into the feasible domain and unfeasible domain, a constraint conflict function Vio (x) is constructed, which is defined as

$$\text{Vio}(x) = \sum_{i=1}^N \max[g_i(x), 0] + \sum_{j=1}^M |h_j(x)|. \quad (11)$$

According to equation (11), an arbitrary feasible point satisfies $\text{Vio}(x) = 0$, and an arbitrary unfeasible point satisfies $\text{Vio}(x) > 0$; meanwhile, $\text{Vio}(x)$ can also describe the degree of constraint violation of the unfeasible point.

To control the size of the extended domain and particle speed, the control variable ξ is defined in the following four situations for any two given search points x_1 and x_2 :

- (1) x_1 is superior to x_2 when x_1 and x_2 are both in the extended domain, i.e., $\text{Vio}(\mathbf{x}_1) < \xi$, $\text{Vio}(\mathbf{x}_2) < \xi$ and $f(\mathbf{x}_1) < f(\mathbf{x}_2)$
- (2) x_1 is superior to x_2 when $\text{Vio}(\mathbf{x}_1) = \text{Vio}(\mathbf{x}_2)$ and $f(\mathbf{x}_1) < f(\mathbf{x}_2)$
- (3) x_1 is superior to x_2 when x_1 and x_2 are both outside the extended domain, i.e., $\text{Vio}(\mathbf{x}_1) > \xi$, $\text{Vio}(\mathbf{x}_2) > \xi$ and $\text{Vio}(\mathbf{x}_1) < \text{Vio}(\mathbf{x}_2)$
- (4) x_1 is superior to x_2 when x_1 is in the extended domain, $\text{Vio}(\mathbf{x}_1) < \xi$, and x_2 is outside the extended domain, $\text{Vio}(\mathbf{x}_2) > \xi$

The control variable ξ of the extended domain is gradually changing with particle swarm evolution, and the strategy is expressed as

$$\xi(k) = \xi(0) \times \exp(-\beta \times k), \quad (12)$$

where k is particle swarm evolution algebra and $\xi(0)$ is the initial control variable of the extended domain, which is defined as

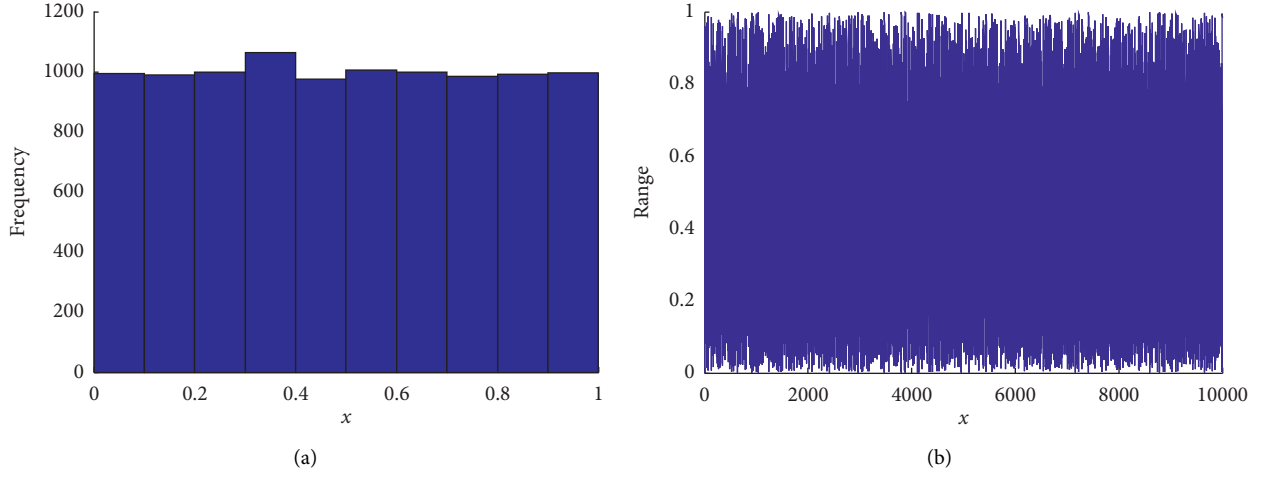


FIGURE 5: Uniform logistic chaotic sequence: (a) frequency curve; (b) ergodic graph.

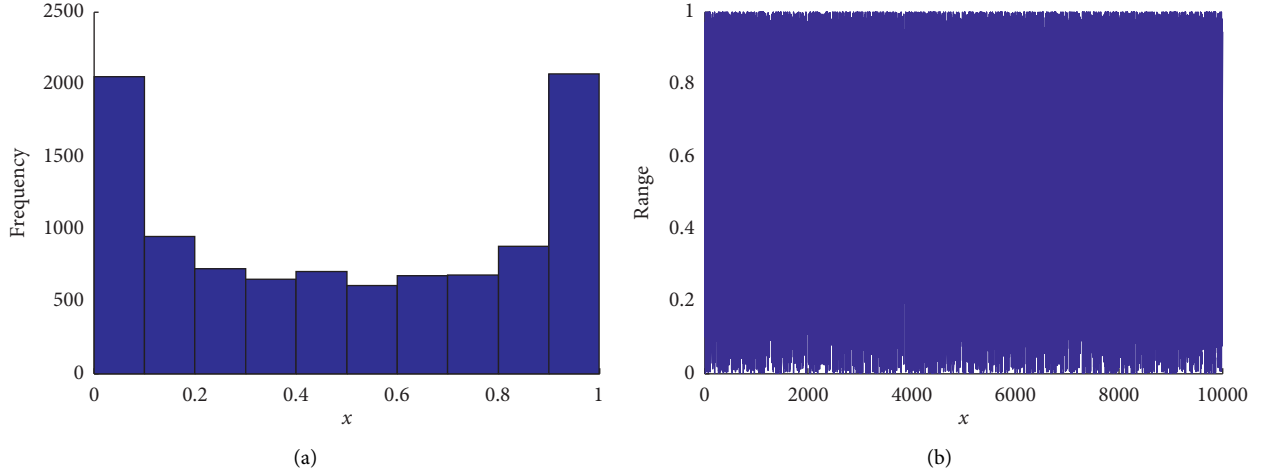


FIGURE 6: Original logistic chaotic sequence: (a) frequency curve; (b) ergodic graph.

$$\xi(0) = \frac{1}{2} \left(\frac{1}{N} \sum_{i=1}^N \text{Vio}(x_i) + \min_{x \in \{x_0\}} \text{Vio}(x) \right), \quad (13)$$

where $\{x_0\}$ is the set composed by the initial particle swarm.

When $\{x_0\}$ evolves to the k th generation, stipulating $\xi(K) = \xi_K$, β can be expressed as

$$\beta = \frac{\log(\xi_0/\xi_K)}{K}. \quad (14)$$

The control variable ξ can be expressed as

$$\xi(k) = \begin{cases} \xi(0) \times \exp(-\beta \times k), & 1 \leq k \leq K, \\ 0, & K \leq k \leq k_{\max}. \end{cases} \quad (15)$$

To make the particle swarm fast gather to the optimal point in the direction, its update strategy is written as

$$\begin{aligned} v_{ij}(k+1) &= w(k) \times |\hat{x}_j(k) - x_{ij}(k)| \times \text{sgn}(v_{ij}) + r \\ &\quad \times [p_{ij}(k) - x_{ij}(k)] + (1-r) \\ &\quad \times [p_{gj}(k) - x_{ij}(k)], \end{aligned} \quad (16)$$

$$x_{ij}(k+1) = x_{ij}(k) + v_{ij}(k+1),$$

where \hat{x} is the optimal position of particles in the current generation; $|\hat{x}_j(k) - x_{ij}(k)|$ controls step length; and $\text{sgn}(v_{ij})$ determines the motion direction of the particle.

The following limit policy is adopted when the particle swarm crosses the border in the process of updating, which is denoted as

$$\begin{aligned} x_{ij}(k) &= \bar{x}_j(k) + r \times [x_{j\min} - \bar{x}_j(k)], & x_{ij}(k) < x_{j\min}, \\ x_{ij}(k) &= \bar{x}_j(k) + r \times [x_{j\max} - \bar{x}_j(k)], & x_{ij}(k) > x_{j\max}, \end{aligned} \quad (17)$$

where r is the uniform-distributed random number and \bar{x} is the locational average of the particle swarm.

To include points such as D in Figure 1(b), the EDM expands the original feasible region and provides preferable information, which is more reasonable.

3. Example

3.1. Unconstrained Optimization. Four test functions are investigated to verify the effectiveness of chaotic methodology. The comparison of PSO, CPSO, and IPSO-EDM is shown in Tables 1–4. Firstly, the mathematic models are established as follows.

(1) Sphere function:

$$f_1(\mathbf{x}) = \sum_{i=1}^n x_i^2, \quad x_i \in [-100, 100]. \quad (18)$$

(2) Rastrigin function:

$$f_2(\mathbf{x}) = \sum_{i=1}^n [x_i^2 - 10 \cos(2\pi x_i) + 10], \quad x_i \in [-5.12, 5.12]. \quad (19)$$

(3) Rosenbrock function:

$$f_3(\mathbf{x}) = \sum_{i=1}^n (100(x_{i+1} - x_i^2)^2 + (x_i - 1)^2), \quad x_i \in [-30, 30]. \quad (20)$$

(4) Ackley function:

$$f_4(\mathbf{x}) = -20 \exp \left(-0.2 \sqrt{\frac{1}{n} \sum_{i=1}^n x_i^2} - \exp \left(\frac{1}{n} \sum_{i=1}^n \cos(2\pi x_i) \right) \right) + 20 + e, \quad x_i \in [-32.768, 32.768]. \quad (21)$$

It is seen from Tables 1–4 that four test functions are used to verify the effectiveness of the IPSO-EDM. As seen in Tables 1–4, the worst value, average value, optimal value, and standard variance in the same dimension are, respectively, calculated via PSO, CPSO, and IPSO-EDM, and the results calculated by the IPSO-EDM are the minimum values. Thus, the computational accuracy of the IPSO-EDM is the highest. In short, the IPSO-EDM has optimal computational accuracy compared with PSO and CPSO.

3.2. Constrained Optimization

3.2.1. Numerical Case Studies. To test the effectiveness of the IPSO-EDM, 3 test case studies are investigated, the scale of the particle swarm is 50, the number of iterations is 1000 times, and $\xi_K = 1e - 15, K = 900$. The statistical results of the optimal function and constraint conflict function are listed in Tables 5 and 6. The comparison of different methods is shown in Tables 7–10, where “N/A” means not available. Firstly, the mathematic models are established as follows.

G1:

$$\begin{aligned} \min \quad & f(\mathbf{x}) = 5 \sum_{i=1}^4 x_i - 5 \sum_{i=1}^4 x_i^2 - \sum_{i=5}^{13} x_i \\ \text{s.t.} \quad & g_1(\mathbf{x}) = 2x_1 + 2x_2 + x_{10} + x_{11} - 10 \leq 0 \\ & g_2(\mathbf{x}) = 2x_1 + 2x_3 + x_{10} + x_{12} - 10 \leq 0 \\ & g_3(\mathbf{x}) = 2x_2 + 2x_3 + x_{11} + x_{12} - 10 \leq 0 \\ & g_4(\mathbf{x}) = -8x_1 + x_{10} \leq 0 \\ & g_5(\mathbf{x}) = -8x_2 + x_{11} \leq 0 \\ & g_6(\mathbf{x}) = -8x_3 + x_{12} \leq 0 \\ & g_7(\mathbf{x}) = -2x_4 - x_5 + x_{10} \leq 0 \\ & g_8(\mathbf{x}) = -2x_6 - x_7 + x_{11} \leq 0 \\ & g_9(\mathbf{x}) = -2x_8 - x_9 + x_{12} \leq 0, \end{aligned} \quad (22)$$

where $0 \leq x_i \leq 1 (i = 1, 2, \dots, 9, 13)$
and $0 \leq x_i \leq 100 (i = 10, 11, 12)$.

G2:

$$\begin{aligned} \min \quad & f(\mathbf{x}) = 5.3578547x_3^2 + 0.8356891x_1x_5 + 37.293239x_1 - 40792.141 \\ \text{s.t.} \quad & g_1(\mathbf{x}) = 85.334407 + 0.0056858x_2x_5 + 0.0006262x_1x_4 - 0.0022053x_3x_5 - 92 \leq 0 \\ & g_2(\mathbf{x}) = -85.334407 - 0.0056858x_2x_5 - 0.0006262x_1x_4 + 0.0022053x_3x_5 \leq 0 \\ & g_3(\mathbf{x}) = 80.51249 + 0.0071317x_2x_5 + 0.0029955x_1x_2 + 0.0021813x_3^2 - 110 \leq 0 \\ & g_4(\mathbf{x}) = -80.51249 - 0.0071317x_2x_5 - 0.0029955x_1x_2 - 0.0021813x_3^2 + 90 \leq 0 \\ & g_5(\mathbf{x}) = 9.300961 + 0.0047026x_3x_5 + 0.0012547x_1x_3 + 0.0019085x_3x_4 - 25 \leq 0 \\ & g_6(\mathbf{x}) = -9.300961 - 0.0047026x_3x_5 - 0.0012547x_1x_3 - 0.0019085x_3x_4 + 20 \leq 0, \end{aligned} \quad (23)$$

TABLE 1: Experimental result of the Sphere function.

f_1	PSO		CPSO		IPSO-EDM	
	$n = 10$	$n = 20$	$n = 10$	$n = 20$	$n = 10$	$n = 20$
Dimensionality						
Worst value	$4.4369e - 49$	$7.4023e - 20$	$3.0672e - 48$	$6.0385e - 22$	$3.3696e - 70$	$9.4993e - 39$
Mean value	$6.5256e - 50$	$6.2447e - 21$	$1.5934e - 49$	$7.9355e - 23$	$1.7190e - 71$	$7.0559e - 40$
Optimal value	$1.1728e - 53$	$1.5012e - 24$	$1.5102e - 54$	$2.1277e - 27$	0	0
Standard variance	$1.1743e - 49$	$1.6707e - 20$	$6.8481e - 49$	$1.5866e - 22$	$7.5283e - 71$	$2.2945e - 39$

TABLE 2: Experimental result of the Rastrigin function.

f_2	PSO		CPSO		IPSO-EDM	
	$n = 10$	$n = 20$	$n = 10$	$n = 20$	$n = 10$	$n = 20$
Dimensionality						
Worst value	5.9697	27.8588	0	$1.8847e - 10$	0	0
Mean value	3.0346	16.2676	0	$9.4753e - 12$	0	0
Optimal value	0	6.9647	0	0	0	0
Standard variance	1.5304	5.3168	0	$4.2132e - 11$	0	0

TABLE 3: Experimental result of the Rosenbrock function.

f_3	PSO		CPSO		IPSO-EDM	
	$n = 10$	$n = 20$	$n = 10$	$n = 20$	$n = 10$	$n = 20$
Dimensionality						
Worst value	22.1917	3.0299e3	12.2003	76.5662	2.9913	4.9399
Mean value	4.3672	174.9661	2.4949	20.5855	0.2530	0.2822
Optimal value	0.0976	4.7483	0.0014	0.1926	$9.9854e - 4$	$9.9068e - 4$
Standard variance	4.6971	672.3508	2.7330	26.6168	0.6919	1.0986

where

$$78 \leq x_1 \leq 102, 33 \leq x_2 \leq 45, \text{ and } 27 \leq x_i \leq 45 (i = 3, 4, 5).$$

G3:

$$\begin{aligned}
 \min \quad & f(\mathbf{x}) = 3x_1 + 0.000001x_1^3 + 2x_2 + \left(\frac{0.000002}{3}\right)x_2^3 \\
 \text{s.t.} \quad & g_1(\mathbf{x}) = -x_4 + x_3 - 0.55 \leq 0 \\
 & g_2(\mathbf{x}) = -x_3 + x_4 - 0.55 \leq 0 \\
 & h_3(\mathbf{x}) = 1000 \sin(-x_3 - 0.25) + 1000 \sin(-x_4 - 0.25) + 894.8 - x_1 = 0 \\
 & h_4(\mathbf{x}) = 1000 \sin(x_3 - 0.25) + 1000 \sin(x_3 - x_4 - 0.25) + 894.8 - x_2 = 0 \\
 & h_5(\mathbf{x}) = 1000 \sin(x_4 - 0.25) + 1000 \sin(x_4 - x_3 - 0.25) + 1294.8 = 0,
 \end{aligned} \tag{24}$$

where $0 \leq x_1 \leq 1200, 0 \leq x_2 \leq 1200, -0.55 \leq x_3 \leq 0.55, \text{ and } -0.55 \leq x_4 \leq 0.55.$

Three numerical case studies are used to verify the effectiveness of the proposed IPSO-EDM. As seen in

Tables 7–10, the worst value, average value, and the best value are, respectively, calculated via the IPSO-EDM and five famous methods, i.e., HM, ASCHEA, SR, EDPSO, and MPSO. The investigation indicates that the computational accuracy of the IPSO-EDM is comparable to HM, ASCHEA,

TABLE 4: Experimental result of the Ackley function.

f_4	PSO		CPSO		IPSO-EDM	
	$n=10$	$n=20$	$n=10$	$n=20$	$n=10$	$n=20$
Dimensionality	$n=10$	$n=20$	$n=10$	$n=20$	$n=10$	$n=20$
Worst value	$2.6645e-15$	$1.0484e-10$	$2.6645e-15$	$1.0991e-11$	$6.2172e-15$	$1.3323e-14$
Mean value	$2.6645e-15$	$3.9470e-11$	$2.6645e-15$	$1.8865e-12$	$2.8422e-15$	$7.1054e-15$
Optimal value	$2.6645e-15$	$1.1324e-12$	$2.6645e-15$	$1.0925e-13$	$2.6645e-15$	$2.6645e-15$
Standard variance	0	$3.6101e-11$	0	$3.0165e-12$	$7.9441e-16$	$2.7938e-15$

Note. The scale of the particle swarm is 50, the change interval of inertia factor $\omega \in [0.4, 0.9]$, earning factors $c_1 = c_2 = 2$, the number of iterations is 2000 times, the number of chaotic iterations is 1000 times, and the maximum number of evolutionary variations allowed is 1000 times.

SR, EDPSO, and MPSO. Furthermore, this research manifests that the computational efficiency of the IPSO-EDM is significantly improved compared with the other five methods (HM, ASCHEA, SR, EDPSO, and MPSO) by measuring the product of the group size and algorithm cycle times. It can be seen from Table 10 that the computational efficiency of the IPSO-EDM is the largest compared with the other five methods, i.e., the product of population size and algorithm cycle times of the IPSO-EDM is the least among all methods.

To verify the effectiveness of the presented algorithm, the new parameters such as β and $Vio(x)$ are investigated. The performance function is written as

$$\mathbf{g}(\mathbf{X}_1, \mathbf{X}_2) = \mathbf{X}_1^3 + \mathbf{X}_2^3 - 18, \quad (25)$$

where $\mathbf{X}_1 \sim N(10, 5^2)$ and $\mathbf{X}_2 \sim N(9.9, 5^2)$.

The iteration process of β and $Vio(x)$ is calculated by HL, W-G, and IPSO-EDM, which are shown in Figure 7.

Figure 7 indicates that $Vio(x)$ of the standard HL method is very large, and its convergence value is 674.2829, but convergence values of W-G and IPSO-EDM are, respectively, $2.42e-2$ and $5.14e-4$, which manifests feasible points of HL are very few, i.e., the accuracy is very low. Meanwhile, it can be seen that the curve of $Vio(x)$ obtained is fairly close each other by W-G and IPSO-EDM, but the convergence value obtained via the IPSO-EDM is $5.14e-4$ which is smaller than $2.42e-2$ obtained by W-G, and this means the accuracy of IPSO-EDM is higher than that of W-G. Meanwhile, the convergence value of β via HL is 1.1657, and they are 2.22572 and 2.22599 by W-G and IPSO-EDM. Thus, the computational accuracy and efficiency of the IPSO-EDM are optimal and of HL are the worst.

3.2.2. Engineering Case Study. Many researchers use the finite element method to study engineering [38], but they do not optimize it. This method can also be used in practical engineering, for instance, this is a welded beam structure, which is shown in Figure 8.

The optimization goal is to seek four design variables, i.e., $x_1(h)$, $x_2(l)$, $x_3(t)$, and $x_4(b)$, which satisfy the constraints of shear stress τ , bending stress σ , bending load P_c of the welding rod, deviation δ , and the boundary condition, and the total manufacturing cost of the welding rod is the minimum. The mathematical model is described as

$$\begin{aligned} \min \quad & f(\mathbf{x}) = 1.104712x_1^2x_2 + 0.04811x_3x_4(14 + x_2) \\ \text{s.t.} \quad & g_1(\mathbf{x}) = \tau(\mathbf{x}) - 13600 \leq 0 \\ & g_2(\mathbf{x}) = \sigma(\mathbf{x}) - 30000 \leq 0 \\ & g_3(\mathbf{x}) = x_1 - x_4 \leq 0 \\ & g_4(\mathbf{x}) = 0.10471x_1^2 + 0.04811x_3x_4(14 + x_2) - 5 \leq 0 \\ & g_5(\mathbf{x}) = 0.125 - x_1 \leq 0 \\ & g_6(\mathbf{x}) = \delta(\mathbf{x}) - 0.25 \leq 0 \\ & g_7(\mathbf{x}) = P - P_c(\mathbf{x}) \leq 0, \end{aligned} \quad (26)$$

where

$$\begin{aligned} \tau(\mathbf{x}) &= \sqrt{(\tau')^2 + 2\tau'\tau''\frac{x_2}{2R} + (\tau'')^2}, \\ \tau'(\mathbf{x}) &= \frac{P}{\sqrt{2}x_1x_2}, \\ \tau'' &= \frac{QR}{J}, \\ Q(\mathbf{x}) &= P\left(L + \frac{x_2}{2}\right), \\ R(\mathbf{x}) &= \sqrt{\frac{x_2^2}{4} + \left(\frac{x_1 + x_2}{2}\right)^2}, \\ J(\mathbf{x}) &= 2\left\{\sqrt{2}x_1x_2\left[\frac{x_2^2}{12} + \left(\frac{x_1 + x_3}{2}\right)^2\right]\right\}, \\ \sigma(\mathbf{x}) &= \frac{6PL}{x_4x_3^2}, \\ \delta(\mathbf{x}) &= \frac{4PL^3}{Ex_3^3x_4}, \\ P_c(\mathbf{x}) &= \frac{4.013E\sqrt{x_3^2x_4^6/36}}{L^2}\left(1 - \frac{x_3}{2L}\sqrt{\frac{E}{4G}}\right). \end{aligned} \quad (27)$$

Note that $P = 6000$, $L = 14$, $E = 30 \times 10^6$, $G = 12 \times 10^6$, $0.1 \leq x_1 \leq 2$, $0.1 \leq x_2 \leq 10$, $0.1 \leq x_3 \leq 10$, and $0.1 \leq x_4 \leq 2$.

The comparison results obtained by the IPSO-EDM and the other methods are shown in Table 11.

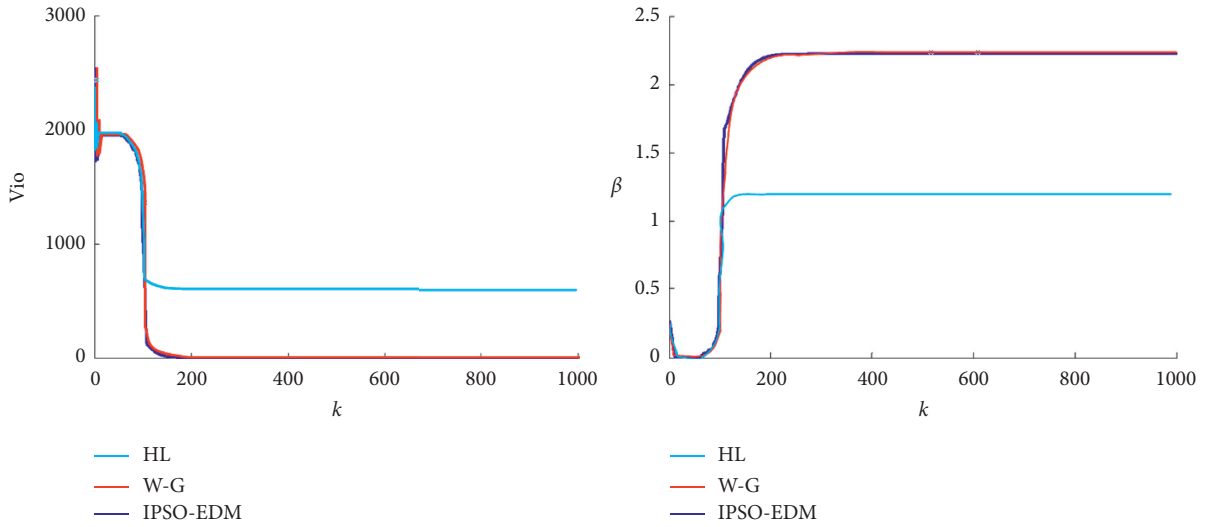


FIGURE 7: Iteration process of β and $V_{io}(x)$.

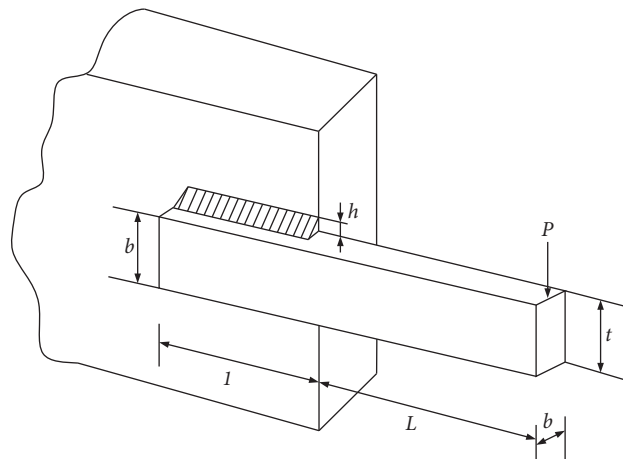


FIGURE 8: Welded beam schematic diagram.

TABLE 5: Statistics of the optimal value with the IPSO-EDM.

Test examples	Optimal value	Mean value	Worst value	Standard variance
G1	-15	-15	-15	$1.8724e-15$
G2	$-3.066e4$	$-3.066e4$	$-3.066e4$	0.0019
G3	$5.1265e3$	$5.1482e3$	$5.1871e3$	20.3178

TABLE 6: Statistics of the constraint conflict function with the IPSO-EDM.

Test examples	Optimal value	Mean value	Worst value	Standard variance
G1	0	$4.8850e-16$	$2.6645e-15$	$1.0352e-15$
G2	0	$1.7764e-15$	$1.4211e-14$	$4.5094e-15$
G3	0	$8.8510e-4$	0.0061	0.0020

TABLE 7: Comparison of the optimal results obtained by different methods.

Test examples	HM [35]	ASCHEA [36]	SR [37]	IPSO-EDM	EDPSO [21]	MPSO [25]
G1	-14.7886	-15.0000	-15.0000	-15.0000	-15.0000	-14.9863
G2	-30665.5	-30665.5	-30665.5	-30665.5	-30665.5	-30665.5
G3	N/A	5126.5	5126.4	5126.5	5126.5	5126.5

TABLE 8: Comparison of average results obtained by different methods.

Test examples	HM [35]	ASCHEA [36]	SR [37]	IPSO-EDM	EDPSO [21]	MPSO [25]
G1	-14.7082	-14.8400	-15.0000	-15.0000	-15.0000	-14.9986
G2	-30665.3	-30665.5	-30665.5	-30665.5	-30665.5	-30665.5
G3	N/A	5141.7	5128.9	5148.2	5148.1	5149.7

TABLE 9: Comparison of the worst results obtained by different methods.

Test examples	HM [35]	ASCHEA [36]	SR [37]	IPSO-EDM	EDPSO [21]	MPSO [25]
G1	-14.6154	N/A	-15.0000	-15.0000	-15.0000	-14.9992
G2	-30645.9	N/A	-30665.5	-30665.5	-30665.5	-30665.5
G3	N/A	N/A	5142.472	5187.134	5148.1	5146.5

TABLE 10: Comparison of computational efficiency of different methods.

Test examples	HM [35]	ASCHEA [36]	SR [37]	IPSO-EDM	EDPSO [21]	MPSO [25]	η_{IP_H} (%)	η_{IP_A} (%)	η_{IP_S} (%)	η_{IP_E} (%)	η_{IP_M} (%)
G1	1400000	1500000	350000	50000	60000	90000	96.42	96.67	85.71	16.67	44.44
G2	1400000	1500000	350000	50000	60000	90000	96.42	96.67	85.71	16.67	44.44
G3	1400000	1500000	350000	50000	60000	90000	96.42	96.67	85.71	16.67	44.44

Note. η_{IP_H} is the improved computational efficiency by the IPSO-EDM compared with that by HM; η_{IP_A} is the improved computational efficiency of the IPSO-EDM compared with that by ASCHEA; η_{IP_S} is the improved computational efficiency by the IPSO-EDM compared with that by SR; η_{IP_E} is the improved computational efficiency by the IPSO-EDM compared with that by EDPSO; and η_{IP_M} is the improved computational efficiency by the IPSO-EDM compared with that by MPSO.

TABLE 11: Comparison of the calculation results by different methods for the welding beam.

Methods	$x_1 (h)$	$x_2 (l)$	$x_3 (t)$	$x_4 (b)$	$f(x)$
Coello [39]	0.208800	3.420500	8.997500	0.210000	1.748309
Coello and Montes [40]	0.205986	3.471328	9.020224	0.206480	1.728226
Coello and Becerra [41]	0.205700	3.470500	9.036600	0.205700	1.724852
IPSO-EDM	0.205730	3.470489	9.036624	0.205730	1.724852
CPSO [27]	0.205731	3.470582	9.036839	0.205680	1.724237
Methods	Optimal value	Mean value	Worst value	Standard variance	
Coello [39]	1.748309	1.771973	1.785835	0.001122	
Coello and Montes [40]	1.728226	1.792654	1.993408	0.074713	
Coello and Becerra [41]	1.724852	1.971809	3.179709	0.443131	
IPSO-EDM	1.724852	1.738620	1.959606	0.048555	
CPSO [27]	1.724381	1.738810	1.958721	0.047891	

The optimal results obtained by the IPSO-EDM are equivalent to those provided by the existing literature, which verifies the accuracy of this method. However, the computational efficiency of the proposed IPSO-EDM is higher than the methods in the literature in Table 10.

4. Conclusions

The standard PSO algorithm is improved from the perspective of engineering application to solve engineering optimization problems.

- (1) The original feasible region is expanded, and some points that are closer to the constrained optimal point in the feasible region are contained as feasible points, which provide preferable function information compared with the points in the original feasible region. This approach uses the current location information of the particles and particle swarm to determine the speed of the particles. In short, the

difference value in the current optimal positions of the particle swarm and the particle is used to determine the current particle velocity. The optimal location of obtained points using the proposed method is better than that obtained using the standard PSO.

- (2) The constrained optimization is transformed into the unconstrained optimization by combining the ergodicity of chaos optimization and the evolutionary variation to realize global search. The logistic chaotic system equation is applied in the PSO algorithm, and the mutation operator is introduced in the evolutionary variation strategy to escape local optimal and maintain its vitality of the particle swarm, which prevents the particle swarm from falling into the condition of “precocity” at the earlier iteration.
- (3) An unconstrained optimization case study, four numerical case studies, and one engineering case study are used to verify the effectiveness of the

IPSO-EDM. The worst value, average value, and optimal value are, respectively, calculated via the IPSO-EDM and compared with other methods. The investigation indicates that the computational accuracy of the IPSO-EDM is comparable to that provided by the existing literature; however, the computational efficiency of the IPSO-EDM is significantly improved.

- (4) Though the PSO method is improved and six case studies are investigated to prove the effectiveness of this method, yet the numerical case studies are relatively simple, and the design variables of the engineering case study are small. Moreover, only the deterministic optimization is studied. Thus, the nondeterministic optimization will be researched, and the random variable will be subject to normal distribution, exponential distribution, or Weibull distribution. Accordingly, the proposed method can be expanded to wide-spread engineering application fields. Further studies will focus on the IPSO-EDM considering random variables of different distributions including normal distribution, exponential distribution, and Weibull distribution to deal with actual operation of the machines.

Data Availability

The data used to support the findings of this study are currently under embargo, while the research findings are commercialized. Requests for data 6/12 months after publication of this article will be considered by the corresponding author.

Conflicts of Interest

The authors declare that there are no conflicts of interest regarding the publication of this paper.

Acknowledgments

The authors gratefully acknowledge the financial support for this research from the National Key R&D Plan Project (Grant no. 2017YFB1301300), the National Natural Science Foundation of China (Grant nos. 11772011 and 11902220), and the National Natural Science Foundation of Hebei Province (Grant no. E2020202217).

References

- [1] Y. M. Zhang, Z. X. Wen, H. Q. Pei, J. P. Wang, Z. W. Li, and Z. F. Yue, "Equivalent method of evaluating mechanical properties of perforated Ni-based single crystal plates using artificial neural networks," *Computer Methods in Applied Mechanics and Engineering*, vol. 360, Article ID 112725, 2020.
- [2] A. L. Soubhia and A. L. Serpa, "Discrete optimization for positioning of actuators and sensors in vibration control using the simulated annealing method," *Journal of the Brazilian Society of Mechanical Sciences and Engineering*, vol. 42, no. 2, p. 101, 2020.
- [3] H. Zhi and S. Y. Liu, "A hybrid GABC-GA Algorithm for mechanical design optimization problems," *Intelligent Automation and Soft Computing*, vol. 25, no. 4, pp. 815–825, 2019.
- [4] J. Martínez-Morales, H. Quej-Cosgaya, J. Lagunas-Jiménez, E. Palacios-Hernández, and J. Morales-Saldaña, "Design optimization of multilayer perceptron neural network by ant colony optimization applied to engine emissions data," *Science China Technological Sciences*, vol. 62, no. 6, pp. 1055–1064, 2019.
- [5] M. Huang and Z. Liu, "Research on mechanical fault prediction method based on multifeature fusion of vibration sensing data," *Sensors*, vol. 20, no. 1, p. 6, 2020.
- [6] J. P. Janet, L. Chan, and H. J. Kulik, "Accelerating chemical discovery with machine learning: simulated evolution of spin crossover complexes with an artificial neural network," *The Journal of Physical Chemistry Letters*, vol. 9, no. 5, pp. 1064–1071, 2018.
- [7] F. Zhao, S. Qin, Y. Zhang, W. Ma, C. Zhang, and H. Song, "A two-stage differential biogeography-based optimization algorithm and its performance analysis," *Expert Systems with Applications*, vol. 115, pp. 329–345, 2019.
- [8] E. Pena, S. M. Zhang, R. Patriat et al., "Multi-objective particle swarm optimization for postoperative deep brain stimulation targeting of subthalamic nucleus pathways," *Journal of Neural Engineering*, vol. 15, no. 6, Article ID 066020, 2018.
- [9] E. Camci, D. R. Kripalani, L. L. Ma, E. Kayacan, and M. A. Khanesar, "An aerial robot for rice farm quality inspection with type-2 fuzzy neural networks tuned by particle swarm optimization-sliding mode control hybrid algorithm," *Swarm and Evolutionary Computation*, vol. 41, pp. 1–8, 2018.
- [10] J.-Y. Jhang, C.-J. Lin, C.-T. Lin, and K.-Y. Young, "Navigation control of mobile robots using an interval type-2 fuzzy controller based on dynamic-group particle swarm optimization," *International Journal of Control, Automation and Systems*, vol. 16, no. 5, pp. 2446–2457, 2018.
- [11] W. Tao, Z. Liu, P. Zhu, C. Zhu, and W. Chen, "Multi-scale design of three dimensional woven composite automobile fender using modified particle swarm optimization algorithm," *Composite Structures*, vol. 181, pp. 73–83, 2017.
- [12] A. ElSaid, F. El Jamiy, J. Higgins, B. Wild, and T. Desell, "Optimizing long short-term memory recurrent neural networks using ant colony optimization to predict turbine engine vibration," *Applied Soft Computing*, vol. 73, pp. 969–991, 2018.
- [13] Z. Cao, H. Guo, J. Zhang, D. Niyato, and U. Fastenrath, "Improving the efficiency of stochastic vehicle routing: a partial Lagrange multiplier method," *IEEE Transactions on Vehicular Technology*, vol. 65, no. 6, pp. 3993–4005, 2016.
- [14] J.-G. Ahn, H.-I. Yang, and J.-G. Kim, "Multipoint constraints with Lagrange multiplier for system dynamics and its reduced-order modeling," *AIAA Journal*, vol. 58, no. 1, pp. 385–401, 2020.
- [15] J. Liang, L. Dai, S. Chen et al., "Generalized inverse matrix-exterior penalty function (GIM-EPP) algorithm for data processing of multi-wavelength pyrometer (MWP)," *Optics Express*, vol. 26, no. 20, pp. 25706–25720, 2018.
- [16] J. Kennedy and R. C. Eberhart, "Particle swarm optimization," in *Proceedings of the 1995 IEEE International Conference on Neural Networks*, pp. 1942–1948, Perth, Australia, 1995.
- [17] Z. Xue, H. Li, Y. Zhou, N. Ren, and W. Wen, "Analytical prediction and optimization of cogging torque in surface-mounted permanent magnet machines with modified particle swarm optimization," *IEEE Transactions on Industrial Electronics*, vol. 64, no. 12, pp. 9795–9805, 2017.
- [18] H. Han, X. Wu, L. Zhang, Y. Tian, and J. Qiao, "Self-organizing RBF neural network using an adaptive gradient

- multiobjective particle swarm optimization," *IEEE Transactions on Cybernetics*, vol. 49, no. 1, pp. 69–82, 2019.
- [19] J. Yi, X. Li, C.-H. Chu, and L. Gao, "Parallel chaotic local search enhanced harmony search algorithm for engineering design optimization," *Journal of Intelligent Manufacturing*, vol. 30, no. 1, pp. 405–428, 2019.
- [20] J. B. Park, Y. W. Jeong, J. R. Shin, and K. Y. Lee, "An improved particle swarm optimization for nonconvex economic dispatch problems," *IEEE Transactions on Power Systems*, vol. 25, no. 1, pp. 156–166, 2010.
- [21] M. D. Phung, C. H. Quach, T. H. Dinh, and Q. Ha, "Enhanced discrete particle swarm optimization path planning for UAV vision-based surface inspection," *Automation in Construction*, vol. 81, pp. 25–33, 2017.
- [22] R. Wang and X. Zhang, "Optimal design of a planar parallel 3-DOF nanopositioner with multi-objective," *Mechanism and Machine Theory*, vol. 112, pp. 61–83, 2017.
- [23] A. Nickabadi, M. M. Ebadzadeh, and R. Safabakhsh, "A novel particle swarm optimization algorithm with adaptive inertia weight," *Applied Soft Computing*, vol. 11, no. 4, pp. 3658–3670, 2011.
- [24] H. D. Mojarrad and M. Nayeripour, "A new fuzzy adaptive particle swarm optimization for non-smooth economic dispatch," *Energy*, vol. 35, no. 4, pp. 1764–1778, 2010.
- [25] S. Khan, M. Kamran, and O. U. Rehman, "A modified PSO algorithm with dynamic parameters for solving complex engineering design problem," *International Journal of Computer Mathematics*, vol. 95, no. 11, pp. 2308–2329, 2018.
- [26] H. B. Liang, D. L. Zou, Z. L. Li, M. J. Khan, and Y. J. Lu, "Dynamic evaluation of drilling leakage risk based on fuzzy theory and PSO-SVR algorithm," *Future Generation Computer Systems*, vol. 95, pp. 454–466, 2019.
- [27] D. P. Tian, X. F. Zhao, and Z. Z. Shi, "Chaotic particle swarm optimization with sigmoid-based acceleration coefficients for numerical function optimization," *Swarm and Evolutionary Computation*, vol. 51, Article ID 100573, 2019.
- [28] F. S. Hsieh, F. M. Zhan, and Y. H. Guo, "A solution methodology for carpooling systems based on double auctions and cooperative coevolutionary particle swarms," *Applied Intelligence*, vol. 49, no. 2, pp. 741–763, 2019.
- [29] S. K. S. Fan and E. Zahara, "A hybrid simplex search and particle swarm optimization for unconstrained optimization," *European Journal of Operational Research*, vol. 181, no. 2, pp. 527–548, 2007.
- [30] E. Zahara and C.-H. Hu, "Solving constrained optimization problems with hybrid particle swarm optimization," *Engineering Optimization*, vol. 40, no. 11, pp. 1031–1049, 2008.
- [31] X. F. Liu, Z. H. Zhan, Y. Gao, J. Zhang, S. Kwong, and J. Zhang, "Coevolutionary particle swarm optimization with bottleneck objective learning strategy for many-objective optimization," *IEEE Transactions on Evolutionary Computation*, vol. 23, no. 4, pp. 587–602, 2019.
- [32] X. W. Xia, L. Gui, F. Yu et al., "Triple archives particle swarm optimization," *IEEE Transactions on Cybernetics*, pp. 1–14, 2019.
- [33] Z.-J. Wang, Z.-H. Zhan, S. Kwong, H. Jin, and J. Zhang, "Adaptive granularity learning distributed particle swarm optimization for large-scale optimization," *IEEE Transactions on Cybernetics*, pp. 1–14, 2020.
- [34] A. Hinrichs, F. Pillichshammer, and S. Tezuka, "Tractability properties of the weighted star discrepancy of the Halton sequence," *Journal of Computational and Applied Mathematics*, vol. 350, pp. 46–54, 2019.
- [35] S. Koziel and Z. Michalewicz, "Evolutionary algorithms, homomorphous mappings, and constrained parameter optimization," *Evolutionary Computation*, vol. 7, no. 1, pp. 19–44, 1999.
- [36] S. B. Hamida and M. Schoenauer, "ASCHEA: new results using adaptive segregational constraint handling," in *Proceedings of the 2002 Congress on Evolutionary Computation*, IEEE, Piscataway, NJ, USA, pp. 884–889, May 2002.
- [37] T. P. Runarsson and X. Yao, "Stochastic ranking for constrained evolutionary optimization," *IEEE Transactions on Evolutionary Computation*, vol. 4, no. 3, pp. 284–294, 2000.
- [38] B. Bai, H. Li, W. Zhang, and Y. C. Cui, "Application of extremum response surface method-based improved substructure component modal synthesis in mistuned turbine bladed disk," *Journal of Sound and Vibration*, vol. 472, Article ID 115210, 2020.
- [39] C. A. C. Coello, "Use of a self-adaptive penalty approach for engineering optimization problems," *Computers in Industry*, vol. 41, no. 1, pp. 113–127, 2000.
- [40] C. A. C. Coello and E. M. Montes, "Constraint-handling in genetic algorithms through the use of dominance-based tournament selection," *Advanced Engineering Informatics*, vol. 16, no. 1, pp. 193–203, 2002.
- [41] C. A. C. Coello and R. L. Becerra, "Efficient evolutionary optimization through the use of a cultural algorithm," *Engineering Optimization*, vol. 36, no. 2, pp. 219–236, 2004.

Review Article

Restoration Methods of Respiratory Function for Spinal Cord Injury

X. Y. Gu ¹, S. Ren ^{2,3}, Y. Shi ², N. Wang ⁴, Z. H. Tong ⁵ and M. L. Cai²

¹The School of Biology and Medical Engineering, Beihang University, Beijing 100191, China

²The School of Automation Science and Electrical Engineering, Beihang University, Beijing 100191, China

³The State Key Laboratory of Fluid Power and Mechatronic Systems, Zhejiang University, Hangzhou 310027, China

⁴The Engineering Training Center, Beihang University, Beijing 100191, China

⁵The Department of Respiratory Medicine, Beijing Chaoyang Hospital, Beijing 100020, China

Correspondence should be addressed to S. Ren; renshuai@buaa.edu.cn and Y. Shi; shiyang@buaa.edu.cn

Received 29 May 2020; Revised 27 June 2020; Accepted 8 July 2020; Published 29 July 2020

Guest Editor: Hang Su

Copyright © 2020 X. Y. Gu et al. This is an open access article distributed under the Creative Commons Attribution License, which permits unrestricted use, distribution, and reproduction in any medium, provided the original work is properly cited.

Respiratory dysfunction caused by high spinal cord injury is fatal damage. Three treatment methods commonly used in the clinic, diaphragm pacing, mechanical ventilation, and respiratory muscle training, were chosen to explain the respiratory function reconstruction of spinal cord injury. The characteristics, research status, advantages, and disadvantages of these three treatment methods are reviewed. Diaphragm pacing technology has attracted much attention due to its price-friendly, efficient, and closer to physiological respiration. Therefore, the emphasis is on describing the characteristics of the stimulation waveform of diaphragm pacing and the mathematical correspondence between stimulation parameters (pulse interval, inspiratory time, etc.) and tidal volume. Meanwhile, it also briefly introduces that for patients with SCI with poor diaphragm pacing, intercostal muscle pacing can be used as the second option to restore respiratory function. Also, the development of electronic technology has promoted the emergence of closed-loop diaphragm pacing technology. Finally, we propose that the method of respiratory function reconstruction after spinal cord injury should pay more attention to physiology and the safety of surgery.

1. Introduction

Recently, with the advance of transportation and construction industry, the number of spinal cord injury (SCI) patients caused by traffic accidents and falls has been increasing year by year. According to the survey, the global incidence of traumatic spinal cord injury (TSCI) is almost 10.5/100,000 [1]. SCI in China has exceeded 100,000 cases in 2012 and increases by 10,000 to 60,000 cases each year [2]. High segment and severe SCI, especially for patients with complete high cervical SCI, will lead to respiratory dysfunction and high mortality [2]. In the critical condition, about 20% of these patients need to be treated with tracheotomy and mechanical ventilation. After treatment, there are still 5% of patients with acute SCI depending on long-term ventilation support with a ventilator to sustain life [3]. It may cause the patients speech difficulties, inconvenience

in social activities, decubitus ulcers, and lung infection, bringing them both psychological and physical pressure [4].

In the past several decades, functional electrical stimulation, using electricity to stimulate the motor nerve to cause muscles contraction, has been successfully used in the recovery of motor function in SCI. Based on this principle, the implantable diaphragmatic pacing can restore spontaneous respiration in high cervical SCI patients [5]. Applying abdominal functional electrical stimulation can increase the tidal volume of respiration in patients with SCI [6]. Furthermore, Electrical stimulation of intercostal nerve roots (T2, 3) produces higher inspiratory capacity [7, 8]. Besides, there are several other ways to reconstruct the respiratory function after SCI, such as the nerve and olfactory cell transplantation [9, 10].

As mentioned previously, the ways to restore the patients' respiratory function with SCI are varied. It is

inappropriate for us to describe all the methods in detail. Hence, we choose three mature clinical treatments with the help of medical devices, including mechanical ventilation, functional electrical stimulation, and respiratory muscle training for analysis. By comparing the effectiveness, advantages, and disadvantages of these three methods to patients' treatment, we focus on the electrical stimulation and briefly describe the clinical application of the other two techniques. Finally, the future development of respiratory function reconstruction methods for SCI is briefly introduced. This review is useful for engineering technicians and medical staff engaged in respiratory therapy. For medical staff, they can quickly understand the key technologies and indications of these treatments to choose the appropriate treatment for the patient. The engineering staff would propose improvements to the technical deficiencies of existing treatment equipment to promote the development of medical devices related to respiratory therapy.

2. Respiratory Mechanism and Spinal Cord Injury

The respiration motion, consisting of inhalation and exhalation, can be seen as the process of gas exchange between the body and the external environment. It is always a self-control and unconscious movement [11], which is controlled by a combination of respiratory muscles, such as the diaphragm, intercostal muscles, and scalenus muscles. The contraction of diaphragm, intercostals, and scalenus muscles in inhalation leads to the decrease in chest pressure. Therefore, the increase of lung volume and the reductions of pressure in lung make the gas from the outside enter the body. During exhalation, the movement of the respiratory muscles and changes of the air pressure in the chest and lungs are contrary to the inhalation process.

In the respiratory muscles, the diaphragm separating the chest and the abdominal cavity is the primary power pump source of ventilation function [12]. The volume of ventilation produced by diaphragm contraction in rest respiration accounts for 60%–80% of the total amount of ventilation [12].

The spinal cord can be seen as the bridge between the brain and the peripheral nerves. Its function is to transmit the motor and sensory information to brain and organs of the body [2]. As shown in Figure 1, the spinal cord in the spine made up of 26 segment vertebrae controls different physiological (sensation and motor) functions of the body [3, 13].

High spinal cord injury (cervical and upper thoracic SCI) is a fatal injury that results in respiratory dysfunction, expectoration weakness, and even without autonomous breathing. That is because high SCI damage the neurons that dominate the contraction of the central respiratory muscles [3]. Figure 2 simply illustrates that the respiratory rhythm arises from the medulla oblongata and its relationship to the spinal cord. The axons of the respiratory neurons project down into the spinal cord, causing the motor neurons of the inspiratory muscles (diaphragms and intercostal muscles) to excite. If the injury occurs above T6, the medullary centre

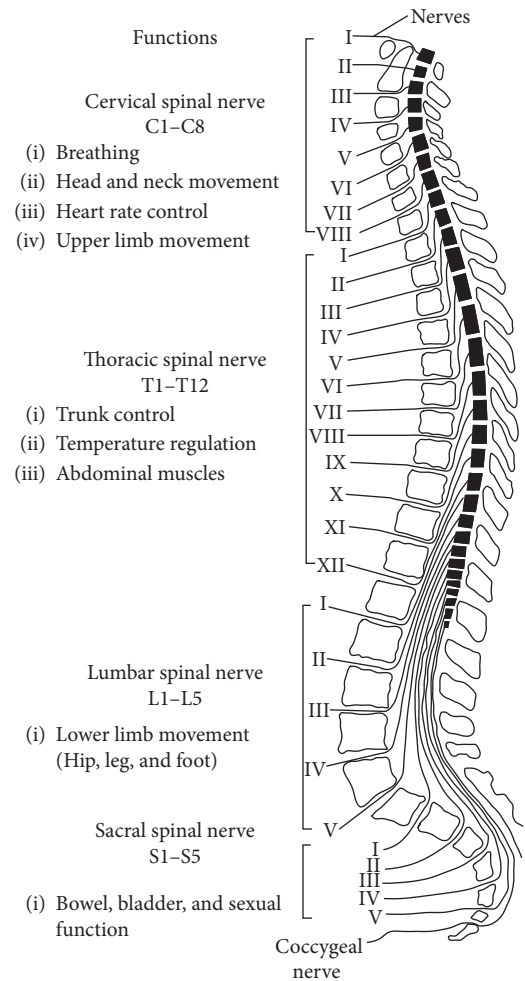


FIGURE 1: The structure of the spine and its corresponding physiological function [13]. The spine is composed of 26 segments of vertebrae, which can be divided into the cervical spine (7), thoracic spine (12), lumbar spine (5), sacroiliac spine, and coccyx. A spinal canal is formed inside the spine from the top to bottom with a spinal cord inside. Spinal cords in different segments control different physiological functions (breathing, movement, defecation function, etc.) of the human body.

and the respiratory muscles will be separated to different degrees, causing respiratory dysfunction. Especially for damages above the C2 level, the medulla oblongata will completely lose regulation of the respiratory muscles.

It is reported that the incidence of respiratory complications, including ventilatory failure and respiratory infection, caused by high SCI can be as high as 81.3% [14, 15]. More significantly, higher (C1–C4) and more severe spinal cord injuries will lead to more severe and long-lasting respiratory complications.

3. Electrical Stimulation Therapy

In recent decades, functional electrical stimulation has achieved a specific clinical effect in the recovery of movement, respiration, urination, and other functions of patients with SCI. It is reported that the diaphragm has been

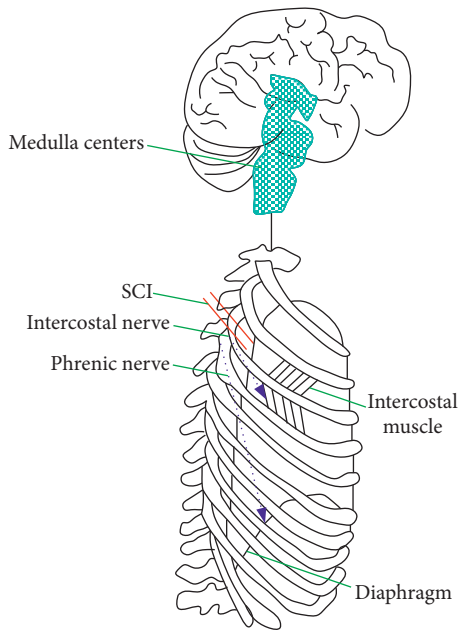


FIGURE 2: The relationship between SCI and respiratory dysfunction. There is a primary centre in the medulla that produces rhythmic breathing. SCI will cause respiratory muscles to escape the control of the medulla centre.

activated by electrical stimulation technology for more than 200 years [16].

3.1. Diaphragm Pacemaker. Diaphragmatic pacing (DP), also known as phrenic nerve stimulation (PNS), is based on the principle of stimulating the phrenic nerve with an electric pulse, thus causing the contraction of the diaphragm to simulate the respiratory movement of the human physiological mode [17]. In the 1960s, the development of electrical stimulation by radio-frequency changed the conventional PNS system. In 1972, Glenn et al. used DP for the first time to improve the respiratory function of patients with high cervical spinal cord injury and achieved success [18].

Moreover, DP technology was proved to be a safe and reliable operation. Glenn being the first doctor to use DP, reported the follow-up results of 77 patients in 1985 [19]. DP was used for up to 10–16 years in these 77 patients. Kong et al. introduced that, in 19 patients who used phrenic stimulation in Australia, the average duration of continuous pacing reached 13 years [20]. There are also many cases that have been used for more than 20 years [21]. At present, DP technology has been recognized in clinical. According to some studies, more than 2000 patients in the world have used DP to recover the SCI that cannot breathe autonomously [22, 23]. These cases fully prove the effectiveness and safety of DP.

Figure 3(a) is the operating principle of diaphragm pacemaker (DP) containing implanted components (electrodes, connector, and radiofrequency receiver) and exterior components (antenna and stimulus transmitter) [24]. Figure 3(b) is a physical diagram of the implantation of

electrodes and receivers for diaphragm pacemaker surgery. The two electrodes connected to the radiofrequency receiver are placed on the phrenic nerves. There is no electric source in vivo, and the external stimulus transmitter based on the principle of electromagnetic induction provides parameter commands (waveform, pulse width, and frequency) and electric energy for the internal device. During stimulation, the power and stimulus parameter instruction is sent to the radiofrequency receiver by the stimulus transmitter. According to the received data, the radiofrequency receiver transmits the electric pulse to the phrenic nerve through the electrode in an alternating manner.

The working process of the DP and the relationship between the various components can be summarised in the flowchart shown in Figure 4. It can be seen more intuitively from the workflow diagram that the DP does not monitor the ventilation effect during the work process, which may be dangerous without the care of medical staff.

Currently, three kinds of DP manufactured by Avery company in the United States, Atrotech company in Finland, and Medimplant company in Australia, respectively, are available in the market [4, 26]. The stimulation effect of them is the same, and the main difference (see Table 1) is the number of the electrode and the electrode implantation. Among the three types of DP, Avery is the first company to develop this product widely used in the world. Compared with the bipolar electrode, the monopolar electrode with more advantages is suitable for most patients. However, for patients with heart pacemaker, to prevent the interference of current, the only bipolar electrode can be selected. Atrotech and Medimplant use quadrupole electrodes to reduce the stimulation frequency and effectively reduce diaphragm fatigue.

3.1.1. Indication of DP. The main indications of DP are sleep apnea syndrome, brain stem injury-induced respiratory failure, and loss of spontaneous respiration due to SCI above C3 [27]. Among these injuries, high SCI is the best indication for DP [28]. However, not all respiratory dysfunction caused by high SCI is suitable for treatment with DP. Whether the structure and function of the phrenic nerve and the phrenic muscle are complete is the fundamental premise for performing DP. Therefore, it is necessary to evaluate it in detail before surgery [29, 30]. The evaluation methods of diaphragm function mainly include the phrenic nerve conduction velocity (7.5–9 ms), the change in transdiaphragm pressure (unilateral pacing: 10 cm H₂O), and the observation of diaphragm activity under fluoroscopy [31–33], which are as shown in Table 2. Fluoroscopy is the most reliable method to observe diaphragm activity among these methods. X-ray fluoroscopy was used to observe the degree of phrenic muscle descent when the phrenic nerve was electrically stimulated. If the descent was more than 5 cm, the success rate of pacing was high.

In addition, the pacing response of unilateral diaphragm may not hinder the implementation of diaphragm pacing. On the contrary, unilateral diaphragm pacing can achieve good pacing effect [30, 34]. Oldenburg O. verified that the

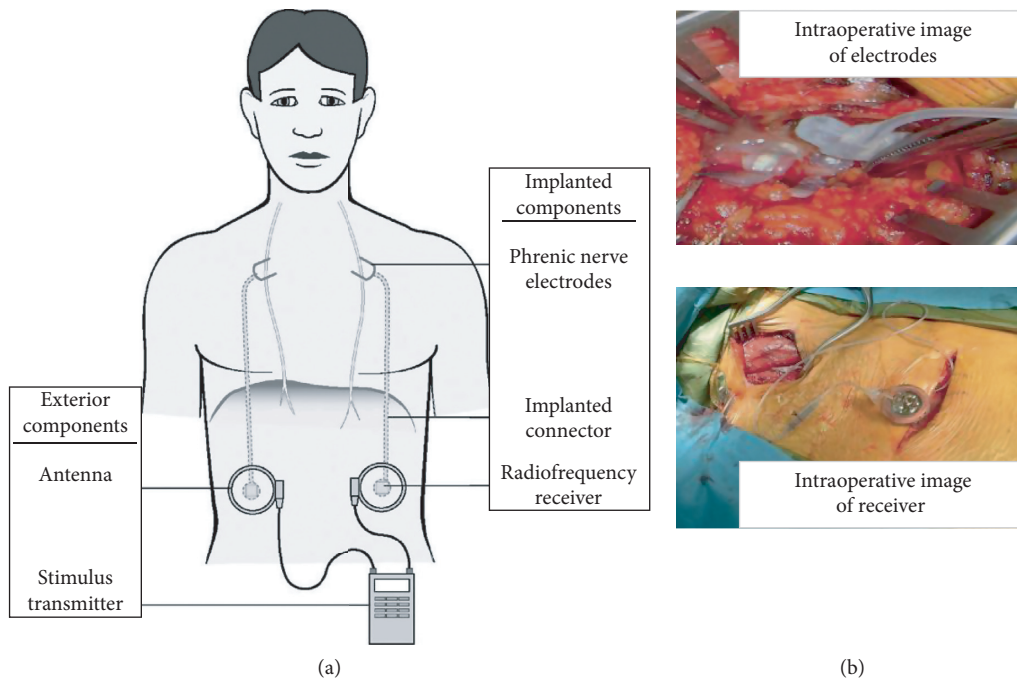


FIGURE 3: General view of the diaphragmatic pacing system [24, 25]. (a) It contains the implanted part and exterior part, and the communication method between them is wireless transmission. The external controller regulates phrenic nerve stimulation parameters (waveform, frequency, respiratory cycle, etc.). The internal part is responsible for transmitting stimulation parameters to the phrenic nerve to control diaphragm contraction. (b) Implantation of diaphragm pacemaker components.

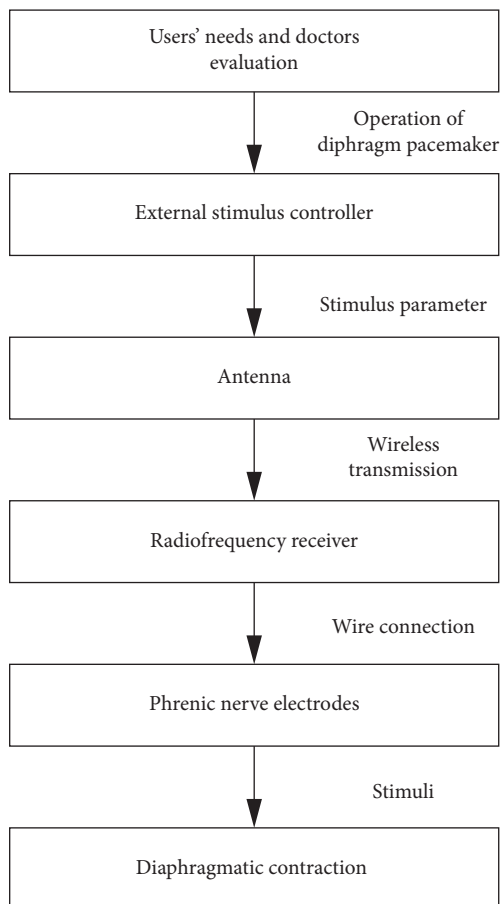


FIGURE 4: DP working flowchart. It is drawn according to the principles introduced earlier.

tidal volume generated by unilateral phrenic nerve stimulation was maintained at 700–1000 ml at 12/min, 16/min, and 18/min, which fully meets the physiological needs of human respiration [30].

3.1.2. Parameter of DP. The stimulation waveform of phrenic nerve is displayed in Figure 5 [35]. T_1 and T_2 represent the time of the respiratory cycle and inspiration respectively, so the expiratory time equals to the difference between T_1 and T_2 . Each blue vertical line in Figure 5 denotes a stimulus pulse, and its pulse width is T_i . In the inspiratory phase (T_2), the pulses (I_{TH} is the minimum stimulation threshold, and I_{TV} is the maximum stimulus intensity) to stimulate phrenic nerve are given to induce the contraction of the diaphragm to increase the tidal volume. While in the expiratory stage, there is no electrical stimulation rendered to make the diaphragm and expel the gas. Accordingly, the working process of the diaphragm pacemaker is to simulate human physiological respiration. Furthermore, after the operation, the stimulation parameters of the signal in Figure 5 should be adjusted based on the actual situation of the patient.

The waveform of the stimulus affects the physiological response and safety of the nerve. For the safety and simplicity of stimulation, the traditional stimulus waveform adopts square wave in DP [35]. The new stimulus waveforms (see Figure 6) as a physiological reaction of the diaphragm may be more effective, which need further research [36].

To avoid to phrenic nerve injury and diaphragmatic fatigue, patients with SCI to choose appropriate pacing

TABLE 1: The main difference between three kinds of diaphragm pacemakers [4, 26].

Manufacturer	Avery, USA	Atrotech, FIN	Medimplant, AUS
Developed time	1960	1980	1984
Electrodes	Monopolar; bipolar	Quadripolar	Quadripolar
Breaths/min	6–24	8–35	5–60
Pulse width (ms)	150	200	100–1000
FDA approval	Yes	Invalid	No
Electrode implantation	Easy	Relatively difficult	Complicated
Diaphragm fatigue	Yes	Relatively light	Relatively light

TABLE 2: Functional evaluation of the phrenic nerve and diaphragm [31–33].

Method	Implementation process	Evaluation criteria
Nerve conduction time	Transcutaneous electrical stimulation with a unipolar needle electrode on the neck to observe the action potential time of diaphragm electromyography	7.5~9 ms [31]
X-ray fluoroscopy	Electrical stimulation of phrenic nerve to observe the descending degree of the diaphragm by X-ray fluoroscopy	>5 cm [32] (5–8 cm)
Transdiaphragm pressure	Calculating the difference between abdominal pressure and pleural pressure by balloon catheter placed in oesophagus and stomach	Unilateral pacing: 10 cm H ₂ O [33]

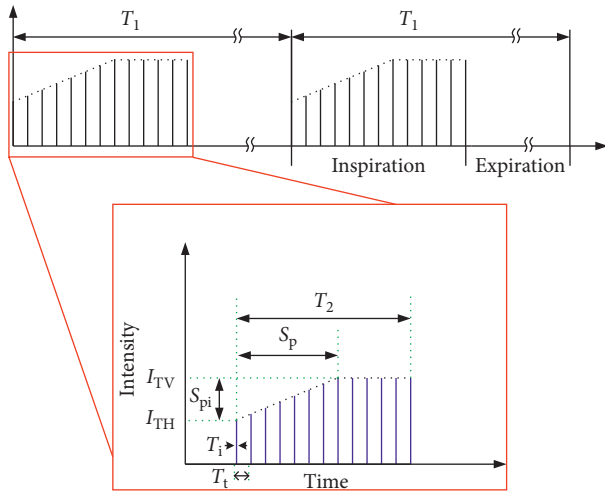


FIGURE 5: Stimulation signal [35]. Stimulation parameters of DP include breathing cycle, stimulation waveform, and pulse width.

parameters is extremely important. Unlike cardiac pacing, a single electrical stimulation pulse does not cause adequate ventilation. DP requires more than 30 continuous stimulation waves at a time. Moreover, several studies have shown that low-frequency pacing and lower respiratory frequency are more tolerable, making muscle structure and function have better chances. Previous successful clinical experience shows that it is safe and effective to adjust the stimulation parameters with pulse frequency of 25 Hz properly, respiratory frequency of 15 breath/min, and the inspiratory duration of one-third of the respiratory cycle [37] making the diaphragm twitch slowly and fatigue-resistant. In 1981, Oda et al. [38] studied the electrical parameters of DP in dogs. They found that the change of stimulation frequency had a great influence on diaphragmatic fatigue. High frequency (33 Hz) and narrow pulse interval easily lead to rapid and obvious fatigue. In 2005, Anthony F. DiMarco et al. [39]

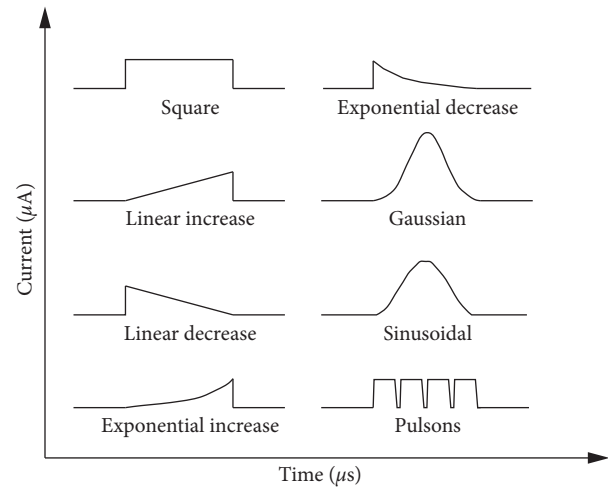


FIGURE 6: Varied Stimulation waveform [36]. The effects of different stimulus waveforms on neurophysiology need to be further studied.

researched the application of DP in patients with quadriplegia. They set the stimulation parameter (stimulus frequency 20 Hz, inspiratory time 1.1s, and respiratory rate 10–12 breaths/min) to restore the spontaneous breathing in four patients successfully.

However, continuous and long-term stimulation (24 h/day for several weeks) would harm the function and structure of the diaphragm, resulting in diaphragm fatigue and damage [40, 41]. The reasonable use time of DP should be in 18 hours/day, so many patients choose to use DP at night and ventilator during the day. Besides, due to the rapid airflow in the trachea caused by DP, the negative pressure in the neck airway may occur, which will give rise to the stenosis of the upper respiratory tract. It was suggested that the continuous use time of DP should not exceed 12 hours or 16 hours a day [40, 41].

As has been mentioned above, interpulse interval, stimulation frequency, and inspiratory time are the key parameters of diaphragm pacemaker. Brouillett [42] discussed the effects of these stimulus parameters on tidal volume for DP in infants and children, as shown in Figures 7 and 8. Figure 7 shows the trend of tidal volume in three patients at different pulse intervals, which can be fitted into a mathematical formula curve [42]:

$$V_T = \frac{a}{1 + be^{-k \cdot \text{Hz}}} \quad (1)$$

The value of tidal volume under the stimulation of the shortest (about 30 ms) and longest pulse interval approached to two asymptotes.

Similar to Figure 8, the trend of tidal volume value in Figure 8 with the increase of inspiratory time is also by the asymptotic regression, which can be described by [42]

$$V_T = a(1 - e^{-kt}). \quad (2)$$

Accordingly, based on meeting the needs of patients' ventilation, the balance between less inspiratory time and lower interpulse interval should be achieved in determining pacing parameters.

3.2. Intercostal Muscles Pacing. DP via electric stimulation of bilateral phrenic nerves can restore spontaneous respiratory function in patients with high SCI. However, some patients with SCI are not candidates for diaphragm pacing due to injury of phrenic motor neuron pools or phrenic nerves. Intercostal muscles being the secondary respiratory muscles can contribute 35%–40% of tidal volume. Some researchers have suggested that intercostal muscles can be activated by electrical stimulation [8, 43–46].

A typical study showed that the combined stimulation of the intercostal nerve and unilateral phrenic nerve could separate patients with SCI from the ventilator [44]. This method requires one electrode placed on the ventral surface of the upper thoracic spinal cord by using hemi-laminectomy to activate intercostal muscles and the other electrode implanted into the unilateral phrenic nerve. After 15–30 weeks of recovery after surgery, the patients' inspiratory volume can reach 0.55 L–1.31 L, and they can leave the ventilator for spontaneous breathing daily for 16 to 24 hours [44]. Direct stimulation of the upper thoracic spinal cord will cause contraction of the intercostal muscles, triggering the generation of inspired volume. In animal studies, where the diaphragm and intercostal muscles breathe separately, the gas exchange induced by this way alone is the same as that caused by bilateral stimulation of phrenic nerve alone [45].

In addition, high-frequency spinal cord stimulation (HF-SCS) is a new and physiologically significant method of activating inspiratory muscles. It was proved that during high-frequency spinal cord stimulation at the T2 level, the peak discharge frequency of a single motor unit of the intercostal muscles was similar to that of spontaneous breathing [46].

Like diaphragmatic pacing, intercostal pacing restores the patients' sense of smell, speech, and social activities and

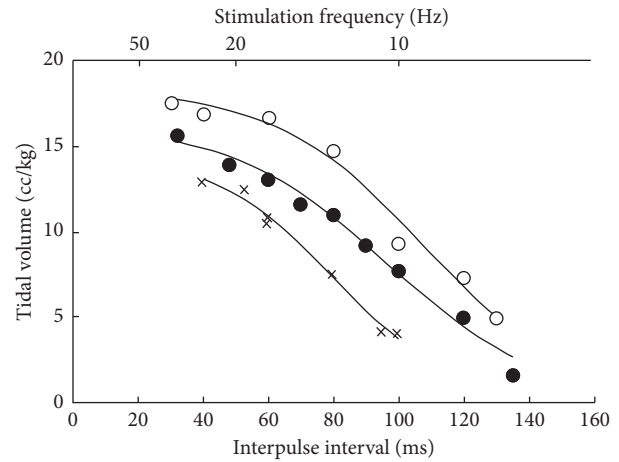


FIGURE 7: Effect of pulse interval in tidal volume [42]. There are upper and lower limits for the impact of pulse interval on tidal volume.

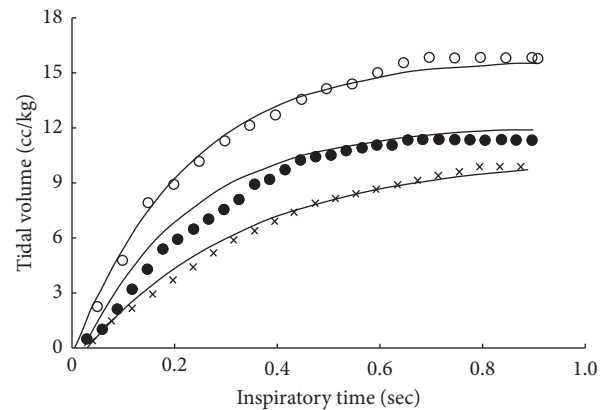


FIGURE 8: Effect of inspiratory time on tidal volume [42]. There is an upper limit to the effect of inspiratory time on tidal volume in stimulation parameters.

generally increases patient happiness. Although this method has some side effects, such as mild hand flexion and upper body muscle contraction, it has less impact on the human body. Intercostal pacing can be a second treatment for patients with unfortunate diaphragm pacing effect. FDA has approved the method through IDE [24], and we believe that it can be applied in the market soon.

4. Mechanical Ventilation

4.1. Principle. Mechanical ventilation (MV) with a history of nearly 600 years is one of the essential means for the treatment of respiratory diseases. Since positive-pressure mechanical ventilation (PPMV) successfully rescued polio patients in 1950s, mechanical ventilation support has been widely used in the clinical operation and the treatment of respiratory disorder [47]. As in Figure 9, the ventilator provides positive air pressure higher than the alveolar pressure into the lungs to replace the contraction and expansion of human respiratory muscles [48, 49]. It can help the patients' respiratory muscles act passively and ensure the

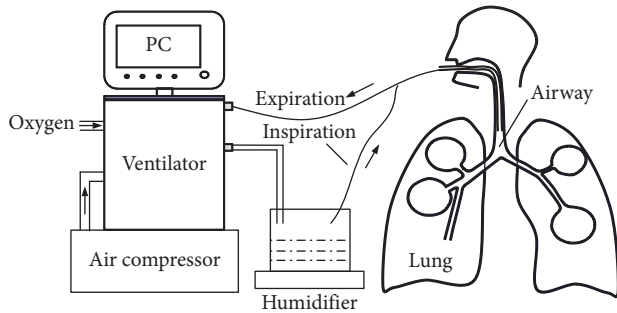


FIGURE 9: Positive-pressure mechanical ventilation (MV). It is a method to assist or completely replace the patient.

O₂ supply and CO₂ exhaust. To simulate the function of the human nasal cavity, the gas provided by the ventilator needs to be heated and humidified, and the oxygen concentration is higher than the atmosphere. It is mainly composed of the mechanical module, controller, and human-computer interaction. The mechanical module realises the compression and storage of air and transfers it to the patient [50]. The controller controls the work of the entire ventilator system [50]. Human-computer interaction is mainly for medical staff to set the parameters of the ventilator (tidal volume, pressure, flow, and time) [50].

However, inflating the lung is a nonphysiological ventilation mode, which may contribute to the lung injury characterised pathologically by pneumonema, oxygen intoxication, and barotraumas [51, 52]. Although the pathogenesis of ventilator-induced lung injury is not fully understood, there is a consensus that the ventilation pressure higher than that of spontaneous respiration will lead to overexpansion of the alveoli and further results in lung injury and the inflammation of body's organs [53, 54]. As a consequence, a concept of pulmonary protective ventilation strategy was proposed to minimise lung injury. Its content mainly includes using low tidal volume to avoid overexpansion of alveoli caused by high tidal volume or airway ventilation, applying sufficient pressure to make the collapsed alveoli open again while inhaling, and keeping the alveoli open with appropriate positive end-expiratory pressure (PEEP) when exhaling [51]. These two ventilation strategies have been proven to be advantageous to prevent alveolar failure and lung injury [55].

4.2. Management of Mechanical Ventilation. According to the connection between the ventilator and the human body, MV can be divided into invasive and noninvasive methods. For the different degrees of respiratory dysfunction caused by SCI, it is necessary for us to accurately evaluate the physiological status of each patient (diaphragmatic function and lung function) and then select the appropriate ventilation mode [56]. The complete SCI patients (C1–C5) with paralysis of the diaphragm and intercostal muscles require to be built effective artificial airway and realisation of MV to ensure the safety of life [57]. For incomplete or low SCI (below C5), conservative treatments can be used. However, the lung function of vital capacity (VC) and arterial blood

gas analysis should be strictly monitored to prevent respiratory failure. Clinical practice guidelines for high SCI suggest that patients have an initial tidal volume of 15 ml/kg for mechanical ventilation and increase with daily chest radiograph atelectasis [58].

Moreover, another critical problem in the management of MV for patients with SCI is the timing of weaning. Whether the patients with SCI can be successfully weaned depends on the location and degree. The success rate of weaning for SCI below C5 is significantly higher than that above C4 [59]. The patients' weaning should be performed in strict accordance with the blood gas analysis indexes, leukocyte count, tidal volume, etc. After weaning, the patients' condition should be grimly observed to avoid danger.

5. Respiratory Muscle Training

The advancement of the medical level has gradually increased the survival rate of patients with SCI, but the respiratory function of patients with 5 years high SCI will decline [60]. The function of inspiratory and expiratory muscles is inhibited in patients with high SCI due to the injury of neurons controlling the respiratory muscle group. This will lead to the reduction of lung capacity and chest wall compliance, then result in the incidence of atelectasis, dyspnea, and respiratory tract infection, and finally seriously affect the health and quality of life of patients with SCI [61–63]. The degree of respiratory muscle injury depends on the segment and degree of injury.

Respiratory muscle training (RMT), a treatment technique, is to use impedance load, threshold pressure load, and other means to carry out continuous and standardised training of muscles related to respiratory function, which in turn improves the strength and endurance of respiratory muscles [63]. It is inappropriate for such patients with SCI above C3 segment due to complete paralysis of all respiratory muscles. Patients with SCI (C3–T12 segment) may lead to partial respiratory muscle failure. Therefore, improving the strength of respiratory muscles through RMT for the recovery of respiratory dysfunction due to SCI is effective [63, 64].

RMT, including inspiratory muscle training and expiratory muscle training, needs to choose the appropriate treatment time and intensity. Each treatment should be performed according to the experience of a professional doctor and the guidance of the physiological literature.

SCI patients often use respiratory trainers for respiratory muscle training [66, 67]. Figure 10 is a photo of expiratory muscle training device [65]. As shown in Figure 11, before using the device, the patient's nose needs to be tightened with a clip [65]. The patient is then asked to take a deep breath, hold the cheeks (to reduce lip leaks), and blow hard on the device. When the device detects that the air pressure reaches a threshold, they are reminded to stop exhaling. The treatment requires to take approximately 4–8 weeks, and approximately 25 to 30 training sessions need to be completed each day [68–70]. Clinicians can check the maximum expiratory pressure (MEP) and pulmonary function parameters (FEV1 and FVC) of trained patients every week to evaluate the effect of treatment.

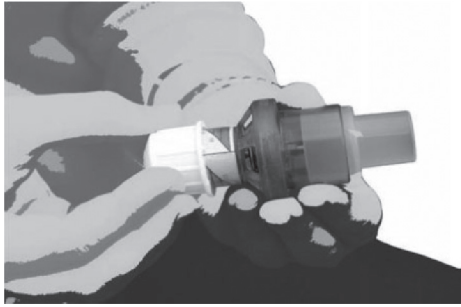


FIGURE 10: Expiratory muscle trainer [65]. It sets a pressure threshold through a spring-controlled check valve to enhance expiratory muscle strength.



FIGURE 11: Respiratory muscle training posture [65]. The patient holds the device with his lips, bites his mouth, and tries to blow into the device.

Many clinicians have studied the effect of RMT on the recovery of respiratory function in patients with SCI. There are two main methods they use to study this subject: one is clinical research verification and the other is meta-analysis or review based on literature search. Postma concluded that, after the treatment of inspiratory muscle impedance, the maximum inspiratory pressure and mental state of 40 patients with SCI had a short-term improvement [64]. Rutchik et al. conducted respiratory muscle confrontation training for 10 patients with cervical spinal cord injury for 8 weeks. Then, they calculated that these patients' mechanical parameters such as vital capacity, maximum inspiratory pressure, and functional residual capacity all increased [71]. Also, meta-analysis results showed that RMT is more effective than traditional rehabilitation methods in improving vital capacity, inspiratory capacity, maximum inspiratory pressure, and maximum voluntary ventilation [63]. In general, RMT can effectively reduce the probability of lung infection in patients with SCI and improve lung function. Therefore, RMT is worth promoting in the clinic.

6. Discussion

Currently, various techniques of respiratory function reconstruction of SCI have been widely used in clinical practice, effectively maintaining the lives of some patients. However, the shortcomings and limitations of these

technologies have led to many patients not being able to get treatment or poor treatment results.

MV is the preferred method of restoring respiratory function in patients with SCI. It can provide temporary respiratory support and continue the patients' life. However, this is a way to help patients breathe passively and cannot help patients with spontaneous breathing function. At the same time, prolonged mechanical ventilation can cause problems such as bedsores, respiratory infections, and airway secretion clearance problem [72]. Compared to MV, DP can restore the patients' language function and social ability and reduce the economic burden [73, 74]. The cost of performing diaphragmatic pacing is expensive. The price of each type of DP is between US\$50000–60000 [4]. Surgery, hospitalisation, and follow-up costs add another US\$20000 [4]. Therefore, DP is more likely to be accepted by patients with SCI. The prerequisite for breathing muscle training is that the patient has a certain ability to breathe spontaneously, which causes that respiratory muscle training can only be used as an auxiliary respiratory function rehabilitation treatment for patients with mild SCI.

Overall, the recovery of respiratory function for SCI is developing in a direction that is meeting the physiological needs of patients. DP is the most effective in improving participants' quality of life and happiness among the three treatments. However, some unavoidable fatal disadvantages of DP, such as equipment failure, postoperative infection, and unknown neurological damage, need to be urgently addressed [24].

The development of microelectronic technology has promoted the improvement of the control function and expansion function of the single-chip microcomputer, which has also been widely used in medical instruments and equipment. Meanwhile, modern control theory achieves fast response and stability of complex systems with time-varying and multivariable [75–78]. The medical hardware platform based on single-chip technology can accurately process and recognize the biological signals of the human body in real time [79, 80]. Zbrzeski developed a multifunctional hardware platform to realise the real-time collection, calculation, display, and storage of biological signals and then applied it to the animal model of DP.

For the current open-loop DP system not responding to changes in equipment components and physiological needs, some researchers [81, 82] have proposed to establish a closed-loop diaphragm pacing system relying on changes in respiratory airflow (Figure 12). Nevertheless, closed-loop DP has not yet appeared on the market and in clinical applications.

The PG/PS controller [81, 83], containing two modules PG and PS, builds a closed-loop diaphragm pacing system. The pacing cycle is set in the PG module, and the PS module adaptively adjusts the stimulation parameters with the change of actual respiratory airflow to make ideal respiratory airflow. The PS module consists of a single-layer neural network, in which each neuron outputs a raised cosine function ($y_j(t)$) as a basic function. The output value $Z(t)$ of PS is the sum of the weighted values ($\omega_j(t)$) of the basic functions:

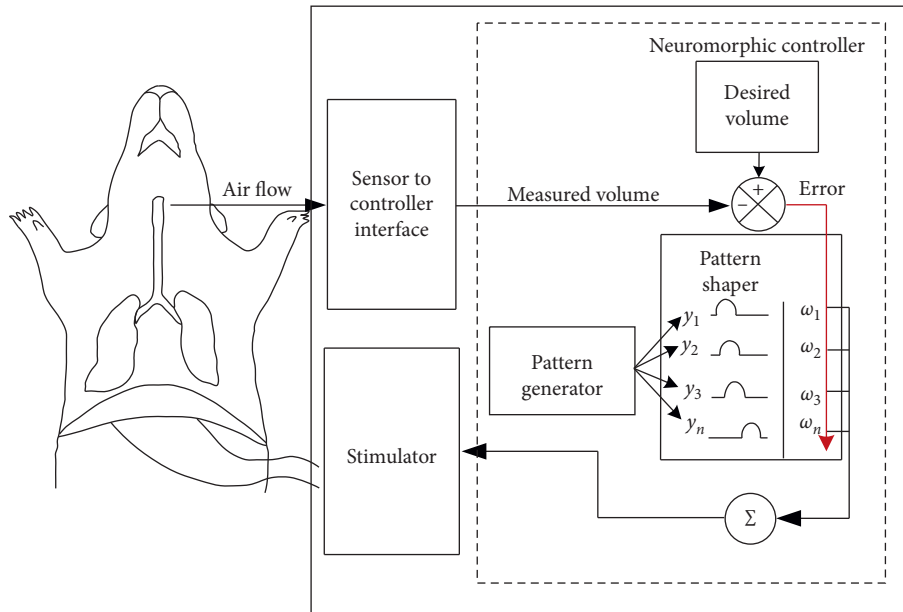


FIGURE 12: Animal model of closed-loop diaphragm pacing system [81]. The system controller adjusts the stimulation parameters online based on the error between the measured respiratory airflow and the ideal airflow.

$$Z(t) = \sum_{j=1}^m \omega_j(t)y_j(t). \quad (3)$$

Also, the EMG signal reflects muscle movement [84] and the respiratory parameters can also be evaluated through the characteristics of the diaphragm EMG signal [85, 86]. Therefore, using the surface diaphragmatic myoelectric signal as feedback is also a research direction to establish a closed-loop diaphragmatic pacing system.

7. Conclusions

High spinal cord injury is one of the most severe injuries, which can lead to death from respiratory failure. This review focuses on respiratory dysfunction in patients with SCI and uses three commonly used devices to restore respiratory function, namely, electrical stimulation, mechanical ventilation, and respiratory muscle training. Compared with the other two treatment methods, electrical stimulation is the most effective treatment method.

Improvements in current respiratory therapy for SCI should underline safety, reliability, and intelligence, which means close to human physiology, fewer complications and side effects, and reliable product performance. Real prospects are presented below:

- (1) Investigate neural signals more meet respiratory physiological patterns. When the pulse signal stimulates the phrenic nerve, the patient produces a rapid ventilation. Hence, a stimulus waveform has the same volume of ventilation as a person’s spontaneous breathing should be explored.
- (2) Improve diaphragmatic pacemaker surgery. High-frequency spinal cord electrical stimulation is also the development direction of diaphragm pacing in

the future due to the advantages of less surgical trauma and closer to the physiological mode.

- (3) Emphasize joint stimulation between the diaphragm and other respiratory muscles to make the respiratory airflow closer to the normal respiratory airflow.

Conflicts of Interest

The authors declare that they have no conflicts of interest.

Acknowledgments

The research was funded by Grant (2019M660391) of China Postdoctoral Science Foundation and the Open Foundation of the State Key Laboratory of Fluid Power and Mechatronic Systems (GZKF-201920).

References

- [1] R. Kumar, J. Lim, R. A. Mekary et al., “Traumatic spinal injury: global epidemiology and worldwide volume,” *World Neurosurgery*, vol. 113, pp. 345–363, 2018.
- [2] Y. S. Xu, D. Q. Luo, W. H. Pan et al., “Epidemiological analysis of traumatic cervical spinal cord injury,” *Chinese Journal of Emergency Medicine*, vol. 28, no. 1, pp. 84–89, 2019.
- [3] R. Brown, A. F. DiMarco, J. D. Hoit, and E. Garshick, “Respiratory dysfunction and management in spinal cord injury,” *Respiratory Care*, vol. 51, no. 8, pp. 853–870, 2006.
- [4] A. F. DiMarco and G. H. Creasey, “Neuroprosthetic control of respiratory muscles,” *Series on Bioengineering and Biomedical Engineering*, vol. 40, no. 12, pp. 566–600, 2017.
- [5] A. Alshekhlee, R. P. Onders, T. U. Syed, M. Elmo, and B. Katirji, “Phrenic nerve conduction studies in spinal cord injury: applications for diaphragmatic pacing,” *Muscle & Nerve*, vol. 38, no. 6, pp. 1546–1552, 2008.

- [6] A. F. DiMarco and K. E. Kowalski, "Effects of chronic electrical stimulation on paralyzed expiratory muscles," *Journal of Applied Physiology*, vol. 104, no. 6, pp. 1634–1640, 2008.
- [7] A. F. DiMarco, "Neural prostheses in the respiratory system," *Journal of Rehabilitation Research and Development*, vol. 38, no. 6, pp. 601–607, 2001.
- [8] A. F. DiMarco, M. D. Altose, A. Cropp et al., "Activation of the Inspiratory intercostal muscles by electrical stimulation of the spinal cord," *American Review Respiratory Disease*, vol. 136, no. 6, pp. 1385–1390, 1988.
- [9] L. Guth, L. Soutter, K. Frank, J. B. Campbell, and J. B. Lloyd, "Diaphragmatic function following anastomosis of recurrent laryngeal and phrenic nerves," *Experimental Neurology*, vol. 2, no. 3, pp. 251–260, 1960.
- [10] J. Polentes, J. C. Stamegna, M. Nieto-Sampedro, and P. Gauthier, "Phrenic rehabilitation and diaphragm recovery after cervical injury and transplantation of olfactory ensheathing cells," *Neurobiology of Disease*, vol. 16, no. 3, pp. 638–653, 2004.
- [11] N. J. Livingston, "The intercostal to phrenic nerve transfer: an effective means of reanimating the diaphragm in patients with high cervical spine injury," *Plastic and Reconstructive Surgery*, vol. 105, no. 4, pp. 1255–1261, 2000.
- [12] National Spinal Cord Injury Statistical Center, "Spinal cord injury facts and figures at a glance," *The Journal of Spinal Cord Medicine*, vol. 28, no. 4, pp. 379–380, 2005.
- [13] World Health Organization and International Spinal Cord Society, *International Perspectives on Spinal Cord Injury*, pp. 3–10, World Health Organization, Geneva, Switzerland, 2013.
- [14] Y. J. HAN, G. M. LI, D. H. LUO et al., "The influencing factors of early death in cervical spinal cord injury patients (A report of 81 cases)," *China Medical Herald*, vol. 5, no. 18, pp. 42–43, 2008.
- [15] A. B. Jackson and T. E. Groomes, "Incidence of respiratory complications following spinal cord injury," *Archives of Physical Medicine and Rehabilitation*, vol. 75, no. 3, pp. 270–275, 1994.
- [16] R. P. Onders, "Functional electrical stimulation," *Handbook of Clinical Neurology*, vol. 109, pp. 275–282, 2012.
- [17] W. W. Glenn, J. H. Hageman, A. Mauro et al., "Electrical stimulation of excitable tissue by radio frequency transmission," *Annals of Surgery*, vol. 160, no. 3, pp. 338–350, 1964.
- [18] W. W. L. Glenn, W. G. Holcomb, A. J. McLaughlin, J. M. O'Hare, J. F. Hogan, and R. Yasuda, "Total ventilatory support in a quadriplegic patient with radiofrequency electrophrenic respiration," *New England Journal of Medicine*, vol. 286, no. 10, pp. 513–516, 1972.
- [19] W. W. Glenn and M. L. Phelps, "Diaphragm pacing by electrical stimulation of the phrenic nerve," *Neurosurgery*, vol. 17, no. 6, pp. 974–984, 1985.
- [20] P. Khong, A. Lazzaro, and R. Mobbs, "Phrenic nerve stimulation: the Australian experience," *Journal of Clinical Neuroscience*, vol. 17, no. 2, pp. 205–208, 2010.
- [21] J. A. Eleftheriades, J. A. Quin, J. F. Hogan et al., "Long-term follow-up of pacing of the conditioned diaphragm in quadriplegia," *Pacing and Clinical Electrophysiology*, vol. 25, no. 6, pp. 897–906, 2002.
- [22] W. W. L. Glenn, J. F. Hogan, M. L. Phelps et al., "Ventilatory support of the quadriplegic patient with respiratory paralysis by diaphragm pacing," *Surgical Clinics of North America*, vol. 60, no. 5, pp. 1055–1078, 1980.
- [23] W. W. L. Glenn, J. F. Hogan, J. S. O. Loke, T. E. Ciesielski, M. L. Phelps, and R. Rowedder, "Ventilatory support by pacing of the conditioned diaphragm in quadriplegia," *New England Journal of Medicine*, vol. 310, no. 18, pp. 1150–1155, 1984.
- [24] A. F. DiMarco, "Phrenic nerve stimulation in patients with spinal cord injury," *Respiratory Physiology & Neurobiology*, vol. 169, no. 2, pp. 200–209, 2009.
- [25] S. V. Abdunnur and D. H. Kim, "Phrenic nerve stimulation: technology and clinical applications," *Stimulation of the Peripheral Nervous System*, vol. 29, pp. 64–75, 2016.
- [26] G. Creasey, J. Eleftheriades, A. DiMarco et al., "Electrical stimulation to restore respiration," *Journal of Rehabilitation Research and Development*, vol. 33, no. 2, pp. 123–132, 1996.
- [27] W. T. Abraham, D. Jagielski, O. Oldenburg et al., "Phrenic nerve stimulation for the treatment of central sleep apnea," *JACC: Heart Failure*, vol. 3, no. 5, pp. 360–369, 2015.
- [28] M. L. Yang, H. M. Zhao, J. J. Li et al., "The clinic experience of implantable diaphragm pacer in a patient with high cervical spinal cord injury and literature review," *Chinese Journal of Tuberculosis and Respiratory Diseases*, vol. 41, no. 9, pp. 718–723, 2018.
- [29] R. Chen, L. I. Jianjun, X. Meng et al., "Application of diaphragm pacing technology in respiratory function reconstruction in patients with cervical spinal cord injury," *Chinese Journal of Rehabilitation Theory and Practice*, vol. 21, no. 2, pp. 157–162, 2015.
- [30] O. Oldenburg, T. Bitter, H. Fox, D. Horstkotte, and K.-J. Gutleben, "Effects of unilateral phrenic nerve stimulation on tidal volume," *Herz*, vol. 39, no. 1, pp. 84–86, 2014.
- [31] D. K. McKenzie and S. C. Gandevia, "Phrenic nerve conduction times and twitch pressures of the human diaphragm," *Journal of Applied Physiology*, vol. 58, no. 5, pp. 1496–1504, 1985.
- [32] R. K. Shaw, W. W. L. Glenn, J. F. Hogan, and M. L. Phelps, "Electrophysiological evaluation of phrenic nerve function in candidates for diaphragm pacing," *Journal of Neurosurgery*, vol. 53, no. 3, pp. 345–354, 1980.
- [33] A. Mier, C. Brophy, J. Moxham, and M. Green, "Twitch pressures in the assessment of diaphragm weakness," *Thorax*, vol. 44, no. 12, pp. 990–996, 1989.
- [34] A. K. Karlsson, L. Dernevik, and B. Houlitz, "Spinal cord injuries. An intact nerve can be enough for a successful phrenic nerve stimulation," *Lakartidningen*, vol. 106, no. 11, pp. 11–17, 2009.
- [35] X. Lu, D. Guiraud, S. Renaux, T. Similowski, and C. A. Coste, *Monitoring Phrenic Nerve Stimulation-Induced Breathing via Tracheal Sounds*, Hal-Lirmm, RehabWeek, Toronto, Canada, 2019.
- [36] C. Günter, J. Delbeke, and M. Ortiz-Catalan, "Safety of long-term electrical peripheral nerve stimulation: review of the state of the art," *Journal of Neuro Engineering and Rehabilitation*, vol. 16, no. 13, pp. 1–16, 2019.
- [37] W. W. L. Glenn, W. G. Holcomb, J. Hogan et al., "Diaphragm pacing by radiofrequency transmission in the treatment of chronic ventilatory insufficiency," *The Journal of Thoracic and Cardiovascular Surgery*, vol. 66, no. 4, pp. 505–520, 1973.
- [38] T. Oda, W. W. L. Glenn, Y. Fukuda, J. F. Hogan, and J. Gorfien, "Evaluation of electrical parameters for diaphragm pacing: an experimental study," *Journal of Surgical Research*, vol. 30, no. 2, pp. 142–153, 1981.
- [39] A. F. DiMarco, R. P. Onders, A. Ignagni, K. E. Kowalski, and J. T. Mortimer, "Phrenic nerve pacing via intramuscular diaphragm electrodes in tetraplegic subjects," *Chest*, vol. 127, no. 2, pp. 671–678, 2005.

- [40] W. W. L. GLENN, "Diaphragm pacing: present status," *Pacing and Clinical Electrophysiology*, vol. 1, no. 3, pp. 357–370, 1978.
- [41] C. E. Hunt, S. V. Matalon, T. R. Thompson et al., "Central hypoventilation syndrome: experience with bilateral phrenic nerve pacing in 3 neonates," *American Review of Respiratory Disease*, vol. 118, no. 1, pp. 23–28, 1978.
- [42] R. T. Brouillette, M. N. Ilbawi, L. Klemka-Walden, and C. E. Hunt, "Stimulus parameters for phrenic nerve pacing in infants and children," *Pediatric Pulmonology*, vol. 4, no. 1, pp. 33–38, 1988.
- [43] A. F. DiMarco, K. Budzinska, and G. S. Supinski, "Artificial ventilation by means of electrical activation of intercostal/ accessory muscles alone in anesthetized dogs," *American Review of Respiratory Disease*, vol. 139, no. 4, pp. 961–967, 1988.
- [44] A. F. DiMarco, Y. Takaoka, and K. E. Kowalski, "Combined intercostal and diaphragm pacing to provide artificial ventilation in patients with tetraplegia," *Archives of Physical Medicine and Rehabilitation*, vol. 86, no. 6, pp. 1200–1207, 2005.
- [45] A. F. DiMarco, A. F. Connors Jr, and K. E. Kowalski, "Gas exchange during separate diaphragm and intercostal muscle breathing," *Journal of Applied Physiology*, vol. 96, no. 6, pp. 2120–2124, 2004.
- [46] A. F. DiMarco and K. E. Kowalski, "Intercostal muscle pacing with high frequency spinal cord stimulation in dogs," *Respiratory Physiology & Neurobiology*, vol. 171, no. 3, pp. 218–224, 2010.
- [47] B. Ibsen, "The anaesthetist's viewpoint on the treatment of respiratory complications in poliomyelitis during the epidemic in Copenhagen, 1952," *Proceedings of the Royal Society of Medicine*, vol. 47, no. 1, pp. 72–74, 1954.
- [48] E. Kondili, G. Prinianakis, and D. Georgopoulos, "Patient-ventilator interaction," *British Journal of Anaesthesia*, vol. 91, no. 1, pp. 106–119, 2003.
- [49] S. Ren, M. L. Cai, Y. Shi, W. Q. Xu et al., "Influence of bronchial diameter change on the airflow dynamics based on a pressure-controlled ventilation system," *International Journal for Numerical Methods in Biomedical Engineering*, vol. 34, no. 3, pp. 1–14, 2018.
- [50] F. Zhou, W. Guan, K. Sierszecki et al., "Component-based design of software for embedded control systems: the medical ventilator case study," in *Proceedings of the 2009 International Conference on Embedded Software and Systems*, pp. 157–163, IEEE, Zhejiang, China, May 2009.
- [51] A. S. Slutsky and V. M. Ranieri, "Ventilator-induced lung injury," *The New England Journal of Medicine*, vol. 369, pp. 2216–2136, 2013.
- [52] G. Nash, J. B. Blennerhassett, and H. Pontoppidan, "Pulmonary lesions associated with oxygen therapy and artificial ventilation," *New England Journal of Medicine*, vol. 276, no. 7, pp. 368–374, 1967.
- [53] R. D. Stevens, C. Lazaridis, and J. A. Chalela, "The role of mechanical ventilation in acute brain injury," *Neurologic Clinics*, vol. 26, no. 2, pp. 543–563, 2008.
- [54] M. Kearns and D. Shimabukuro, "Respiratory complications and management of mechanical ventilation in cervical spine injury," *ICU Director*, vol. 3, no. 5, pp. 220–223, 2012.
- [55] M. B. P. Amato, C. S. V. Barbas, D. M. Medeiros et al., "Effect of a protective-ventilation strategy on mortality in the acute respiratory distress syndrome," *New England Journal of Medicine*, vol. 338, no. 6, pp. 337–354, 1998.
- [56] R. Galeiras Vázquez, P. Rascado Sedes, M. Mourelo Fariña, A. Montoto Marqués, and M. E. Ferreiro Velasco, "Respiratory management in the patient with spinal cord injury," *BioMed Research International*, vol. 2013, Article ID 168757, 12 pages, 2013.
- [57] E. B. Marsolais, M. L. Boninger, P. McCormick et al., "Respiratory management following spinal cord injury: a clinical practice guideline for health care professionals," *Journal of Spinal Cord Medicine*, vol. 28, no. 3, pp. 259–293, 2005.
- [58] S. Berney, P. Bragge, C. Granger, H. Opdam, and L. Denehy, "The acute respiratory management of cervical spinal cord injury in the first 6 weeks after injury: a systematic review," *Spinal Cord*, vol. 49, no. 1, pp. 17–29, 2011.
- [59] A. E. Chiodo, W. Scelza, and M. Forchheimer, "Predictors of ventilator weaning in individuals with high cervical spinal cord injury," *The Journal of Spinal Cord Medicine*, vol. 31, no. 1, pp. 72–77, 2008.
- [60] K. Postma, J. A. Haisma, S. de Groot et al., "Changes in pulmonary function during the early years after inpatient rehabilitation in persons with spinal cord injury: a prospective cohort study," *Archives of Physical Medicine and Rehabilitation*, vol. 94, no. 8, pp. 1540–1546, 2013.
- [61] C. P. Cardozo, "Respiratory complications of spinal cord injury," *The Journal of Spinal Cord Medicine*, vol. 30, no. 4, pp. 307–308, 2007.
- [62] R. Brown, A. F. DiMarco, J. D. Hoit et al., "Respiratory dysfunction and management in spinal cord injury," *Respiratory Care*, vol. 51, no. 8, pp. 869–870, 2006.
- [63] Y. Xu, Y. Gao, Q. Xie et al., "Efficacy of respiratory muscle training on pulmonary function of spinal cord injury patients: a meta-analysis," *Chinese Journal Of Evidence-Based Medicine*, vol. 17, no. 10, pp. 1150–1157, 2017.
- [64] K. Postma, J. A. Haisma, M. T. E. Hopman, M. P. Bergen, H. J. Stam, and J. B. Bussmann, "Resistive inspiratory muscle training in people with spinal cord injury during inpatient rehabilitation: a randomized controlled trial," *Physical Therapy*, vol. 94, no. 12, pp. 1709–1719, 2014.
- [65] C. Sapienza, M. Troche, T. Pitts, and P. Davenport, "Respiratory strength training: concept and intervention outcomes," *Seminars in Speech and Language*, vol. 32, no. 1, pp. 021–030, 2011.
- [66] E. J. Roth, K. W. Stenson, S. Powley et al., "Expiratory muscle training in spinal cord injury: a randomized controlled trial," *Archives of Physical Medicine and Rehabilitation*, vol. 91, no. 6, pp. 857–861, 2010.
- [67] Y. Bao and J. H. Sun, "The effect of respiratory trainer in the care of the patients with cervical spinal cord injuries," *Medical Journal of West China*, vol. 23, no. 12, pp. 2449–2450, 2011.
- [68] A. Schlumberger, J. Stec, D. Schmidtbleicher et al., "Single- vs. multiple-set strength training in women," *The Journal of Strength and Conditioning Research*, vol. 15, no. 3, pp. 284–289, 2001.
- [69] R. M. Otto and R. N. Carpinelli, "A critical analysis of the single versus multiple set debate," *Journal of Exercise Physiology Online*, vol. 9, no. 1, pp. 32–57, 2006.
- [70] M. R. Rhea, B. A. Alvar, and L. N. Burkett, "Single versus multiple sets for strength: a meta-analysis to address the controversy," *Research Quarterly for Exercise and Sport*, vol. 73, no. 4, pp. 485–488, 2002.
- [71] A. Rutchik, A. R. Weissman, P. L. Almenoff, A. M. Spungen, W. A. Bauman, and D. R. Grimm, "Resistive inspiratory muscle training in subjects with chronic cervical spinal cord injury," *Archives of Physical Medicine and Rehabilitation*, vol. 79, no. 3, pp. 293–297, 1998.
- [72] S. Ren, Y. Shi, M. L. Cai et al., "Influence of airway secretion on airflow dynamics of mechanical ventilated respiratory

- system,” *IEEE/ACM Transactions on Computational Biology and Bioinformatics*, vol. 15, no. 5, pp. 1660–1668, 2017.
- [73] W. H. Dobbelle, M. S. D’Angelo, B. F. Goetz et al., “200 cases with a new breathing pacemaker dispel myths about diaphragm pacing,” *ASAIO Journal*, vol. 40, no. 3, pp. 244–252, 1994.
- [74] M. N. Ilbawi, F. S. Idriss, C. E. Hunt et al., “Diaphragmatic pacing in infants. Techniques and results,” *The Annals of Thoracic Surgery*, vol. 21, no. 11, pp. 323–329, 1985.
- [75] Z. Li, W. Zuo, and S. Li, “Zeroing dynamics method for motion control of industrial upper-limb exoskeleton system with minimal potential energy modulation,” vol. 163, pp. 1–10, 2020.
- [76] Z. Li, C. Li, S. Li et al., “A fault-tolerant method for motion planning of industrial redundant manipulator,” *IEEE Transactions on Industrial Informatics*, vol. 16, 2019.
- [77] H. Su, W. Qi, C. Yang, J. Sandoval, G. Ferrigno, and E. D. Momi, “Deep neural network approach in robot tool dynamics identification for bilateral teleoperation,” *IEEE Robotics and Automation Letters*, vol. 5, no. 2, pp. 2943–2949, 2020.
- [78] W. Qi, H. Su, and A. Aliverti, “A smartphone-based adaptive recognition and real-time monitoring system for human activities,” *IEEE Transactions on Human-Machine Systems*, 2020.
- [79] A. Quotb, J. B. Floderer, T. Bollengier et al., “Live demonstration: real-time wavelet spike detection with in-vitro biological signals,” in *Proceedings of the 2012 IEEE Biomedical Circuits and Systems Conference (BioCAS)*, p. 79, Hsinchu, Taiwan, November 2012.
- [80] A. M. Zbrzeski, R. Siu, Y. Bornat et al., “A versatile fast-development platform applied to closed-loop diaphragmatic pacing,” in *Proceedings of the 2015 7th International IEEE/EMBS Conference on Neural Engineering (NER)*, pp. 791–794, Montpellier, France, April 2015.
- [81] R. Siu, J. J. Abbas, B. K. Hillen et al., “Restoring ventilatory control using an adaptive bioelectronic system,” *Journal of Neurotrauma*, vol. 36, no. 24, pp. 3363–3377, 2019.
- [82] B. K. Hillen, J. J. Abbas, A. Zbrzeski et al., “Adaptive control of ventilation using electrical stimulation in a biomechanical model,” *BMC Neuroscience*, vol. 16, no. 1, pp. 1–2, 2015.
- [83] M. D. Fairchild, S.-J. Kim, A. Iarkov, J. J. Abbas, and R. Jung, “Repetitive hindlimb movement using intermittent adaptive neuromuscular electrical stimulation in an incomplete spinal cord injury rodent model,” *Experimental Neurology*, vol. 223, no. 2, pp. 623–633, 2010.
- [84] H. Su, S. E. Ovrur, X. Zhou et al., “Depth vision guided hand gesture recognition using electromyographic signals,” *Advanced Robotics*, vol. 15, pp. 1–13, 2020.
- [85] L. Estrada, A. Torres, L. Sarlabous et al., “Improvement in neural respiratory drive estimation from diaphragm electromyographic signals using fixed sample entropy,” *IEEE Journal of Biomedical and Health Informatics*, vol. 20, no. 2, pp. 476–485, 2015.
- [86] L. Estrada, A. Torres, L. Sarlabous et al., “Onset and offset estimation of the neural inspiratory time in surface diaphragm electromyography: a pilot study in healthy subjects,” *IEEE Journal of Biomedical and Health Informatics*, vol. 22, no. 1, pp. 67–76, 2017.